ABSTRACT

Title of dissertation: An Experimental Study of Water Surface Features in Response to Rain

Ren Liu, Doctor of Philosophy, 2017

Dissertation directed by: Professor James H. Duncan
Department of Mechanical Engineering

Water surface features induced by the impact of raindrops on a deep water pool are studied experimentally in an artificial rain facility. Artificial rain is produced by a rain generator that consists of a rectangular tank with an array of 738 hypodermic needles attached to its bottom and that is mounted at various heights above a deep water pool. In this thesis, three rain intensities and four raindrop impact velocities are used while the diameters of raindrops remain approximately the same. For comparison with some of the results of the rain experiments, a set of single drop impacts on a quiescent water surface were also performed.

In the single drop impact experiments, cinematic shadowgraph methods were used to measure the drop diameter (D) and velocity (V) just before impact, to observe qualitatively the water surface response and to measure the height of the vertical water jet (stalk) that is typically part of the water surface response. It is found that the stalk height varies with impact Froude number ($Fr = V^2/(gD)$, where g is the acceleration of gravity) in three different ways depending on the Froude number range.

In the rain experiments, the drop diameters and velocities are measured with a cinematic shadowgraph technique while the temporal evolution of the surface profile along the center plane of the target water pool is measured with a cinematic Laser Induced Fluorescence (LIF) technique. The history of rain-induced stalk height and the profiles of the rain-induced surface waves are extracted at each instant in time. It is found that the stalk height varies considerably in the rain field and the average stalk heights are less than in cases with single drop impacting a quiescent surface at the same Froude number (Fr). The stalk height distribution correlates with the rain intensities rather than the impact velocity. Occasional bubble entrainment was observed at the lowest raindrop impact velocity ($Fr = 500$) while bubble entrainment only occurred for Froude numbers greater than 1800 in single drop experiments. Furthermore, surface waves outside of the rain field propagate faster than that inside the rain field.

Radar backscattering powers from raindrops, surface waves in front of the rain field and the water surface features inside a rain field are measured. The measurement results show that strong radar return signals are observed from the water surface inside the rain field while the radar return signals from both raindrops and the surface waves in front of the rain field are weak. The experimental results also show that the radar return intensity increases as the rain intensity increases from 85 to 300 mm/hr. In addition, it is found that the attenuation of the radar backscattering from the rain field is likely correlated with a high-water-content layer of secondary droplets generated in the rain field.

An Experimental Study of Water Surface Features in Response to Rain

by

Ren Liu

Dissertation submitted to the Faculty of the Graduate School of the
University of Maryland, College Park in partial fulfillment
of the requirements for the degree of
Doctor of Philosophy
2017

Advisory Committee:
Professor James H. Duncan, Chair/Advisor
Dr. Xinan Liu, Co-Advisor
Professor Richard V. Calabrese
Professor Kenneth Kiger
Professor Johan Larsson
Professor Amir Riaz

Dedication

To Mama and Baba.

Acknowledgments

First and foremost I would like to express my gratitude to my advisor and mentor, Professor James H. Duncan. His guidance and knowledge has helped me overcame many challenges I encountered throughout my graduate study. I am eternally grateful for everything he have taught me and his endless patience and kindness.

I would also like to thank my co-advisor, Dr. Xinan Liu. He provided valuable theoretical ideas and experimental expertise. He has always made himself available to help me. It has been a great experience to work with and learn form him. I wholeheartedly appreciate my committee members. Professor Richard V. Calabrese, Professor Kenneth Kiger, Professor Johan Larsson, and Professor Amir Riaz have spent their value time to serve on my committee and provided helpful comments. I would also want to thank Dr. Quanan Zheng and Dr. Mark Sletten for their help. I am grateful for the opportunity and support provided by the Academic Achievement Program and McNair Scholar program at University of Maryland, College Park.

My colleagues at the Hydrodynamic laboratory have also helped me in many ways. I want to thank Dr. Christine Ikeda, Dr. Dan Wang, Dr. Naeem Masnadi, Dr. Nathan Washuta, An Wang, Martin Erinin, Karan Parmar, Adama M. Sombie, Henry Brown, Steffen Harbarth,Yvonne Zhou for their supports and the knowledge I learned from each and everyone of them.

Special thanks to Emerald Ji, Roger Yu, My Le, Martin Hoe, Chang Liu, Kuang Xue, Haoyuan Liu, Rahul Mulinti, Roger Keiper, Antonio Acevedo-Ortiz and many others supported me along the way through friendship and to Yijia Zhu

for her companionship and understanding.

My deepest gratitude is to my family for their endless love and support. My mother and father, Guomei and Jinji, who have told me the importance of education and tried their best to provide a good study environment. I am forever in your debt.

Finally, I would like to acknowledge financial support from the National Science Foundation (NSF), Division of Ocean Sciences.

Table of Contents

List of Tables

List of Figures

List of Abbreviations

α	alpha
β	beta
RMS	Root Mean Square
LIF	Laser Induced Fluorescence
PIV	Particle Image Velocimetry
Fr	Froude Number
We	Weber Number
Bo	Bond Number

Chapter 1: Introduction

1.1 Motivation

Rainfall over the ocean plays an important role in the exchange of energy, mass and momentum between the ocean surface and atmosphere. It has been argued that approximately 79% of the world precipitation is over the ocean [2] and about three-fourths of the heat energy of the atmosphere is provided from the latent heat release in the formation of raindrops [28]. When the temperature of raindrops is different from the temperature of the ocean, the rainfall can change the ocean surface temperature and create a heat transfer [26] [57] . Oceanic rainfall generates turbulence within a thin layer of the water surface and the air entrainment and bubble formation due to the rainfall over the ocean can contribute up to 20 % to the total gas exchange [21]. The impact of raindrops on the ocean surface can enhance the production of sea salt aerosol [39]. Oceanic rainfall can also have a significant contribution to the ocean surface stress by transferring momentum from the raindrops to the water surface. Under some conditions, this surface stress is comparable to the wind stress [8]. In addition, the precipitation associated with the El Nino-Southern Oscillation (ENSO) has important influence on the ocean circulation [51].

The knowledge about rainfall over the ocean is limited due to the technical difficulties of measurements. Conventional rainfall measurement uses networks of rain gauges and weather radar systems where available. However, only a few gauges exist over the ocean and these are located on atolls and small islands. These gauges cannot represent the surrounding ocean due to local influences [27]. For global coverage of precipitation over the oceans, satellite remote sensing has the potential to overcome the spatial and temporal limitations of ground observations [41].

The satellite radar signatures of rainfall events over the ocean are mainly generated from two sources. One is the scattering and attenuation of microwaves by raindrops and ice particles in the atmosphere and the other is the scattering by the sea surface features that are associated with raindrop impacts. The effects of raindrops and ice particles on the scattering and attenuation of the microwaves in the atmosphere have been extensively studied by radar meteorologists [44]. The scattering is described by a volume backscattering coefficient that is a function of radar wavelength, refractive index of water and the reflectivity of raindrops while the attenuation is depicted by a volume attenuation coefficient that depends on the rain rate with a power law [64]. More recent experimental study by Lemaire et al. [31] showed that for a given raindrop size, the shape of the scatterometer spectrum was independent of the rain rates. For a given rain rate, the peak frequency and the spectral bandwidth were inversely proportional to raindrop sizes.

The effects of rainfall on radar scattering from the ocean surface were first investigated by Moore et al. [42]. Further investigations on this subject with different microwave frequencies were performed by Hansen [18], Sobieski et al. [61], Braun

et al. [6], and others. These studies show that the radar backscattering powers are dramatically affected by the rain-generated surface features, including crowns, craters, stalks and ring waves. Furthermore, Sobieski et al. [61] measured these surface features with a high-speed digital camera that was synchronized with radar data acquisition. They compared the radar backscattering powers from crowns, craters, stalks and ring waves and concluded that ring-waves are the dominant scattering contribution, though the scatterings from crowns, craters and stalks are not negligible. By developing a scattering model from the splash products of a single rain drop impact, Wetzel [66] showed that the stalk has significant effects on the major scattering features. Recently, a backscattering model developed by Liu et al. [36] [37] shows that the effects of stalks are dominate under low wind condition.

1.2 Previous Studies

An essential part of at-sea rain processes is the generation of surface features that are associated with raindrop impacting a deep water pool. These water surface features are extremely complicated. When raindrops impact on a water surface, they produce crowns, stalks, secondary droplets, ring waves and turbulence underneath the water surface. Due to the randomness of raindrop impacts in space and time, the surface features in response to each individual raindrop vary considerably. The simplest studies of this phenomenon, which is considering the impact of a single drop on a quiet water surface, started more than 100 years ago by Reynold [54], Worthington [67], etc. Thus, the literature review given below consists of both

outcomes of a single drop impacting a water surface and the surface features in response to rainfall with particular focus on stalks, surface waves and subsurface turbulence.

1.2.1 Single Drops Impacting a Liquid Pool

Many phenomena occur the impact of a single drop on an otherwise quiescent liquid pool. At first, the target pool surface is forced to deform downward which results in a crater at the location of impact and the crater is surrounded by a rim of displaced liquid to form a crown. Some small droplets detach from the top of the crown which are called secondary droplets. Then, the crown retracts and the crater starts to recover and results in a liquid jet, which is called a stalk, at the center of the crater. Depending on the impact conditions, some droplets can also be generated from the tip of the stalk, which is called tip drops. Surface waves, also called ring waves, are generated due to the oscillation of liquid surface caused by the impact. In addition to the above phenomena, a single drop impact also produces vortex rings that penetrate further down into the liquid pool.

Stalk has been studied extensively. Hobbs and Kezweeny [22] conducted an experimental study of a liquid drop falling from constant height impacting a liquid pool with different depths. They observed that the maximum height of the impact-induced stalk increases as the target pool depth decreased from 25 to 7 mm, but the maximum stalk height decreases sharply when the pool depth less than 7 mm.

Fedorchenko and Wang [15] studied the behavior of the maximum stalk height

using the Froude number. They derived an equation for the stalk height by assuming the total energy of the impacting drop is completely converted and the shape of the stalk was a circular cylinder. For the Froude number between 100 and 1100, they concluded that the non-dimensional stalk height ($H^* = H/D$)was proportional to the one fourth power of the Froude number ($Fr = \frac{V^2}{gD}$) :

$$H^* = 1.43Fr^{1/4} \tag{1.1}$$

where V is the drop speed at impact, D is the droplet diameter and g is the gravitational acceleration. It should be mentioned that very few articles have reported about the stalk behavior for impact condition with Froude number greater than 1000.

The other import dimensionless number associates with the formation and shape of the stalks is the Weber number given as follows

$$We = V(\rho D/T)^{\frac{1}{2}} \tag{1.2}$$

where ρ is density, and T is surface tension. Hsiao et al. [24] developed a theoretical model and claimed that whether a subsurface vortex or a stalk is produced depends on the Weber number. Based on a mercury-to-mercury impact experiment that they conducted and the data presented in Rodriguez and Mesler' s paper [55], Hsiao et al. concluded that a stalk would be formed during impact of a drop on the same fluid when the Weber number is above 8. Cresswell and Morton [12] proposed a theory for the formation of vortex based on the generation of vorticity on relaxation of surface stresses at coalescence but did not provide the value of the corresponding Weber number. Manzello and Yang [38] conducted an experimental study with

different target pool depths and two different liquids (water and HFE7100) for the target pool. The Weber number was used to determine whether the droplet would be produced by breaking up from the stalks (tip drops). They concluded that the Weber number for stalk breaking up was independent of the target pool depth for water to water impact.

While most of the studies explored drop impact on a stationary liquid pool, Alghoul [1] studied a drop impacting a liquid film which moved at speeds up to 0.2 m/s. The impact-induced stalk exhibited the same regimes as the impact in static liquids, but the transition boundaries were different. In addition, the stalks did not have an axisymmetric shape. Recently, Zhao [69] studied liquid droplets with diameters are less than 1 mm impacting a target pool of the same fluid. He used five different fluids and concluded that both low viscosity and low surface tension would create tall impact-induced stalks.

Ring waves have the longest duration among all the outcomes of single raindrop impacts and they have been studied both theoretically and experimentally. About 30 years ago, Crapper [11] presented some photographs of the ring waves created by the impact of raindrops of various diameters. Later, Mehaute [40] conducted a theoretical study of the ring waves generated by the impact of tiny objects such as raindrops onto an initially quiescent body of water by taking account of gravity, capillary and dissipative viscous effect. He pointed out that impact-induced ring waves belong to mixed capillary-gravity regime. He also concluded that ring waves were generated only by the oscillation of the water surface at the impact location and that they had a narrow range of wave numbers which relates to the minimum

group velocity of gravity-capillary waves. Furthermore, the amplitude of ring waves was proportional to the drop momentum when it hits the free surface and ring wave pattern was composed of a multiplicity of rings with increasing amplitude towarded the impact location and was terminated by a trailing wave with an exponential decay. Craeye et al. [10] measured the characteristic wavenumber of impact-induced ring waves. In their experiments, water droplets falled from three different heights onto two different target pools, one composed of fresh water and one of salt water. They found the characteristic wavenumber of impact-induced ring waves was around 0.2 mm^{-1}. They also noticed that the ring waves decayed to small amplitude of the order of 0.1 mm at 0.8 s after impact and further concluded that only a small amount, on the order of 1%, of the incident kinetic energy was converted to ring waves. Zhu et al. [70] studied experimentally the propagation of ring waves and their group velocity. They used 2 mm diameter drops impacting a lake from 1.47 m above. They found that the carrier waves and the group velocity of the ring waves packet were near the minimum point of the diversion curve of group velocity of gravity-capillary waves and claimed that this was the main reason the ring waves packet could propagate with low diffusion.

A number of experiments studied drop impact on pre-disturbed wavy surfaces. Schotland [58], Jayaratne and Mason [25] studied drops impinging onto wavy surfaces created by previous impacts and they founded that the effect of this wavy surface on the impact-induced surface features was small. However, the impact frequency that they used was low and the surface of the liquid layer may have mostly recovered from the previous impact. For high frequency impact, Siscoe and

Levin [59] studied the interaction of surface waves with impacting drops by allowing a continuous sequence of drops to fall on water surface in a circular battery jar. The battery jar wall would reflect the waves produced by the previous drops back into the center and interact with the following drops. When the drops fell at a constant frequency, there would appear a steady condition in which each drop impacts the surface wave at a fixed phase. This phase could be changed by varying the drop rate, the height of initial drop and the diameter of the battery jar. They found that depending on whether the drop would hit the crest or the trough of the wave, the drop would be absorbed and amplified the surface wave or form an unusually high stalk, respectively. They also found that the impact-induced vortex rings and eddies were confined roughly to a depth of 5 to 10 cm.

1.2.2 Raindrops Impacting a Deep Liquid Pool

The physical process of raindrops impinging onto a liquid pool is even more complex than the single drop case. Unlike single drop impact, the impact of a particular raindrop in a rain field is affected by the free surface motions and subsurface flow features due to the nearby random distribution of raindrop impacts prior to and during the impact of the drop of interest. Some important phenomena associated with raindrops impinging onto a liquid pool have been studied. These phenomena include rain-induced stalks, surface waves and sub-surface turbulence.

Unlike single drop impact, only a few articles report about stalk generation and the behavior of the maximum stalk height in a rain field. Wetzel [66] presented stalk

height distributions for two rain fields that had approximately the same rain rate. However, he did not provide details about how the stalk height data was obtained. Instead, Wetzel just claimed that he got these data through private communication with V. Cavaleri. From these data , Wetzel noticed that sometimes the maximum stalk height distribution looked like a Rayleigh distribution. However, a different rain with the same rain rate, the stalk height distribution could be quite different. Therefore, the correlation of stalk height distribution with rainfall conditions is still unclear.

Rain-induced surface waves, which are called ring waves in single drop impact, have also been studied in laboratory. Houk and Green [23] used a capacitance wave gauge to measure the surface waves due to artificial rain. In their raindrop distribution, 73% of the drop had diameters near 2.2 mm, 23% of the drops had diameters near 3.6 mm and 4% had diameters near 5.5 mm. All of the drops had speeds within 1% of their terminal velocity and impacted a thoroughly mixed receiving water. Houk and Green [23] found that the root mean square (RMS) surface height fluctuation was proportional to the rain kinetic energy flux and raindrop size but inversely proportional to the liquid viscosity. Bliven, Sobieski and Craeye [5] conducted an experimental study with 2.8 mm diameter raindrops impacting a target pool at terminal velocity. The artificial rain rate was varied between 5 and 200 mm per hour. They concluded that the energy of rain-induced surface waves is predominately within the range of 2 to 15 cm wavelength. The maximum wave energy was occurred at a wavelength of about 5.3 cm.

Many studies focused on rain-induced turbulence because this feature en-

hanced air-water gas exchange and damp the surface waves with sufficient rain intensity. Ho el al. [21], Zappa et al. [68], Harrison et al. [20], etc. claimed rain-induced turbulence enhanced air-water gas exchange. Green and Houk [17] studied the rain-induced mixing layer depth. They used rain fall distributions consisting of both a single raindrop diameter and a crude drop-size distribution which consisted of 4% of 5.5 mm drops, 23% of 3.6 mm drops and 73% of 2.2 mm drops. The receiving water pools were one composed of fresh water and one of salt water. Their result showed that large drops played an important role in the mixing process. Furthermore, upward entrainment coefficients varied inversely to a suitably defined bulk Richardson number and the fresh and salt water results were nearly the same. Ho et al. [21] studied the mixing of three different gas helium, nitrous oxide, and sulfur hexafluoride due to 22 different rain rates which were between 13.6 to 115.2 mm per hour. The raindrop sizes were 2.3, 2.8 and 4.2 mm in diameter and were able to reached their terminal velocities before impact. Their experiment showed that the rain-induced turbulence was the dominate factor in the air-water exchange process. Generated bubbles contributed about 0 to 20 % to the total gas exchange. The contribution of rain-generated bubbles to mixing increased with higher rain rate and larger diameter raindrops. Lange et al. [29] measured rain-induced surface mixing using dye, digital partial image velocimetry and ultrasonic sounding techniques. The average diameter of the raindrops was 2.9 mm and the impact velocity was about 80-85% of the terminal velocity. They measured typical eddies of 10-15mm in diameter. The turbulence layer thickness was found to be 15 cm for a moderate rain rate and showed homogeneous turbulence. Zappa et al. [68] measured the tur-

bulent kinetic energy dissipation rate of a rain event over a wavy saltwater surface with a pulse to pulse coherent doppler. However, the measured turbulent velocity fluctuation was significantly higher than measured by Lange. Beya et al. [3] also measured rain generated turbulence in freshwater with Acoustic Doppler Velocimeter and reported the smallest turbulent velocity fluctuation among the three. Their result was one order of magnitude less than those measured by Zappa. Beya et al. also claimed that the rain rate had no significant influence on turbulence intensity while Harrison et al. [20] reported that turbulent kinetic energy dissipation near the free surface was increase with increasing rain rate at low wind speed.

1.2.3 Radar Backscattering of Rain

For remote sensing application, the microwave signatures of the ocean surface features, which are associated with raindrop impacts, are studied. Rain can affect the microwave signatures of a ocean surface by producing additional roughness through craters and crowns, stalks, and surface waves. However, how those surface features affect the electromagnetic scattering are not well understood due to the complexity and chaos of a rain field.

From previous studies, stalks and surface waves significantly affect the radar backscattering power. Wetzel [66] developed a model and claimed that rain-induced stalk are dominant for radar backscattering with 75 degree from nadir. Bliven et al. [4] studied the rain-induced surface waves using 13.5 GHz scatterometer with 30 degree incidence angle in a wind-wave tank. Their simulated rain intensities were

between 10 and 30 mm per hour. They found that rain-induced surface waves are the dominate feature contributing to backscattered power. Bliven et al. [5] also claimed that wave energy and backscattered power increased with the rain intensity but the growth rates reduced at higher rain intensity. Lemaire et al. [31] performed a similar experiment, but they used various drop sizes and tested monodisperse and polydisperse rain events. They observed that for a given drop size, the shape of the scatterometer spectrum was independent of the rain rates. For a given rain rate, the peak frequency and the spectral bandwidth were inversely proportional to drop size but the wave energy was proportional to drop size. They also found that the ring wave spectra in polydisperse rain events could be derived from the mono disperse rain-induced wave spectra. Braun et al. [6], Peirson et al. [47], etc. reported that heavy rain would damp the surface waves and affect the radar backscattering of an ocean surface.

Previous studies also showed that velocity of raindrop is important. Sobieski el al. [61] studied the backscattering of rain induced surface features for raindrops impact at terminal and non-terminal (50 % - 60 %) velocities. They found the significant differences of geometrical and backscattering characteristics of surface features between these two cases.

1.3 Thesis Outline

Given the above-noted importance of the surface features in the satellite radar backscattering, the study of the water surface features in response to rainfall is

crucial to improve the measurement of oceanic rainfall by using satellite. The main objective of this thesis is to experimentally investigate the water surface features inside an artificial rain field.

Details of the experimental apparatus are given in Chapter 2. Rain intensities and raindrop impact velocities are the two important factors. Three measurement techniques were used for measuring water surface profiles, sub-surface velocity field, and the radar backscattering signals. Chapter 3 contains results and discussion of these three measurements. Chapter 4 provides a conclusion and suggestions for the future research.

Chapter 2: Experimental Details

The artificial rain experiment was performed in a rain facility built in the Hydrodynamics Laboratory at the University of Maryland, College Park. As shown in Figure 2.1, The facility includes an overflow water tank that acts as the target pool and a rain generator. The rain generator can be located at heights up to 4.8 m above the target pool to create a range of droplet impact velocities on the target. The rain impact process is measured with a variety of time resolved techniques including shadowgraph, LIF images, stereoscopic PIV, and radar remote sensing as described below.

2.1 Rain Facility

2.1.1 Target pool

The target pool is a 1.2-m-by-1.2-m square tank in plane view with a depth of 0.31 m and is constructed of transparent acrylic, see Figure 2.2. The upper edges of two opposing sidewalls of the tank are 1.27 cm lower than the other two and overflow channels are attached to these sidewalls. The target pool is supported by a short frame which is adjusted so that the upper edges of the two lower side walls

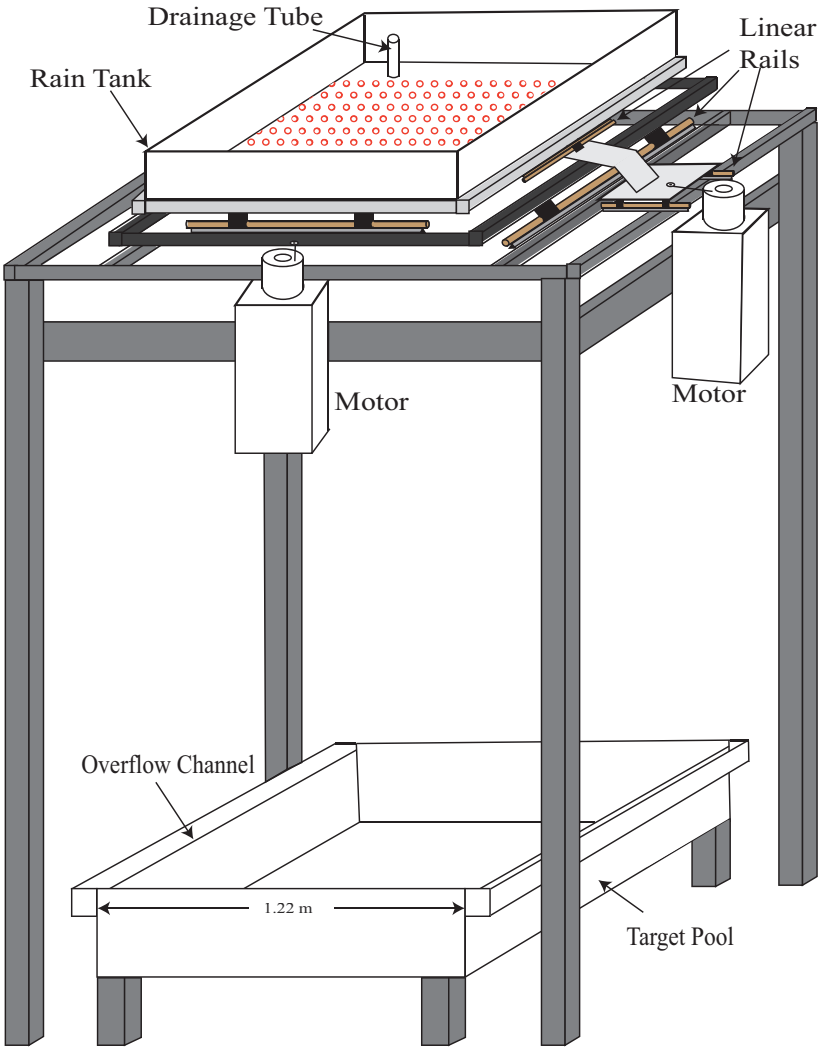

Figure 2.1: Experimental facility.

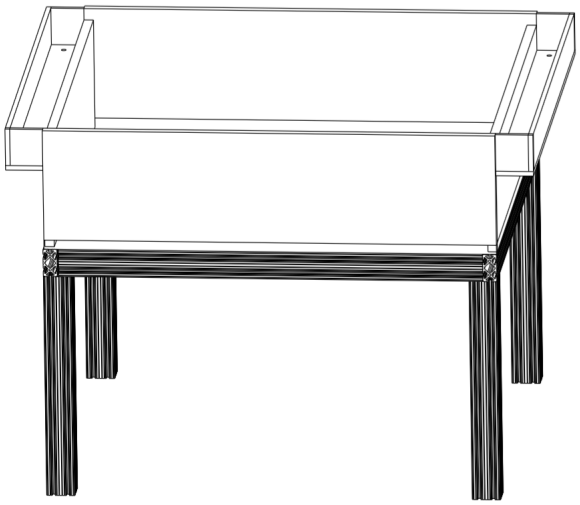

Figure 2.2: Target pool.

form a horizontal plane. The bottom of the water tank is about 0.5 m above the ground, allowing space for optics to project laser light sheet from below. The target pool is operated with a constant water level by maintaining an overflow condition at the two lower sidewalls with inflow due entirely to the incoming rain drops.

2.1.2 Rain Generator

The rain generator consists of a rectangular open surface tank (horizontal dimensions 0.9 m by 0.6 m) with a rectangular array of 738 equal spaced hypodermic needles protruding through its bottom surface, see Figure 2.3. During the experiment, the tank is filled with water at a constant rate and a constant water level is achieved with the aid of vertically oriented overflow drainage tube mounted with adjustable height. The tank is mounted on a linear traverser system with two horizontal degrees of freedom. Each axis of the traverser system consists of two parallel

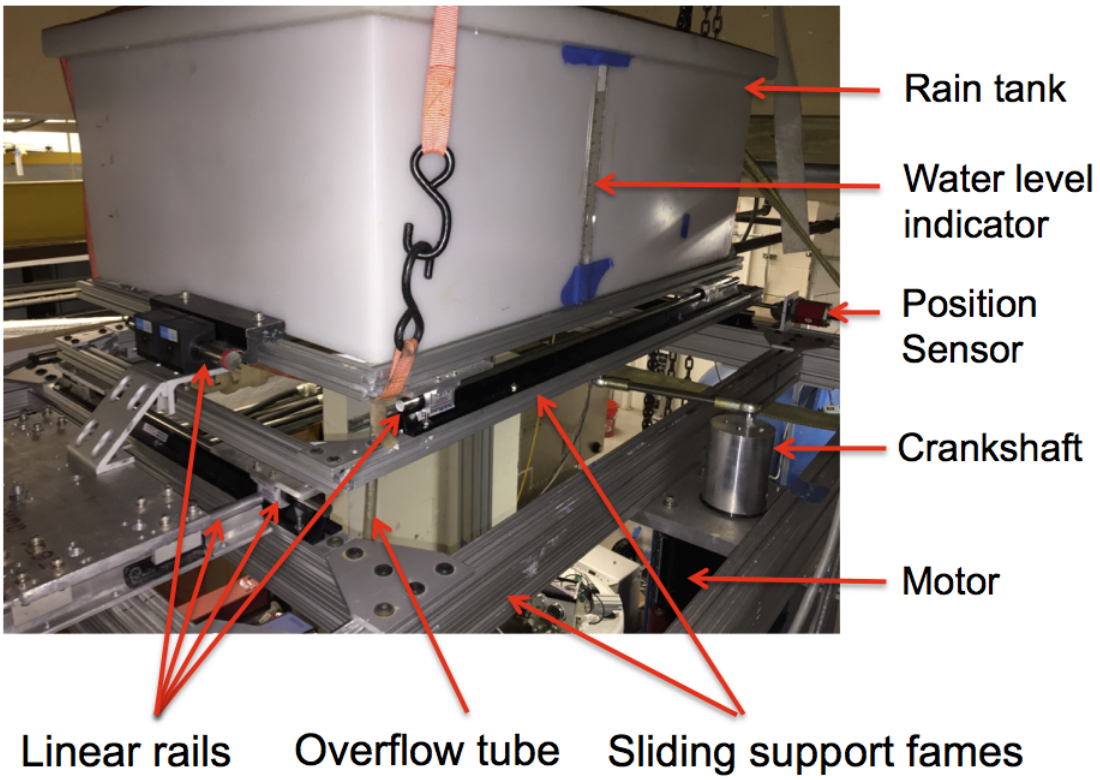

Figure 2.3: Rain generator.

rails, two bearings, a servomotor, a crank-piston drive mechanism and a linear position sensor. The motion of the rain generator is controlled by a computer using the position feedback sensor on each motion axis. A floating closed cell foam pad is place inside the rain tank to reduce any surface fluctuations that may be induced by the traverser system. In the following, the term 'rain generator' is used to refer to the entire above-described system.

2.1.3 Impact Velocity Variation

To achieve different impact velocities, the traverser system was mounted on top of a frame with adjustable height. Due to the limited height of the laboratory

ceiling, the maximum distance between the bottom end of the needles and the water surface in the target pool was 2.2 m. With this maximum height, the raindrops reached impact velocities of 72% of their terminal velocity in natural conditions. In order to achieve higher terminal velocities with the same diameter raindrops, a section the steel grating in the ceiling above the rain generator was removed to create a 1.83-m-by-1.83-m opening. Then, two 3-m-long 80/20 square beams with a 7.62-cm-by-7.62-cm cross section were placed across the opening and clamp fixed to the floor above the laboratory. Three 3.6-m-long pieces of lumber with nominal 4-inch-by-4-inch cross sections and two with 2-inch-by-4-inch cross sections were then placed parallel to the 80/20 beams for additional support. A plywood platform was mounted on top of the lumber supporting beams to cover the opening area for safety when not in use. At the four corners of the platform, small rectangular holes were cut in the platform to mount the tall rain generator support frame on the 80/20 beams. Plywood side walls were then attached to the structure for stability, see Figure 2.4. With this arrangement, the rain generator could be positioned so that the distance between the ends of the needles and the water surface in the target tank was 4.8 m and the impact speed of the raindrops reached 90% of the terminal velocity for the drop diameters used in this study.

2.1.4 Artificial Rain Intensity Variation

The artificial rain intensity was varied by varying the needle length, the water level inside the rain generation tank, and the needle arrangement. In order to

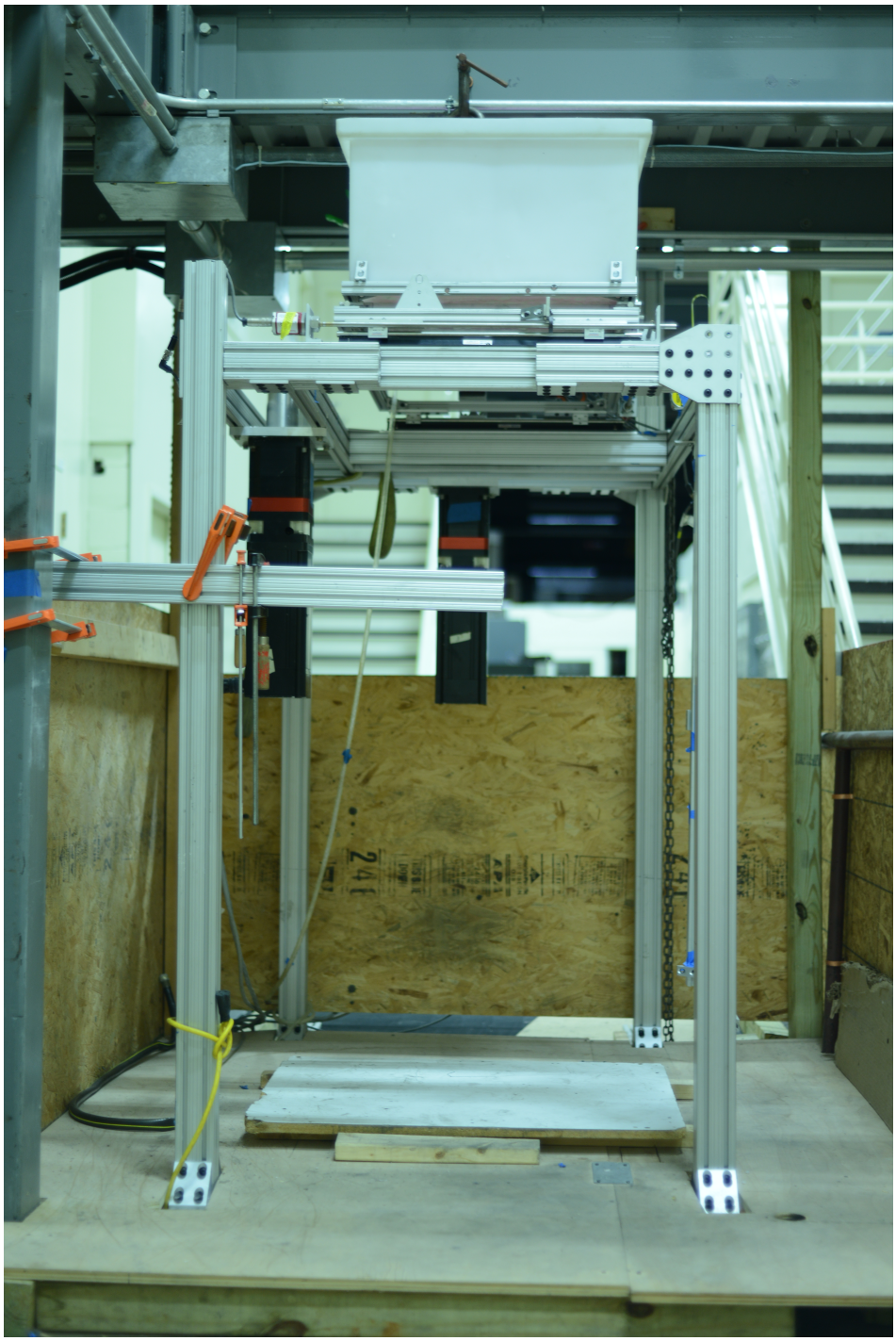

Figure 2.4: Experimental facility.

maintain constant droplet size (2.6 mm - 2.8 mm in diameter), all needles used were 22-gauge with an inner diameter of 0.41 mm. However, two different needle lengths, 50.8 mm and 6.4 mm, were used. The water in the rain generator reservoir was kept at a depth of about 25 cm for the long needles and 10 cm for the short needles by adjusting the height of the drainage tube. This resulted in a raindrop diameter of 2.6 mm and two different drip rates, about 3 Hz and 4 Hz.

For the single-drop impact experiments, only one of the 22-gauge needles with a 6.4-mm length was used. For the rain experiments, four needle arrangements were used. These arrangements consisted of blocking the flow to some of the needles as shown in the schematic drawings in Figure 2.5. For the full field concentrated case, see Figure 2.5(a), 35 rows of needles were used and the needles covered almost all of the bottom surface of the rain tank. In this case, there are a total of 717 needles and the distance between the needles is uniform, 2.54 cm. For the full field scattered case, see Figure 2.5(b), the 17 odd rows of the full field concentered case were blocked and the 18 even rows were used. There were 360 working needles and the distance between the needles is 2.54 cm along the y-axis (vertical in figure 2.5) and about 4.4 cm along the x-axis. In the half field concentrated and half field scattered cases, Figures 2.5(c) and (d), respectively, half of the rain field was blocked in order to have enough space to study the surface waves outside a rain field. As a result, 18 rows were used for a half field concentered case and only 9 of the even rows were used for the half field scattered case.

The rain generator was in motion for the rain experiments but remained stationary for the single drop impact experiments. For the concentrated cases, the rain

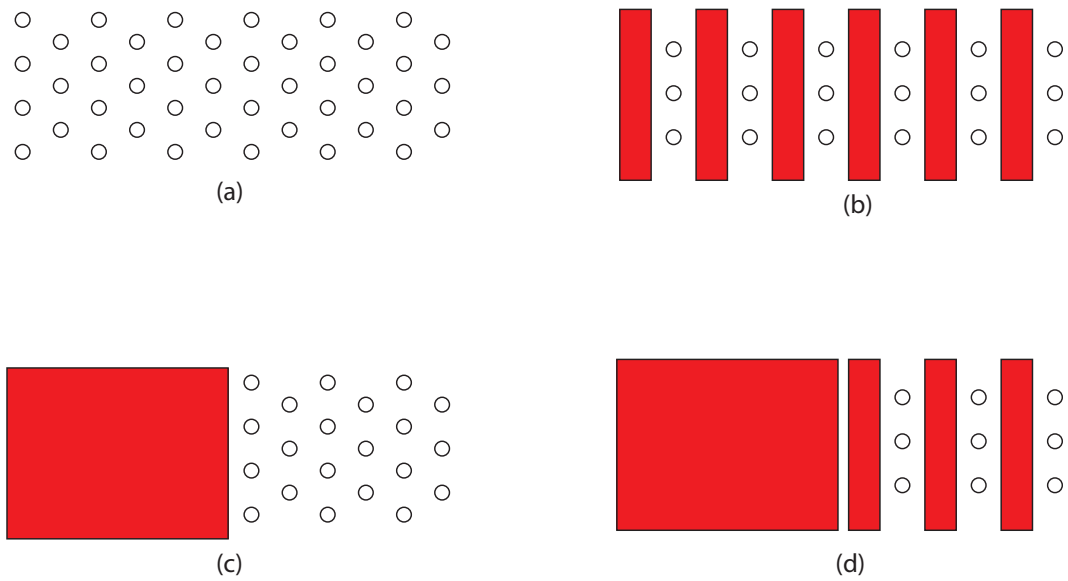

Figure 2.5: The four needle arrangements used in the experiments. The open circles indicate open needles used to generate raindrops, but in these schematic drawings only a small faction of the needles used are shown. The needles in the red regions were blocked so that no droplets were produced. (a) Full field concentrated, (b) Full field scattered, (c) Half field concentrated, and (d) Half field scattered. In this figure, the x axis is horizontal and the y axis is up.

generator motion was circular with a diameter of 2.5 cm and a frequency of 0.5 Hz. For the scattered cases, the rain generator moved in an oval path with the diameters along the y and x axes equal to 4.33 cm and 2.5 cm, respectively. With this combination of the needle separation and the motion of the rain generator, the average distance between two adjacent raindrop impacts on the water surface is about the same for both the concentered and scattered cases.

2.1.5 Artificial Rain Intensity Measurement

The rain intensity was measured using a ruler and a stop watch. The ruler is attached to the side wall of the target pool as shown in Figure 2.6. After a given rain experiment, the rain rate was maintained and water was drained from the target pool until the water level was 50 mm below the lower tank walls. The water level was then recorded and the stop watch was started to measure the elapsed time. After the 15 minutes, the water level was record again. Then, the following formula was used to relate the rain intensity R (mm/hr) to the water level difference L (mm), the surface area of the target pool A_T (m^2), and the active surface area are of the rain generator A_G (m^2):

$$R = \frac{4LA_T}{A_G}. \tag{2.1}$$

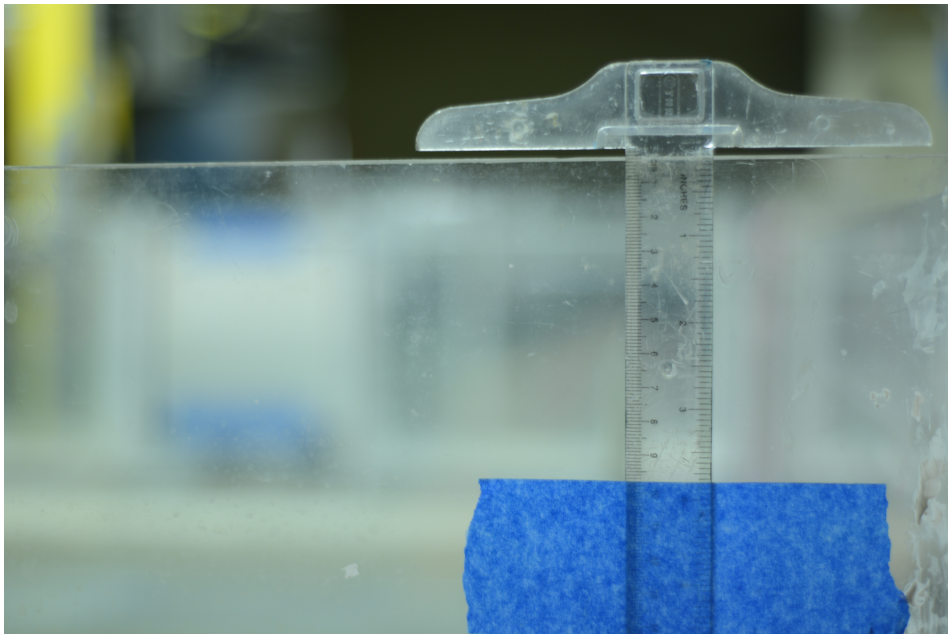

Figure 2.6: A ruler is attached to the target pool edge for rain intensity estimation.

2.1.6 Water Preparation and Surface Tension Measurement

The literature review showed that surface tension (Weber number) is an important factor in liquid to liquid drop impact, so clean fresh water was prepared for the experiments by using a special procedure. In the morning, the day before a given experiment, a 0.91 m in diameter round storage tank (Figure 2.7) was be filled with filtered tap water up to 1.68 m in height. Then, chlorine was added to the round tank such that the water free chlorine level of 3 ppm. The water was then circulated through a diatomaceous earth filter for about 6 hours before filling the 0.45 m^3 target pool. After the target pool was filled, the round storage tank was filled with filtered tap water again. Then, pool chlorine was added to the round tank such that the water had a free chlorine level of 5 ppm. The water was then circulated overnight for about 12 hours. On the following experiment day, a sufficient

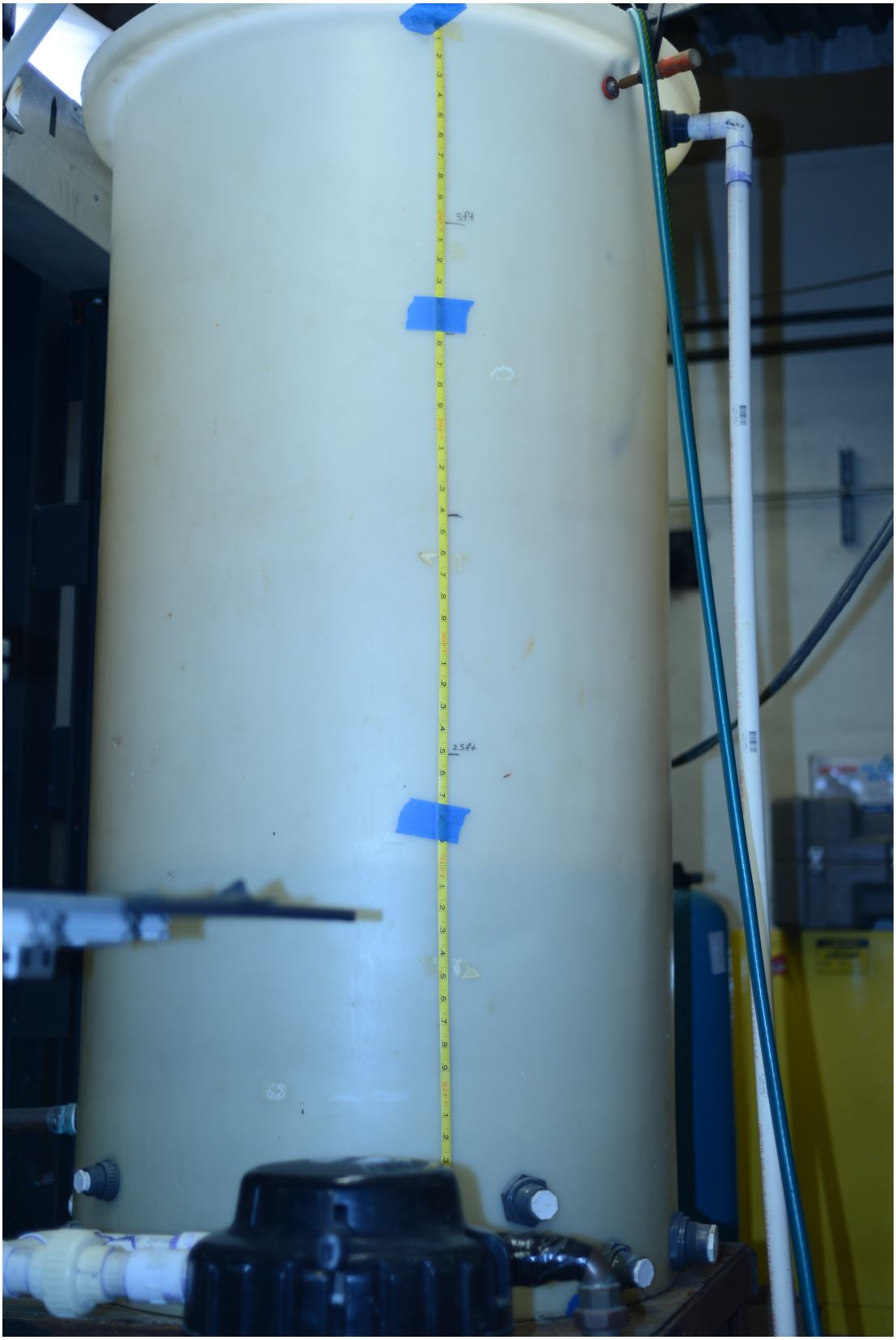

Figure 2.7: Round water storage tank used to prepare clean water.

amount of hydrogen peroxide was added to the round tank in order to dechlorinated the water to about 2 ppm. In this way, about 1100 liter of water was prepared for experiment. For the maximum rain intensity of 340 mm/hr over a 0.56 square meter area. The round tank would supply water for about 7 hours.

During the experiment on each day, three samples of the target pool water were extracted after the calibration and before the first experimental run, in the middle of the experiment (if there were ten runs, the sample was taken after the 5th run), and after the last run. The surface tension isotherm of each sample was measured using a KSV NIMA Langmuir trough as shown in Figure 2.8. Before the surface tension measurement, a Platinum Whilhelmy plate was heated with a Bernzomatic propane torch to clean its surface. The trough and its two movable Teflon barriers were rinsed by the sample water from the target pool. Then, the remaining sample water was poured into the trough. Finally, the two barriers was placed on the trough such that they barely touch the water surface and the Whilhelmy plate was lowered so that it dipped into the sample water. During surface tension measurement, the Platinum Whilhelmy plate monitored the surface tension as the water surface in the trough was compressed by the two Teflon barriers as they moved toward each other at a constant rate of 180 mm/min. As a result, the number of surfactant molecules per unit water surface area in between two barriers was increased with increasing time.

An example of the surface tension isotherm results is shown in Figure 2.9. Before the compression, the fresh water used for experiment had a surface tension of 73.0 ± 0.5 mN/m, which is close to the value for clean water. Then, the water surface

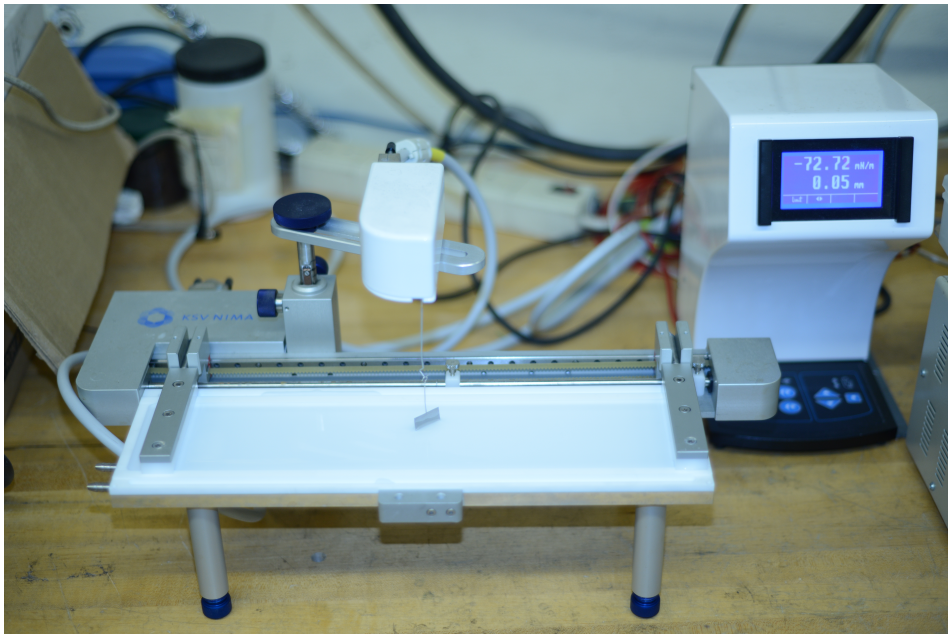

Figure 2.8: KSV NIMA Langmuir trough used for surface tension measurement.

area was compressed about 80%. As image shown, the surface tension remained at about 72 mN/m through a 70% compression and then experienced a sudden drop beyond about 75 % compression. This data is typical of the surface tension isotherm data in all experiments discussed herein.

2.2 Shadow Graph Measurement

In this study, measurements were performed for both single drop impact experiments and raindrop impact experiments. As mentioned in the Chapter 1, only a few researchers, for example Fedorchenko and Wang [15] ,studied the maximum stalk height of a single drop liquid-to-liquid impact and they only recprded data for impact Froude numbers ($V^2/(gD)$) less than 1,200. However, Laws' report [30] and theoretical predictions using a drag coefficient approximation given by Cheng [9]

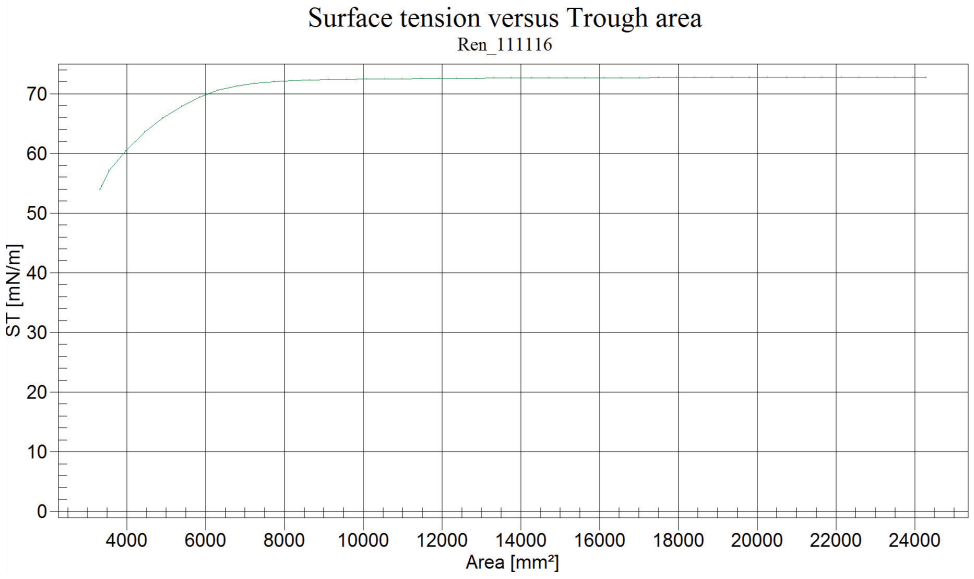

Figure 2.9: A sample surface tension test result using the Langmuir trough. The vertical axis is the surface tension measured by the Wilhelmy plate and the horizontal axis is the water surface area between the two teflon barriers.

showed that raindrops with 2.6 to 2.8 mm diameters have terminal velocities greater than 8 m/s, which has a corresponding Froude number greater than 2,200. Thus, a single drop impact experiment was needed to study the maximum stalk height variation for Froude numbers greater than 1,200 in the single drop impact experiments. For the rain experiment, knowing the raindrop impact conditions is essential for comparing the outcomes of a raindrop impacting on a wavy water surface in a rain field to a single drop impacting on an otherwise quiescent surface. In order to obtain the required data, the following cinematic shadowgraph measurement setups for the single drop and rain experiments.

2.2.1 Single Drop Impact Experiments

For the single drop impact experiment, only one needle was activated and a rectangular glass tank (0.9 m x 0.4 m x 0.2 m) was used as the target pool. This tank was chosen because its small volume (0.07 m^3) reduced water usage. As shown in Figure 2.10, a small bucket was placed above the target pool and was used as a shutter. During the experiment, the shutter bucket was quickly moved out of the way between droplet impacts, then allowing the next drop to hit a quiescent water surface in the target pool. After the measurements for the first drop impact, the shutter bucket position was restored to catch the droplets again. Water from the round storage tank was then fed to the target pool, thus overflowing the tank for about 5 minutes in order to clean the water surface. The water supply was then turned off and a period of 10 minutes was allowed for the target pool to again become nearly quiescent before the next drop impact.

The single drop impacts were recorded by two high-speed digital movie cameras (Phantom V640, Vision Research), which were set to a frame rate of 2,000 frames per second (fps) and synchronized through a BNC pulse delay generator. The first camera (1) was placed in front of the target tank and oriented to view the water surface from the front with a look-down angle of about 0.6 degrees from the horizontal. By using a metal combination square, camera 1 was carefully oriented such that, other than the small look-down angle, its lens was perpendicular to one of the vertical glass walls of the target tank. The light source was a 650 watt flood lamp which was placed on the opposite side (behind the target tank) and pointed

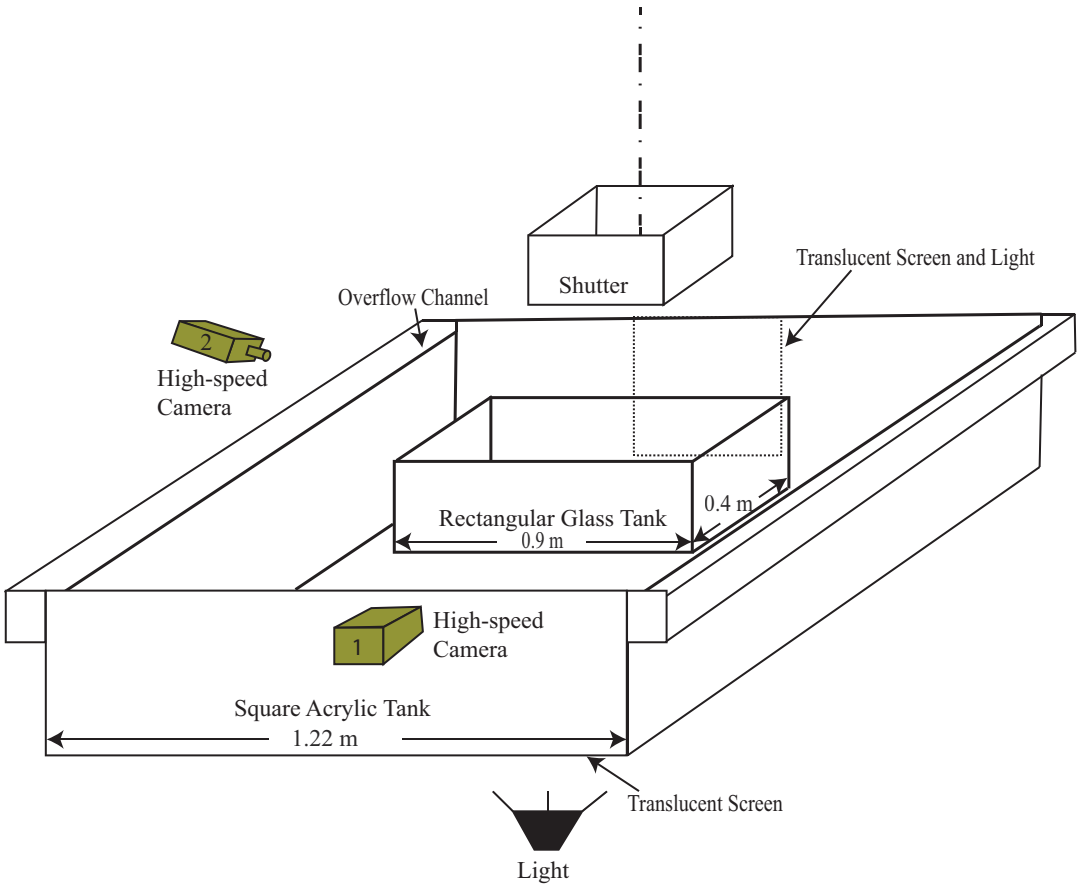

Figure 2.10: Experimental setup for the single drop impact measurements.

into the line of sight of the camera 1 lens through a translucent screen. Camera 1 was equipped with a 200 mm lens. Camera 2 was used for verification of the location of the drop impact. The line of sight of camera 2 was horizontally perpendicular to the line of sight of camera 1 but with a look-down angle of 45.4 degrees. The light source for camera 2 was a 650 watt flood lamp which was placed under the square tank and oriented to shine upward through a translucent screen. From the camera 2, the drop impact location relative to the focus plane of the first camera could be measured; only single drop impact events which were located less than 5 mm away from the focus plane were collected for the data set. From the high-speed movies, the droplet diameter, droplet impact speed, and stalk height were obtained.

2.2.2 Experimental setup for raindrop velocity and diameter measurements.

To measure the raindrop diameters and impact velocities, two sections of 7.62-cm diameter PVC tube are placed in line horizontally across the free surface of the target pool with a 25.4 mm gap in between the adjacent tube ends as shown in Figure 2.11. The outer ends of the tubes were located outside of the rain field. Each PVC tube blocks all the raindrops along its length allowing only the drops from 2-3 needles above the gap to be captured when looking through the length of the tube from one end. A high-speed digital movie camera (Phantom V640) was placed at one end of the tube with its line of sight directed along the tube axis and a back-lighted translucent screen was placed at the end opposite the camera. The majority

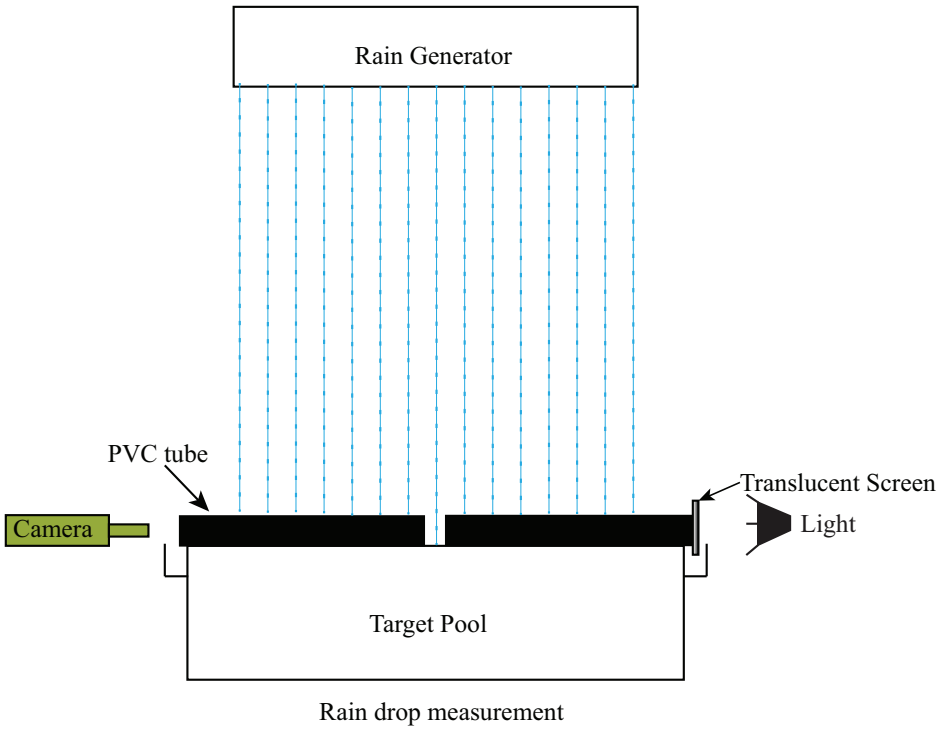

Figure 2.11: Experimental setup of the raindrop impact condition measurement.

of the measurements were conducted when the rain generator remain stationary. A few measurements were conducted when the rain generator was moving, the drop impact velocities and diameters were the same as in the case with the stationary rain generator.

2.2.3 Calibration

For the single drop impact experiments, the error was estimated using an optical formula considering an ideal Gaussian optical system [34]. For the possible error due to impact location variation, the following formula was used to relate the distance between the focal plane and the object s_o, the focal length f, and the magnification error M_e :

$$M_e = \left| \frac{-f}{(s_o - f)^2} \right|. \tag{2.2}$$

Since the collected impact events were less than 5 mm away (measured by camera 2 using the calibration image if Figure 2.12 (b)) from the focal plane and the focal length was at least 0.6 m, the resulting error due to distance between the impact location and the focal plane should be less than 0.17%. From calibration images, it was found that the camera 1 had greater than 22 pix/mm resolution. For measuring the raindrop, only 1 camera was used and calibrated. The procedure and calibration image was similar to Camera 1 of the single drop impact experiment. Raindrop measurement had 5 times more error than single drop experiment because the drop could be anywhere within the 25.4 mm gap in between the adjacent tube ends, but the error was still less than 1%.

2.2.4 Image Processing

To extract the droplet diameter and droplet position from the digital images, a gradient-based method was applied. Images illustrating various steps in this ex-

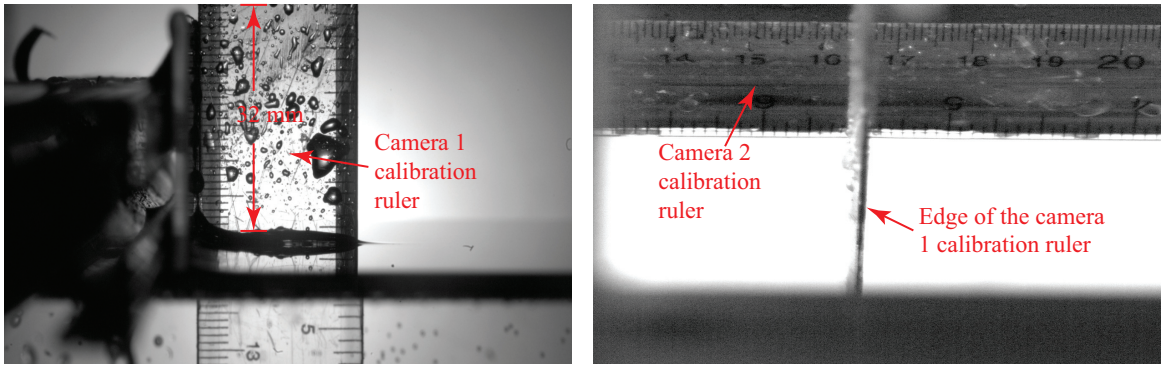

(a) (b)

Figure 2.12: Calibration ruler images of shadow graph measurement. Image (a) is captured by camera 1 and the vertical ruler image is used to correct the image distortion due to look-down angle by measuring the number of pixels in 32 mm vertical distance. Image (b) is captured by camera 2 and the horizontal ruler image is used to determine the impact distance respects to the focus plane (the edge of the camera 1 calibration ruler).

traction method are shown in Figure 2.13. In the first step, a constant threshold is determined from images in a given experimental run. Then, all the pixels with grey levels below the threshold were converted to white and all the pixels with gray level equal to or above the threshold are converted to black. This converts the original gray level image to a a black and white image, see Figure 2.13(b). Next, this black and white image was processed with a smoothing filter and a gradient operator to obtain gradient intensity image. The pixels with the highest values of image-intensity gradient were taken as the location of the edge of the droplet. Due to droplet oscillations while falling, the droplet may not appear as a perfect circle in the images; however, since these oscillations in shape were small, the drop diameter and the position of its center were determined by fitting a circle, by using a least squares method, to the locations of the pixels with maximum gradient intensity. In figure 2.13(c), this fitted circle plotted on top of the raw image. The final droplet diameter was determined by averaging the diameters determined by this method to five consecutive images taken (at 2,000 fps) just before impact. To extract the impact velocity, the horizontal and vertical positions of the drop center in two frames separated by 2 ms was used. It was found that the horizontal velocity was less than 0.01% of the vertical velocity. Thus, the droplet speed was taken as the vertical component.

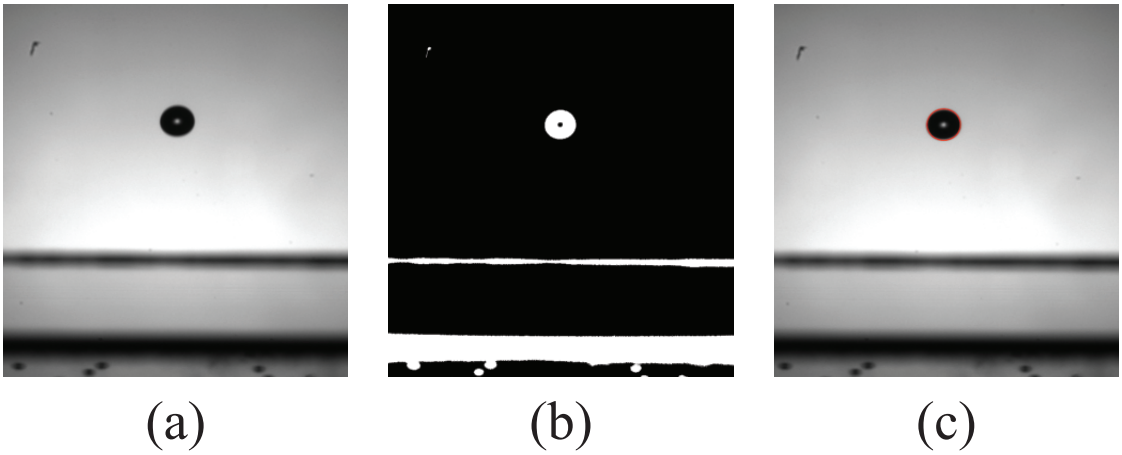

Figure 2.13: Shadow graph image processing for determining droplet diameters and speeds. (a) Original image of a drop before impact. (b) Image (a) after thresholding and conversion to black and white. (c) Image (a) with computed outline of the droplet shown in red.

2.3 Surface Profile Measurement

A cinematic planar laser induced fluorescence (LIF) method was used to measure the water surface profile during rain drop impact in regions both within and adjacent to the rain field in the target pool. Various aspects of this method are described in the following subsections.

2.3.1 Fluorescent Dye Preparation

Fluorescein Sodium salt (F6377) powder was mixed with the water in the rain facility by using the following procedure. First, a laboratory analytical balance was used to obtain a 0.4 g sample of the dye powder. This sample was then mixed into 800 ml of distilled water to produce the dye mixture. Disposable latex gloves and

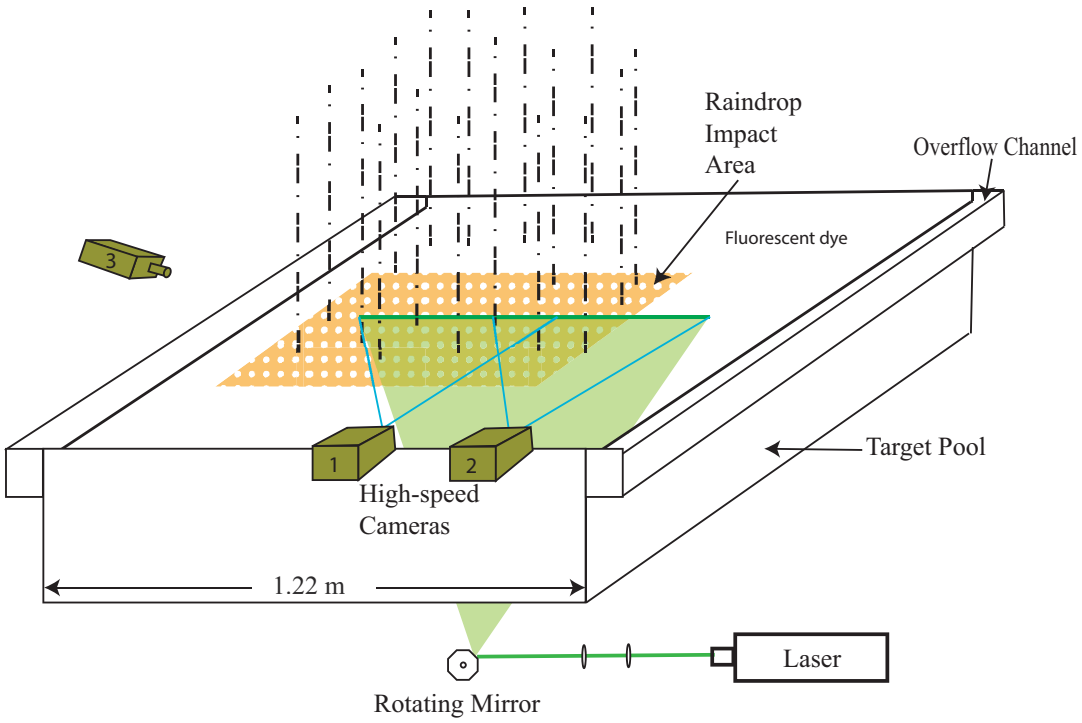

Figure 2.14: LIF measurement setup.

a 3M industrial respirator were used during the above preparation process. Before the experiment, 1 ml of the dye mixture was added into the 0.45 m^3 of water in the target pool and 2.4 ml of the dye mixture was added into the round tank so that the incoming raindrops would not decrease the dye concentration. This resulted in a dye concentration about 1.1 ppm throughout the system.

2.3.2 Experimental Setup

A vertically oriented laser light sheet and 3 synchronized high-speed digital movie cameras were used in the LIF surface profile measurement technique, see Figure 2.14. The light sheet was created from the beam of 5-Watt CW Argon-Ion laser that was operated in all lines mode (power output dominated by spectral lines

at wavelengths of 488 nm and 512 nm). A train of fixed mirrors, lenses and a rotating mirror were used to direct the beam to its focal point at the water surface where the beam waist about 1 mm in diameter. In this optical path, the fixed mirrors were used to direct the beam horizontally under the target pool where the beam intersected the rotating mirror. This mirror consisted of 3/8-inch-thick 12-sided aluminum polygon with polished edges. The rotation axis was horizontal and as each mirror facet passed through the beam it was deflected in a vertical plane and scanned over an angle of 60 degrees. This light sheet was positioned at the mid-plane of the tank and oriented to extend perpendicular to the two overflow channels. The mirror rotation rate was 12,000 rpm thus producing a scan rate of 2.5 per ms. The cameras were set with a frame rate of 250 Hz and an exposure time of 4 ms so within each frame the laser beam was scanned 10 times, thus creating essentially a uniform light sheet for each image. The three high-speed digital movie cameras (Phantom V640 an V641, Vision Research) were synchronized frame by frame by using a pulse delay generator (Berkeley Nucleonics). The first camera was oriented to view the intersection of the light sheet and the water surface in the rain field from the side with a look-down angle of about 10 degrees from the horizontal. To measure the surface waves outside the rain field, the second camera was oriented parallel to the first camera and positioned such that 50 % of its field of view overlapped that of camera 1 while the other 50% of its field of view was adjacent to the rain field. The line of sight of the third camera was oriented along the light sheet, i.e., nearly perpendicular to the view of the first and second camera. With 50 mm Nikon lenses, the images captured by the first and second camera, which consisted of an array

of 2,560 x 1,440 pixels, had a resolution of 7.3 pixels/mm and a horizontal field of view of 35.1 cm in the plane of the light sheet. The third camera was used only to verify that the drop impacts used in the measurement set occurred within the light sheet. A long-wavelength-pass (cut off wavelength 550 nm) optical filter was placed in a 3-D printed housing and then attached in front of each camera lens by using Cokin ring adaptors as shown in Figure 2.15. These filters blocked the primary light wavelengths of the laser thus minimizing specular reflections of the laser beam from reaching the image sensor in the camera while transmitting a portion of the fluoresced light. With this system, the primary light source for the images is the glowing dye within the light sheet near the water surface.

Sample LIF images from the first and second cameras are shown in Figure 2.18(a). The interface between the dark upper and bright lower region of each image is the intersection where the light sheet hits the water surface. The region below the interface was bright because the laser beam was projected from the bottom of the target pool and illuminated the fluorescent dye along its path. Therefore, the fluorescing light worked as a background light and made the water surface in front of the light sheet visible. Due to the surface shape fluctuations in the rain field, some fluorescing light was refracted from high slope portions of the water surface behind the light sheet as well.

Figure 2.15: A long-wavelength-pass 550 nm optical filter mounting on a 50 mm lens.

2.3.3 Calibration

For the measurement cameras (camera 1 and 2), images of rulers placed above the water surface and in the plane of the light sheet were taken to determine the resolution and to correct for image distortion due to the 10-degree look down angle of the cameras. One of these calibration images is shown Figure 2.16 (a). Also, a longer ruler was placed across the target pool (Figure 2.17) and photographed by cameras 1 and 2 to determine the relative position of the observation windows of the two cameras. For the verification camera (camera 3), an image of a horizontal ruler (Figure 2.16 (b) was also taken to determine the image resolution and the location of each pixel along the light sheet. In addition to these images taken for the determination of image resolution, images were taken with the rulers removed,

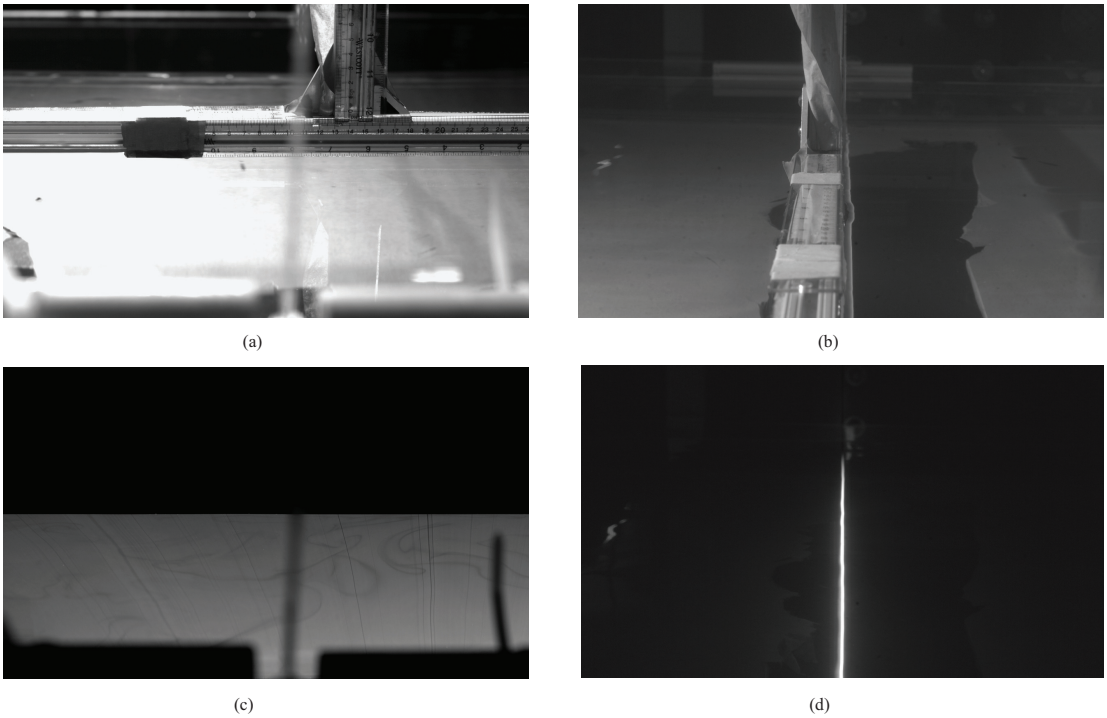

Figure 2.16: Calibration images for the LIF measurements. (a) Camera 1 image. (b) Camera 3 image. (c) Camera 1 image with laser on and no rain. (d) Camera 3 image with laser on and no rain.

the laser turned on, and the rain generator turned off. From these images, the mean water level was located in the images from cameras 1 (see Figure 2.16(c)) and 2 and the position of the light sheet was determined in the images from camera 3, see Figure 2.16(d). During these calibrations, the round tank was supplying water directly into the target pool though a garden hose to make the water overflow as it did during the rain experiment.

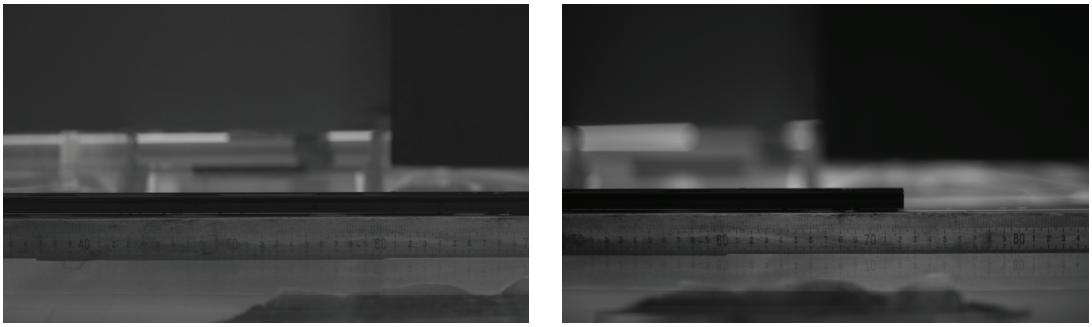

(a) (b)

Figure 2.17: Calibration images from cameras 1 (a) and 2 (b) of a ruler that spanned the fields of view of both cameras.

2.3.4 Image Processing

The water surface profiles were extracted from the digital images using gradient-based methods similar to Liu and Duncan [35]. A MATLAB program consisting of several steps was written for this purpose. In the first step of the calculations, two threshold values were determined using image intensities over all the images from one experimental run. Then, in each image all the pixels that have grey levels below and above these two thresholds are saturated to increase the contrast of images. Next, the edge function in MATLAB is used to find the edges at those points where the gradient of the image intensity is maximum. These edges at the air-water interface are connected from left to right and a spline function is used to manually connect the gaps between the edges. Finally, a smoothing function is used to create the finished surface profile.

As shown in Figure 2.18, images on the left are the LIF image of water surface inside the rain field captured by camera 1. Images on the right are the corresponding

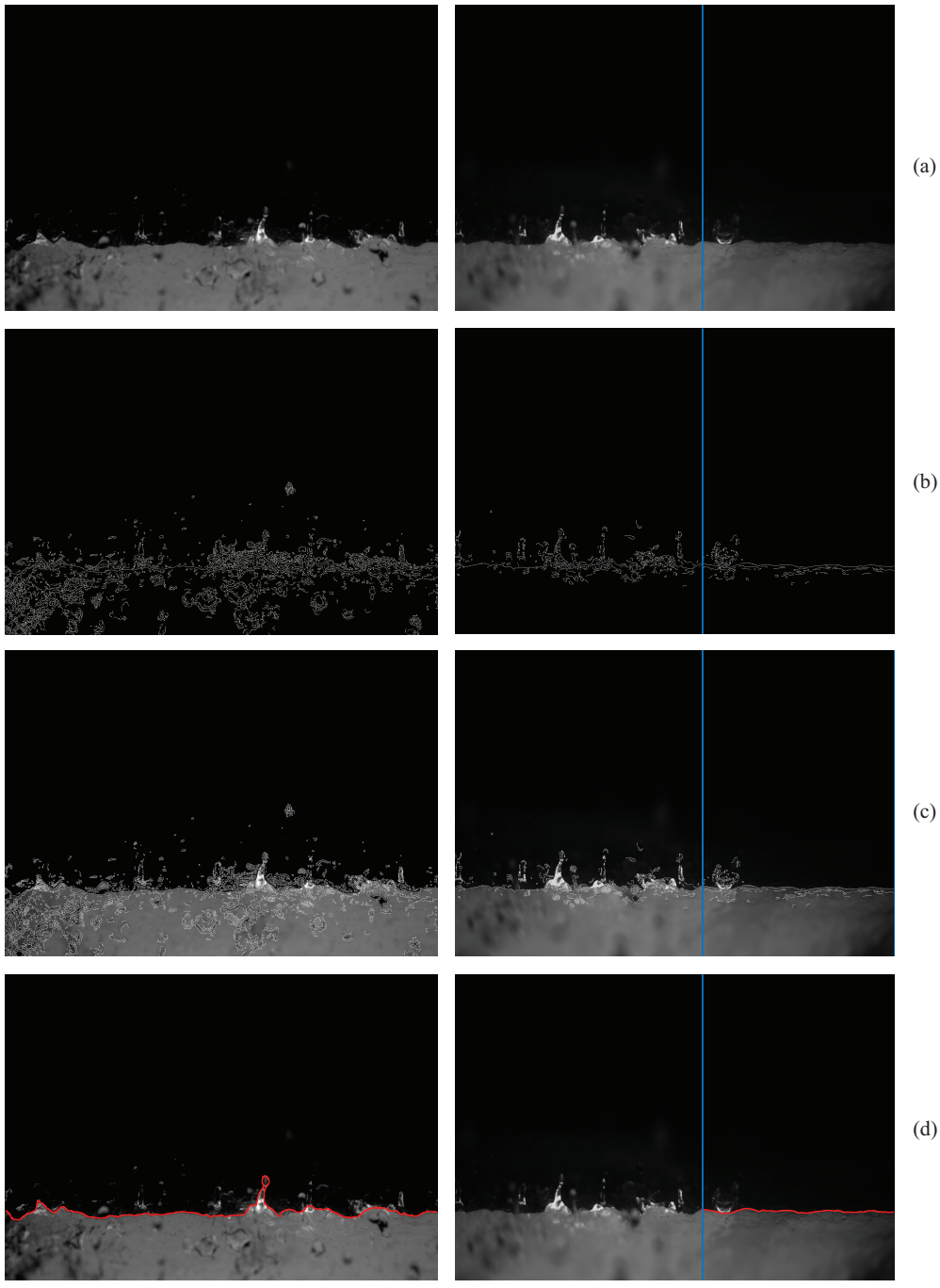

Figure 2.18: LIF image processing for extracting the surface profile. (a) Original LIF images from cameras 1 and 22. (b) Image (a) after thresholding, conversion to black and white and edge detection using canny method. (c) Images (a) with the edge detection results from (b). (d) Images (a) with the extracted surface profiles shown in red.

LIF images captured by camera 2. Only about 40% of the right images (on the right of the blue light) were processed because it indicates the region outside the rain field. Due to the chaotic nature of the water surface within the rain field, there were many discontinuities of the initial guessed surface profile and required a lot of spline fitting. On the other hand, the surface profile outside the rain field was well estimated and spline fit was rarely needed.

2.3.5 Needle Cleaning Process

Experiments for each case took about 7 to 12 hours and they were complete in one day. After a case was completed, the needles were taken off and placed in isopropyl alcohol overnight to prevent fluorescein dye or dust, which was remain inside the needle tube, getting dry and solidified. On the next day, a syringe with a two and half teflon tube was used to clean the needle by forcing a water jet through needle tube toward needle base as shown in Figure 2.19. A needle was considered cleaned, when a steady water jet could be erupted out of the needle base. If a blockage occurred due to harden dye or dust, the cleaning probes were used to poke through needle tubes before cleaning with syringe.

2.4 Simultaneous LIF and Stereoscopic PIV Measurement

The literature review showed that the subsurface flow field could effect the rain-induced surface features. To investigate the possible correlation between the water surface features associated with impinging raindrops and the subsurface flow

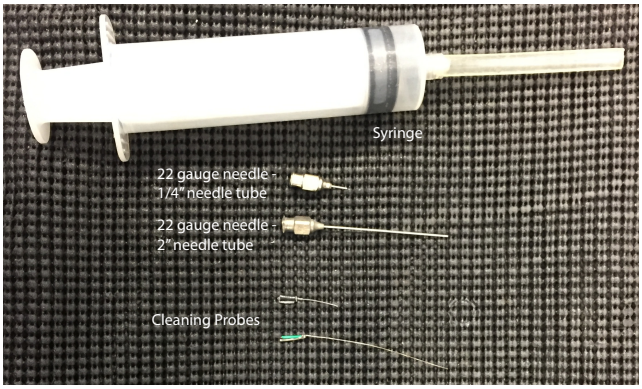

Figure 2.19: Needles and cleaning tools

field, the turbulent velocity field beneath the free surface was measured simultaneous with LIF surface profile measurement. Thus, PIV particles and experimental setup were prepared to perform LIF and Stereoscopic PIV measurements together.

2.4.1 PIV Seeding Particles

One of the problems in PIV measurements of the rain-induced sub-surface flow field is the possibility of the specular reflections of laser light in the images. These reflections can originate if the light sheet hits the air-water interface of impact craters and air bubbles. In addition, the light from LIF setup (fluoresced light) may act as background light and reduce the contrast of stereo PIV images. Thus, a special type of seeding particles were manufactured in the laboratory using Rhodamine WT dye (maximum emission wavelength of 582 nm) to solve these problems. First, Rhodamine WT dye was well mixed with epoxy in a cake pan. Then, the epoxy-Rhodamine WT dye mixtures was allowed to cure for at least 24 hours to become a solid disk. This disk was then sanded into a wide range of small particles with

a belt sander.and collected using a vacuum. Finally, the collected particles were segregated into various size ranges by using a shifter with different size sieves. Only particles that had size ranges from 25 μm to 53 μm were selected as PIV seeding particles. During the experiment, a long-wavelength-pass (cut off wavelength 562 nm) optical filter was attached in front of each stereo PIV camera lens. These filters blocked the primary light wavelengths (527 nm) of the laser and most of the fluoresced light (maximum emission wavelength of 515 nm) from the LIF setup while transmitting a sufficient portion of the fluoresced light from the Rhodamine WT dye in the particles.

The settling velocity of these PIV seeding particles were estimated using Stokes' Law:

$$V = \frac{2}{9}\frac{(\rho_p - \rho_f)}{\mu} g R^2 \tag{2.3}$$

In this equation, V is the settling velocity, g is the gravitational acceleration, ρ_p and ρ_f are the mass density of the seeding particle and water, and μ is the dynamic viscosity. The estimated settling velocity was between 0.04 mm/s and 0.20 mm/s.

The frequency response of these tracer particles was studied by Washuta [65]. Based on his analysis (Figure 2.20), for the seeding particles used in this study (ranging in diameter from 25 μm to 53 μm) the As can be seen in the figure, the square of the magnitude of the transfer function H_p between the fluid particle oscillations and the tracer particle oscillations is 95% or higher for frequencies less than or equal to 1,000 Hz.

Before each experiment, 10 g of seeding particle were well mixed with 200 ml

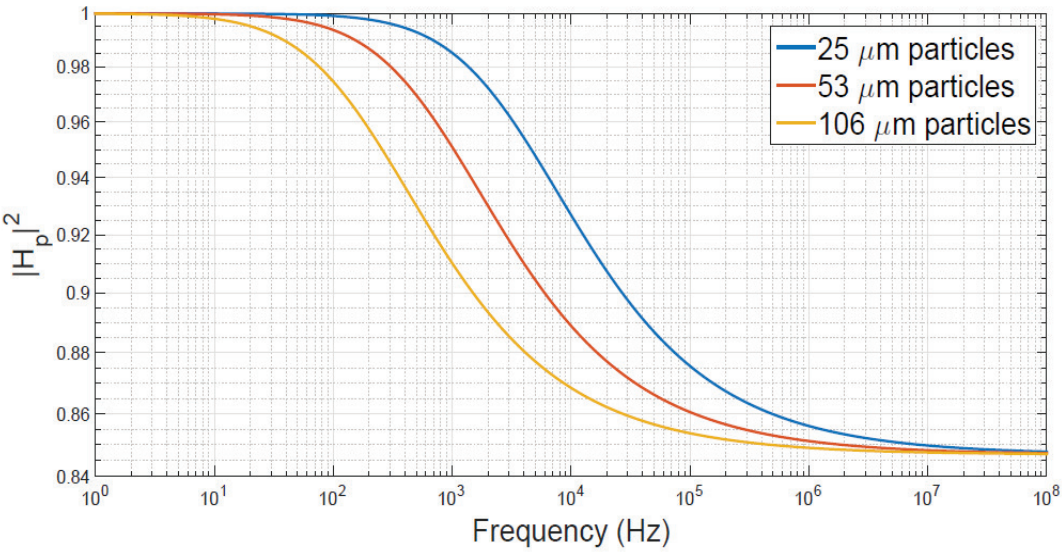

Figure 2.20: Particle frequency response for a range of particle diameters (Washuta 2016). H_p is transfer function between the fluid velocity fluctuations and the the particle velocity fluctuations of frequency f.

of isopropyl alcohol in order to prevent PIV particle clogging. Then, 110 ml of the particles-alcohol mixture was poured over the target pool. During the experiment, seeding particles density would decrease overtime due to overflow of the water and particle settling. Therefore, 30 ml of the remaining mixture was added into the target pool after every three runs to maintain sufficient particle density.

2.4.2 Experimental Setup

This measurement used four high-speed digital movie cameras (Phantom V640 & V641, Vision Research) and a high-repetition rate Nd: YLF laser to provide light source. As Figure 2.21 shown, Nd: YLF laser was set to generate a light sheet which

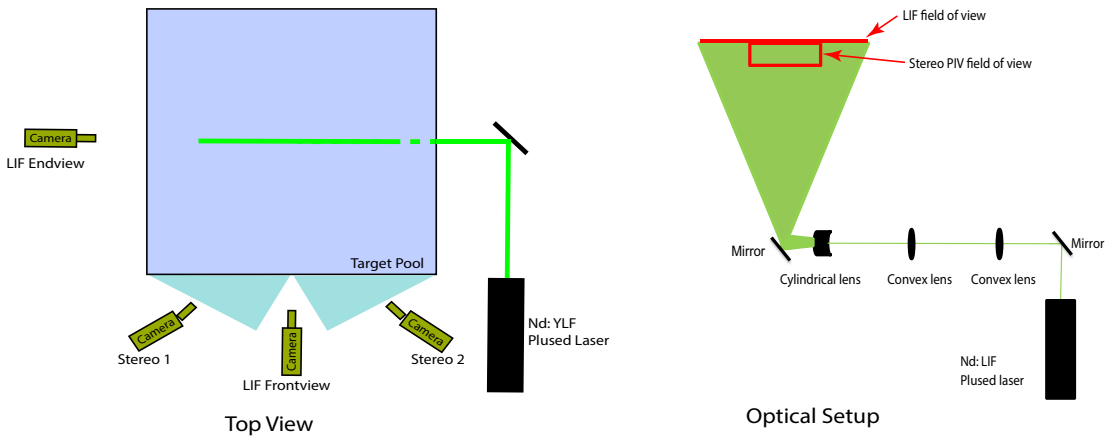

Figure 2.21: Simultaneously LIF and stereo PIV measurement setup

passed through the transparent bottom of the target pool and illuminate a light sheet vertically upward at the center line of the target pool. Two cameras were performing LIF measurement of the water surface while the other two cameras were performing stereo PIV measurement of the flow field below and they were synchronized together at a frame rate of 250 fps. To measure the out of plane velocity, two 30-60-90 triangle prim filled with water were attached to the front side of the target pool in front of the stereo PIV cameras. Each PIV camera had equipped with two Scheimpflug mount and tilted camera sensor plane to the lens plane as shown in Figure 2.22. Combining the effect of triangle prim and Scheimpflug mount, each camera could focus on a plane parallel to front side of the target pool, which was also the parallel to the light sheet.

Instead of using a long-wavelength-pass (cut off wavelength 550 nm) optical filter, a band-wavelength-pass (515 nm $\pm$ 10 nm) optical filter was placed in front of each LIF cameras in this measurement. These filters blocked the primary light wavelengths (527 nm) of the laser and the Rhodamine light (maximum emission

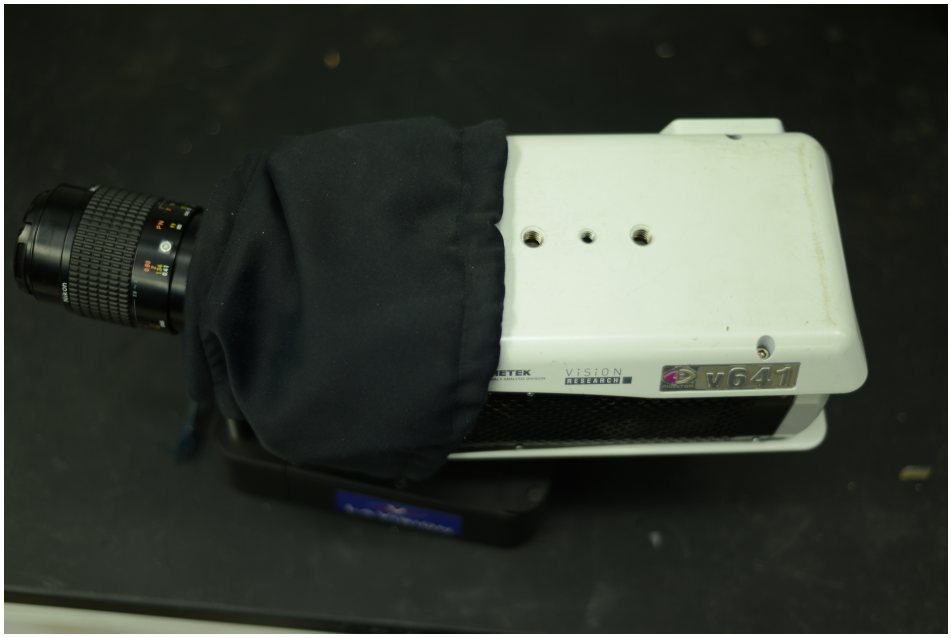

Figure 2.22: A Phantom V641 with Scheimpflug and 105 mm lens

wavelength of 582 nm) from stereo PIV particles while transmitting fluoresced light (maximum emission wavelength of 515 nm).

2.4.3 Calibration

Calibration of the LIF and Stereo PIV image was perform both before and after the experiment using DaVis software (LaVision, Inc.). The calibration target is a two-level 3D calibration plate(Type 309-15, LaVision, Inc.) as shown in Figure 2.23. It is a 309 mm by 309 mm black plate with 3mm diameter white dots. The dots are 15 mm apart and the separation of the calibration planes is 3 mm. The top plane of the calibration plate was carefully aligned with the laser light sheet before the calibration images were taken. Then, DaVis software could apply a 3rd order polynomial fit to transform camera images into real-world images by calculating the

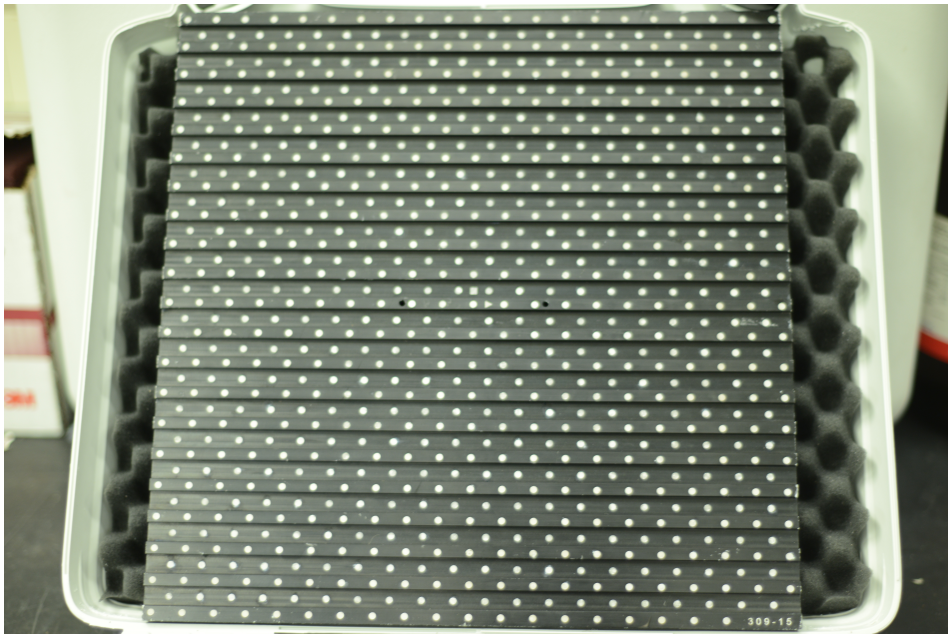

Figure 2.23: Type 309-15 calibration target

image distortion of the target plate. Using this procedure, DaVis software should properly correct image distortion due to the optical setup.

2.4.4 Image Processing

DaVis software was used to process both LIF and Stereo PIV images. LIF images were corrected only use the 3rd order polynomial fit calculated from calibration. Stereo images went through planar self-calibration method to correct misalignments between laser light sheet and calibration plane. Then, the Stereo PIV cross-correlation algorithm were apply to calculate the velocity fields.

2.5 Simultaneous LIF and Radar Measurements

To investigate the radar backscattering due to rain-induced surface features, simultaneous measurements of LIF and radar with different rain intensities and impact velocities were conducted using a 6 -12 GHz scatterometer with different incident angles.

2.5.1 Radar System

The radar system is an ultra-wide band, polarimetric radar similar to that shown in Sletten and Trizna [60], see Figure 2.24. The radar is based on a fast oscilloscope (Tektronix Model DPO72004B) that samples the radar backscatter in real time at rates of 50 GS/s. The short ultra-wideband pulse is generated through the use of an ultra-fast pulse generator (PSPL Model 4015) and a 6 - 12 GHz (X-band) solid state microwave amplifier. The combination of the amplifier response and the pulse generator rise time produces microwave pulses with a 3 dB pulse-width of approximately 0.5 ns, providing a range resolution of approximately 4 cm. A pair of 2 - 18 GHz antennas with appropriate pulse-to-pulse transmit and receive switching capability are used to collect four consecutive equivalent-time-sampled pulses at a per-polarization pulse repetition frequency of 500 Hz. One complete scan of the 1.2 m range (the width of the square target pool) swath of the radar was complete at every pulse, with (HH, HV) and (VV, VH) echoes collected on alternate scans.

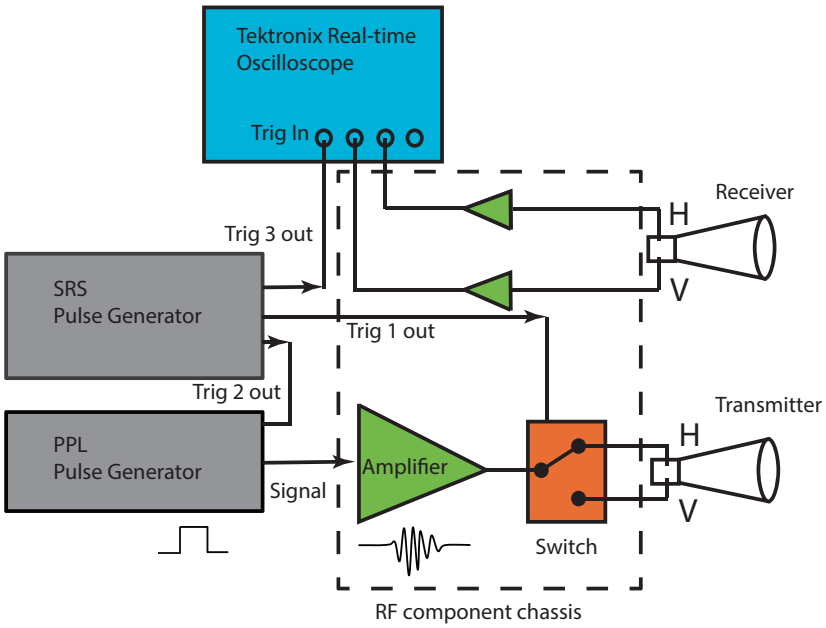

Figure 2.24: Radar design

2.5.2 Experimental Setup

The radar antennas were mounted on a sliding bar which was attached to a vertical 80/20 beam. The bar had a 90° rotating pivot at the bottom. As shown in Figure 2.25, the sliding bar allows the adjustment of the antenna height and its pivot provides different incident angles. By adjusting the sliding plate and pivoted beam, the radar antennas measured rain-induced surface features at different incident angles. Radar absorbents are installed in order to reduce the reflection of the target pool edges. The distance to the center of the rain field on the water surface from the antennas was 1.6 m, producing a bistatic angle of 9°.

The LIF measurement used 1 laser and 2 synchronized cameras as shown in Figure 2.26. A continues wave Argon-Ion laser was used and the light sheet was

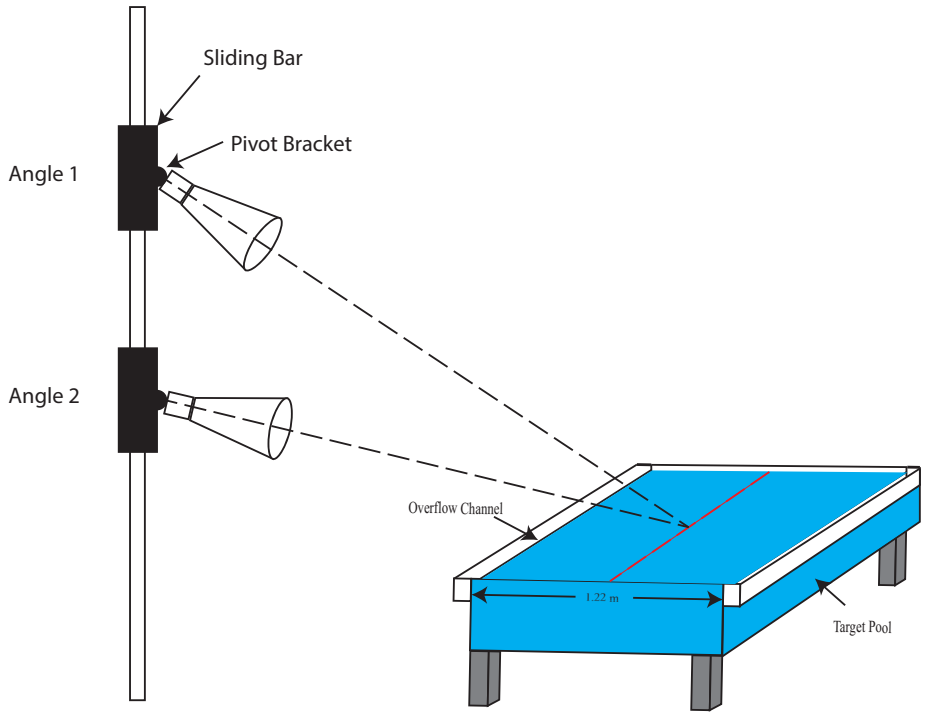

Figure 2.25: Antenna angle variation

generated the same way as in the above LIF measurement. Two high-speed digital movie cameras (Phantom V640, Vision Research) were placed side by side and set to a frame rate of 500 frames per second (fps) were synchronized using a BNC pulse delay generator. Both cameras were oriented to view the water surface from the side. Camera 1 had a look-down angle of about 10 degrees from the horizontal and focused on the bright region in front of the light sheet. It provides a overview of the number of stalks presented in the front half of the rain field for a particular radar pulse. The second camera focused on the light sheet (performing LIF measurement) with a look-down angle of about 6 degrees from the horizontal.

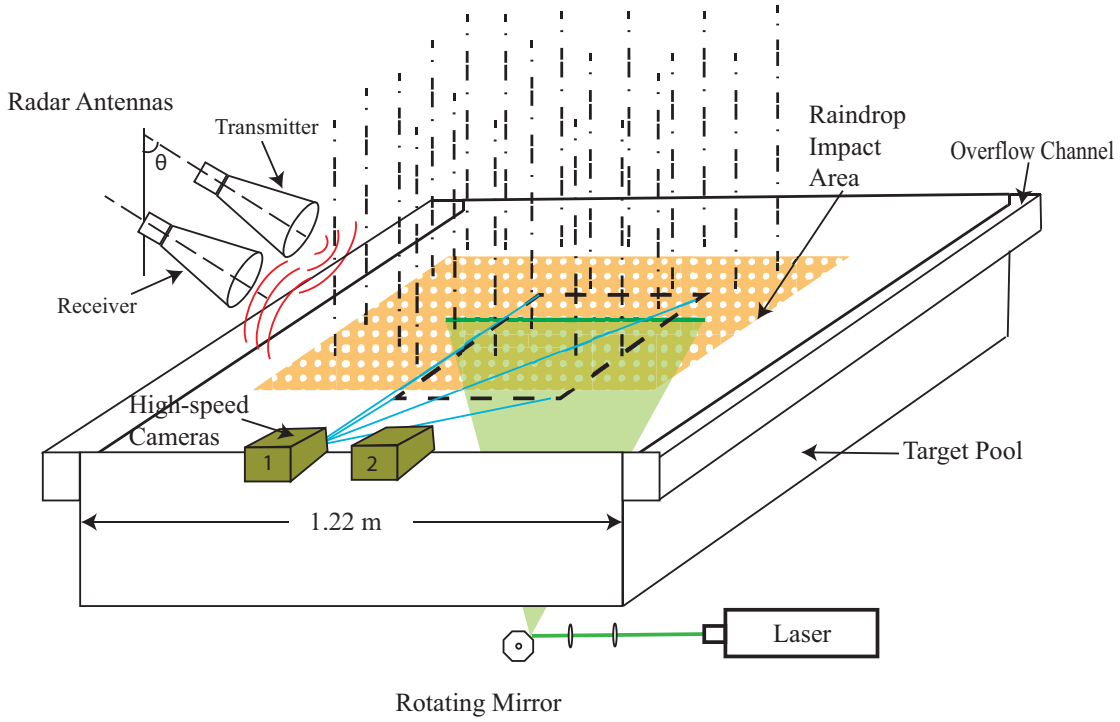

Figure 2.26: Experimental setup of synchronized radar measurement and LIF

2.5.3 Calibration

Two spherical targets were used to calibrated the radar travel distant and radar backscattering power. As shown in Figure 2.27 (a), a 5.1 cm diameter (slightly bigger than the radar range resolution of 4 cm) plastic ball was placed with known distance relative to the square target pool and its image was captured by both cameras to indicate the relative position of the two cameras. Then, the ruler was removed and the radar signal of the plastic target was record. Next, the radar backscattering signal of the metal spherical target was record as shown in Figure 2.27 (b). Finally, the LIF images and radar backscattering signal of an overflowing water surface without rain was also recorded (Figure 2.27 (c)).

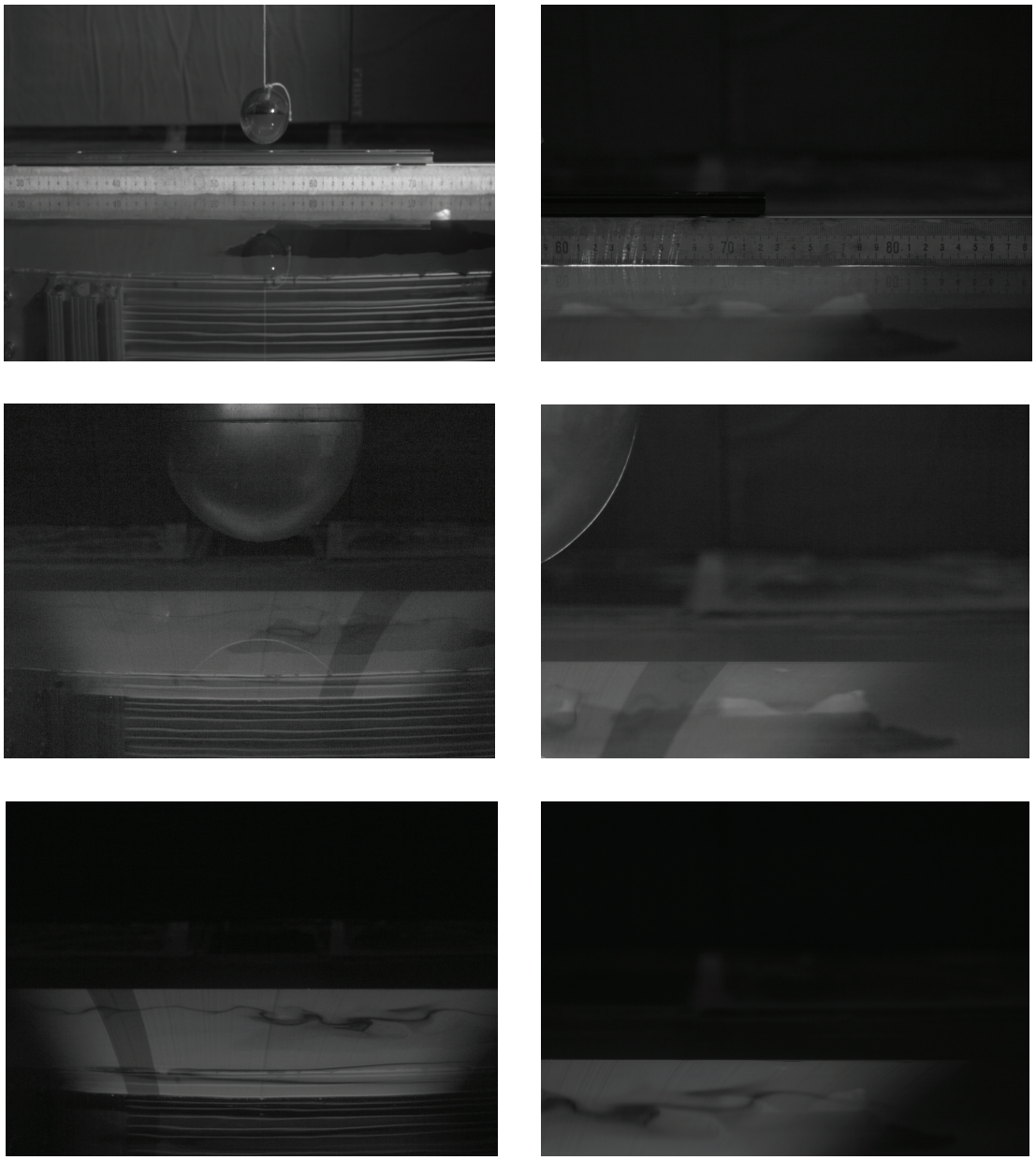

Figure 2.27: Radar calibration images. (a) Calibration images from cameras 1 and 2 of a ruler that spanned the fields of view of both cameras and the position of a plastic spherical target is measured. (b) The position of a metal spherical target is measured. (c) The mean water level is measured.

2.5.4 Radar Signal Processing

The radar return signal in the present study consists of four waveforms (HH, HV, VH, VV). The raw data of the radar backscattering signal is recorded as voltage vs. time. Using the radar backscattering from the plastic spherical targets and the back edge of the target pool, the time can be converted to space with the following formula

$$x = \frac{ct}{2\sin(\theta)} \tag{2.4}$$

where c is the speed of light, t is the time, and θ is the incident angle. The backscattering power strength was then calculated by comparing it to the backscattering signal of the metal spherical target.

Chapter 3: Results and Discussion

3.1 Single Drop Impact

Single drop impact experiments were performed at 11 different needle heights (H_d, defined as the vertical distance between the free end of the hypodermic needle and the undisturbed surface of the target pool). For the lowest 9 heights, the experiments consisted of ten individual drop impacts, while for the two highest heights, the experiments consisted of 30 drop impacts. The data resulting from these experiments is given in Table 3.1. As can be seen in the table, the droplet diameters were nearly the same for all needle heights; the average of the average diameters for each case is $\overline{D}_{ave} = 2.66$ mm and the standard deviation is only ± 0.08 mm. On the other hand, the impact velocity varies substantially from $\overline{V}_{ave} = 2.15$ m/s at the lowest needle height to 7.2 m/s for the highest needle height. The impact Froude and Weber numbers,

$$Fr_{ave} = \frac{V_{ave}^2}{gD_{ave}} \qquad \text{and} \qquad We = \frac{\rho V_{ave}^2 D_{ave}}{T}, \tag{3.1}$$

varied from from 176 to 2,011 and 172 to 1,893, respectively. Because of the definitions of Fr and We, the fact that all experiments were performed in water, and the fact that D_{ave} is nearly the same for all experimental conditions, Fr and Br are

$H_d(m)$	$V_{ave}(m/s)$	$V_\sigma(m/s)$	$D_{ave}(mm)$	$D_\sigma(mm)$	Fr	We	H^*	H^*_σ
0.25	2.15	0.01	2.68	0.05	176	172	-	-
0.51	3.0	0.01	2.66	0.02	345	332	4.66	0.27
0.71	3.4	0.01	2.61	0.02	451	419	5.53	0.13
0.91	3.9	0.02	2.67	0.03	581	564	5.74	0.26
1.4	4.6	0.06	2.82	0.05	765	829	6.44	0.30
1.9	5.3	0.03	2.73	0.04	1050	1065	7.08	0.26
2.4	5.7	0.03	2.72	0.03	1219	1227	8.29	0.24
2.9	6.1	0.04	2.68	0.06	1417	1385	9.60	0.54
3.4	6.6	0.05	2.58	0.02	1723	1561	11.3	0.37
4	6.9	0.07	2.53	0.1	1920	1673	10.2	1.92
4.8	7.2	0.06	2.63	0.03	2011	1894	8.67	2.89

Table 3.1: Experimental conditions and measurements for the single drop impact experiments. H_d is the vertical distance from the bottom of the hypodermic needles to the water free surface in the target pool. V_{ave} and V_σ are the average and standard deviation of the drop impact velocities, respectively. D_{ave} and D_σ are the average and standard deviation of the drop diameters, respectively. $Fr = V_{ave}^2/(gD_{ave})$. $We = \rho V_{ave}^2 D_{ave}/T$. H^* and H^*_σ are the average and standard deviation of H/D_{ave} where H is the measured stalk height for each drop impact.

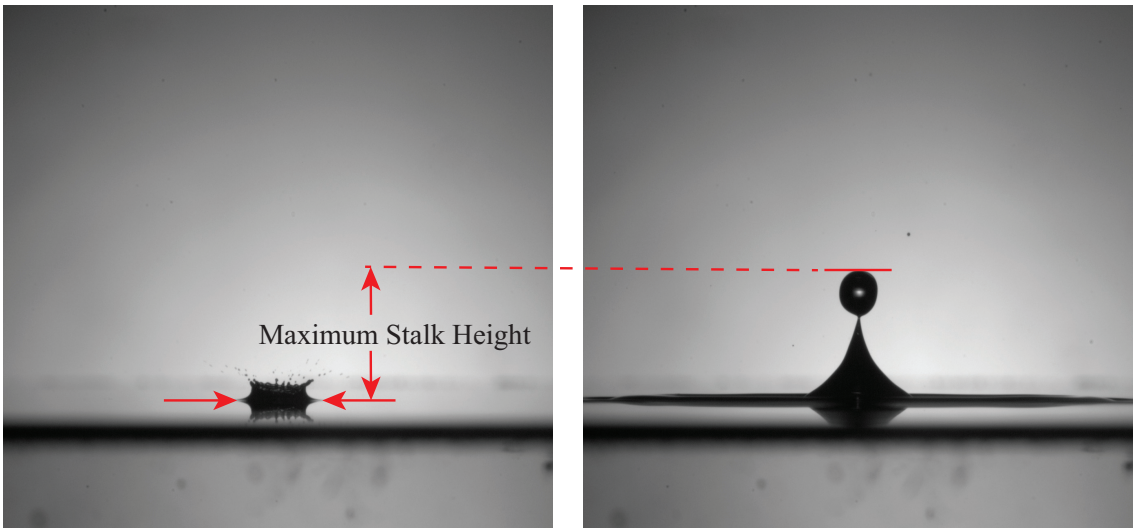

Figure 3.1: The determination of maximum stalk height. Images from an experiment with $Fr = 345$.

nearly proportional to one another in the present experiments as is demonstrated by the plot of Fr versus We in Figure 3.5. This proportionality results in a nearly constant Bond number,

$$Bo = We/Fr = \frac{\rho g D_{ave}^2}{T}, \tag{3.2}$$

of 0.966 $\pm$.060.

Variations in the stalk behavior as the impact Froude number changes creates some ambiguity in measuring stalk height. In the present study, the maximum stalk height is defined as the vertical distance from the undisturbed water level to the to the highest point reached by the top of the stalk without or before a tip drop pinches off from the upper end of the stalk. This is shown schematically in Figure 3.1 for a case with $Fr = 345$. In this experimental run, an instant in time after the second image, the drop separated from the stalk. More complex behaviors occur at low Froude numbers as shown in a study by Rein [53]. Image sequences

from Rein's study for three drop impacts are shown in Figures 3.2(a), 3.2(b) and 3.3 and correspond to Fr = 120, 177, and 305, respectively. For the two lowest Froude numbers, Figure 3.2, tiny droplets are ejected upwards while the stalk is still growing. A similar sequence of images for the $Fr = 176$ case from the present study is shown in Figure 3.4(a). As in Rein's study, small droplets are ejected from the stalk while it is still growing. Thus, in these low Froude number cases, one is not certain how to define a maximum stalk height. At the next lowest Froude number (345), no small droplets are ejected. Because of the small droplet ejections, no value of stalk height has been assigned to the Fr = 176 case in the present study; see Table 3.1. Thus, the maximum stalk height variation studied herein correspond to Froude numbers ranging from of 345 to 2011 and Weber numbers ranging from 332 to 1,894, including 10 experimental conditions. According to Rein's [53] classification, the stalks in for Froude numbers ranging from 345 to 1050 the present experiment are all in the "thick jet" regime, while the case with the lowest Froude number, $Fr = 176$ is in the thin jet regime; see Figure 3.4.

The average and standard deviation of the dimensionless stalk height ($H^* = H/D_{ave}$) measurements at each of the 10 experimental conditions are given in Table 3.1 and plotted versus Fr in Figure 3.6. As Fr is increased, H^* at first increases nonlinearly, then increases linearly at a higher rate and finally decreases. In addition to the data, several lines are plotted. The blue dash-dot line is Fedorchenko and Wang's theoretical model [15],

$$H^* = 1.43Fr^{1/4}, \tag{3.3}$$

which, in their work, was favorably compared to experimental data with a 70% glycerol-water solution in a relatively shallow pool, depth equal to $6D_{ave}$. The theory was based on images from experiments with $100 \leq Fr \leq 1,000$, droplet diameters greater than 3 mm and three approximations: (1) all of the kinetic and surface tension energy of the drop, $M\frac{1}{2}V^2$ (where M is the mass of the drop), is converted to the potential energy of the stalk, which is taken as a vertical right circular cylinder and (2) all the kinetic and potential energy of the drop is converted to the crater which reaches a stationary maximum size just before the jet forms, and (3) the mass of the stalk is equal to the added mass of the crater.

In the present experiment, where the droplets were between 2.5 to 2.8 mm in diameter, clean water was used and the water depth was $114D_{ave}$, the stalks in the Froude number range from were not very close in shape to the right circular vertical cylinders assumed in the theory, see figure 3.9. Therefore, the images from the experiment were used to calculate the total mass of the stalk and the induced mass of the crater by using the following method; see Figure 3.7. First, the crater diameter was determined from the image taken when the bottom of the crater reached its maximum depth and the crater induced mass was approximated by treating it as a perfect hemisphere. The tip droplet diameter was calculated in the same way as the impinging droplet diameter as described in section 2.2.4. For this calculation, the image used was one frame after (0.5 ms after) the tip drop detached from the stalk. Next, the remaining part of the stalk was divided into different sections and treated as truncated cones using the image of the frame just before the tip drop was detached from the stalk. Finally, the mass of a stalk was approximated by adding

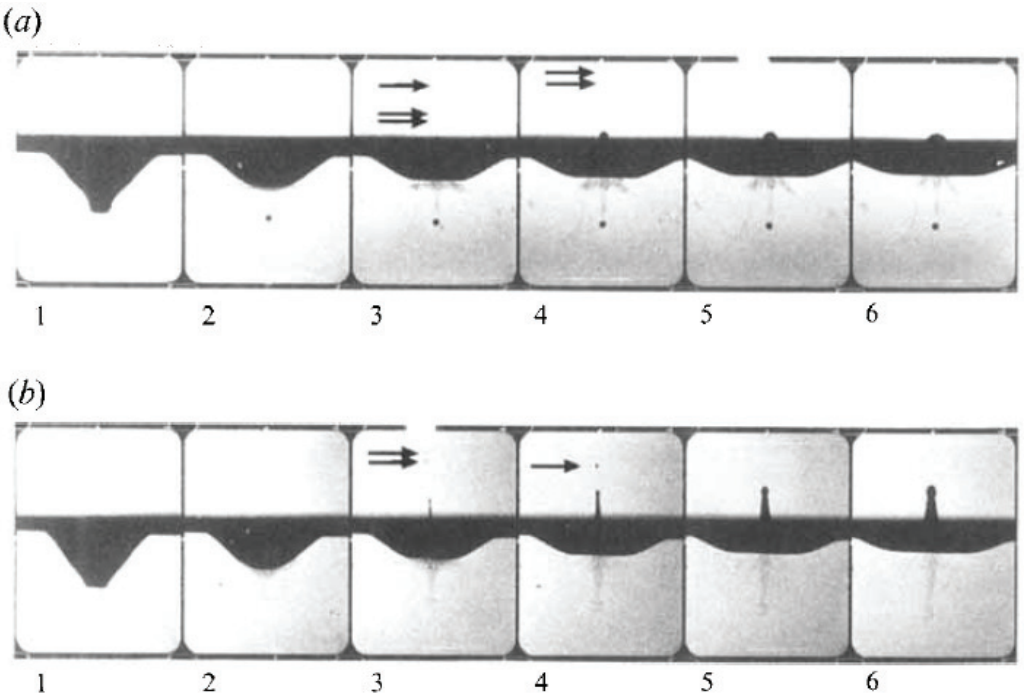

Figure 3.2: Photographic sequences begin shortly before the crater bottom reverses its motion (Rein 1996). Small arrows are pointing at the small droplets. (a) Formation of a thick jet ($Fr = 120$, $We = 102$). (b) Formation of a thin jet ($Fr = 177$, $We = 125$).

the mass of the tip drop, and the mass of all the truncated cones together. From this mass approximation, it was found that about 80% of the induced mass of the crater was later converted into the mass of the stalk. Thus, Fedorchenko and Wang's theoretical model was scale by 0.8:

$$H^* = 0.8 * 1.43 Fr^{1/4}. \tag{3.4}$$

This new equation is plotted as a blue solid line in Figure 3.6 and agrees well with the experimental data.

For Froude number between above 1050 but less than about 1800, images

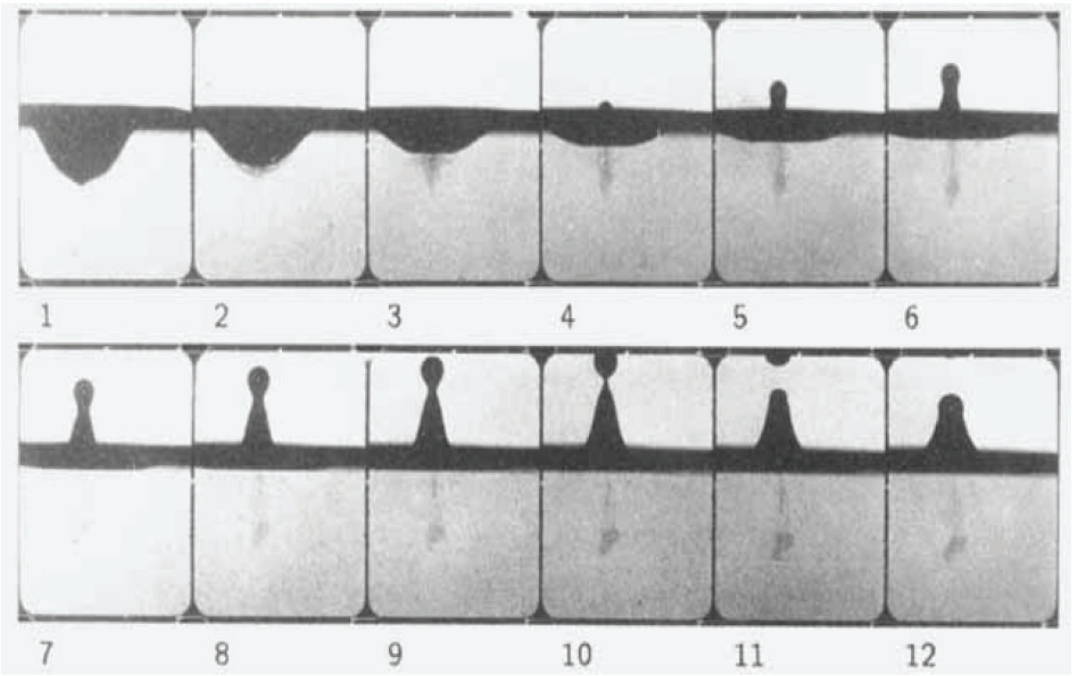

Figure 3.3: Photographic sequences begins at the moment when the base of the crater reverses its motion and form a thick jet for $Fr = 305$, $We = 219$ (Rein 1996).

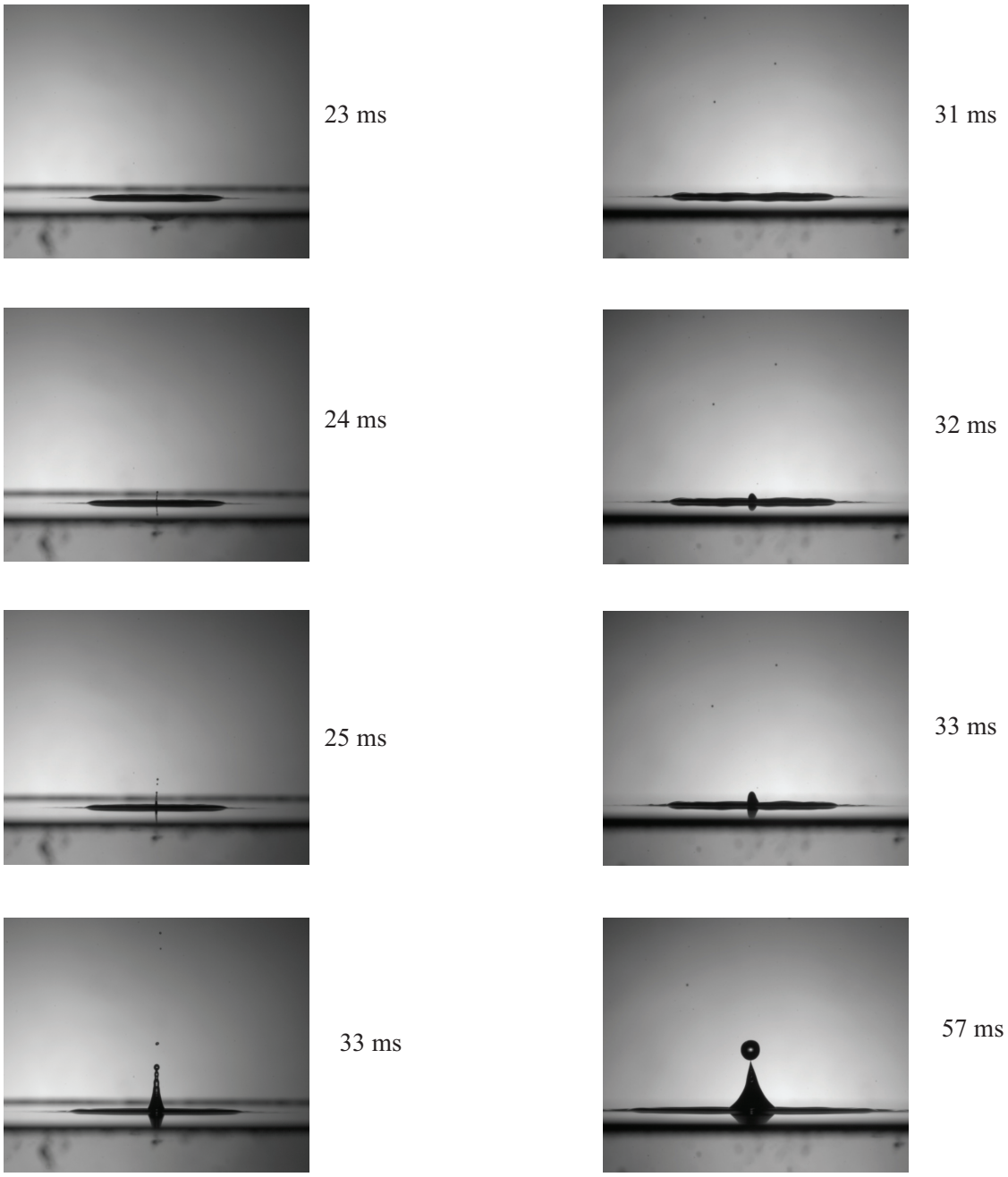

Figure 3.4: Photographic sequences begins at the moment when the droplet impact the water surface. (a) Formation of a thin jet ($\mathrm{Fr}_{ave} = 176$) and small tip droplets are constantly generated when the stalk is rising. (b) Formation of a thick jet ($\mathrm{Fr}_{ave} = 345$)

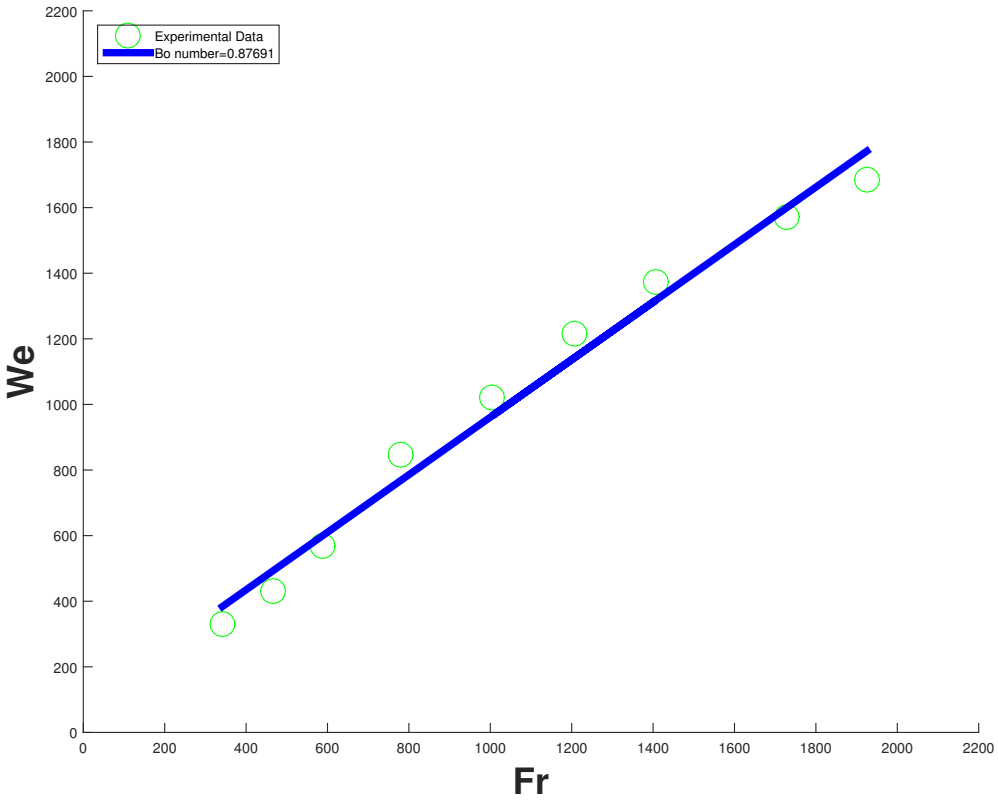

Figure 3.5: Non-dimentional Single Drop Impact Condition

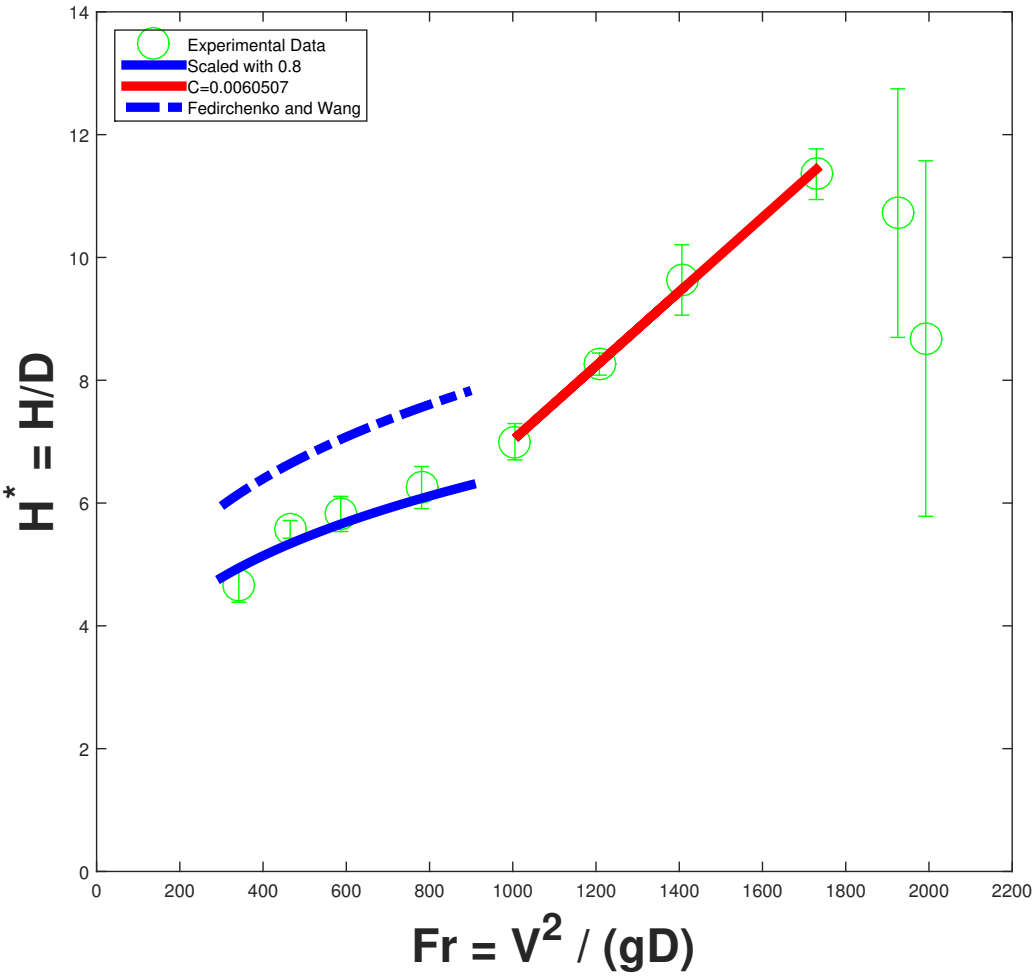

Figure 3.6: Single drop impact-induced stalk height H^* Vs. Fr

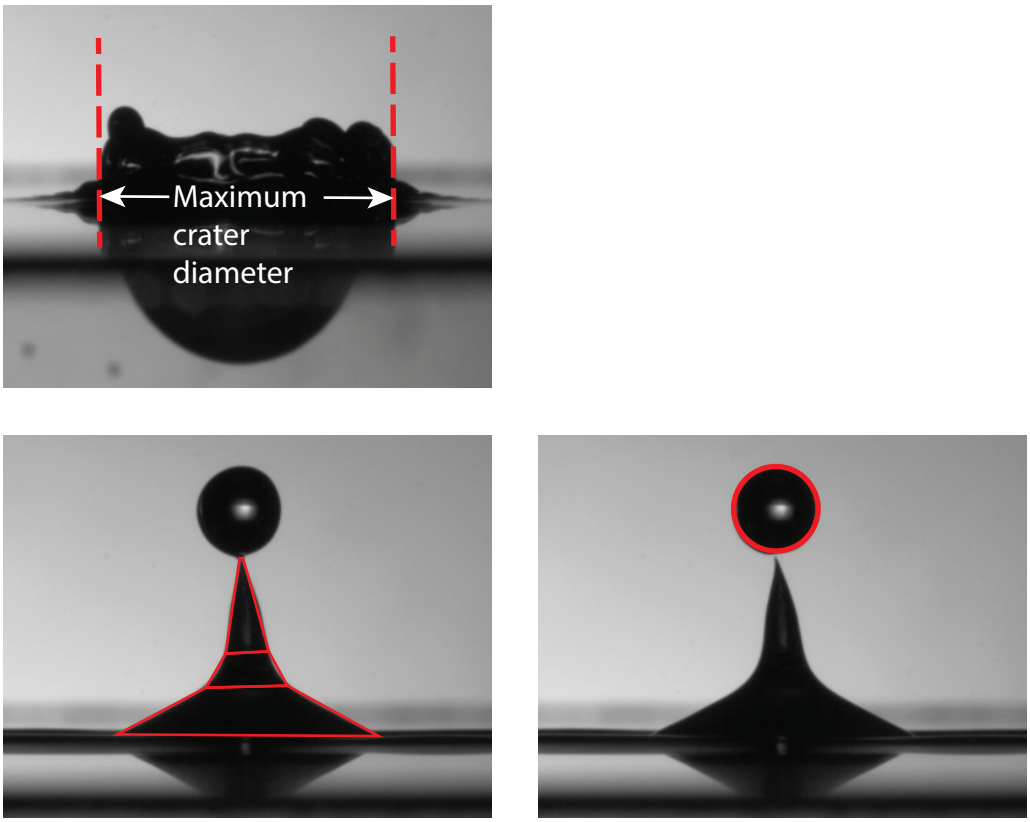

Figure 3.7: Mass Approximation: The mass of the induced mass by crater is approximated using the maximum crater diameter (between red dash lines). The mass of a stalk is approximated by treating it as a tip drop, and truncated cones (plotted by red solid lines)

of the stalk formation are shown in Figure 3.10. In this region of Figure 3.6, H^* increases linearly with Fr. The straight line with slope 0.006 plotted in the figure was obtained by a least squares fit to the data. Comparing the shape of the stalk between Fr = 300 to Fr= 1800 as shown in the Figure 3.9 and 3.10, their shapes are similar. All of the stalks have a large base, a narrow neck and a tip drop that detaches from the stalk at the end. The bases and tip drops of all cases had similar size, but the length of the narrow neck between the base and the tip drop increased with increasing Froude number. For impacts with Froude number greater than 1000, the mass of a stalk was also approximated and the ratio of the mass of a stalk to the induced mass of the crater was found to be about 1.2. This means that at maximum height the mass of the stalk was greater than the induced mass of the crater. This gives some indication of the reason for the rapidly increasing stalk heights in this region; however, the root cause of this behavior is not known.

It is also interesting to note that all the stalks are in the thick jet of the Froude versus Weber number plot given by Liow [33]; see Figure 3.8 shown. The red dash line is the fitted Bo numbers using Froude and Weber number calculated from the present 10 single drop impact experiments. The upper portion of the red line, which extends outside Liow's graph, indicates single drop impacts with Froude number greater than 1000.

The time for a stalk to reach its maximum height and the mechanism which causes tip drop formation were also investiagted. Figure 3.9 and 3.10 show the time instance around the maximum stalk hight. For Froude number between 300 and 1800, stalks are getting higher as the Froude number (impact velocity) increase and

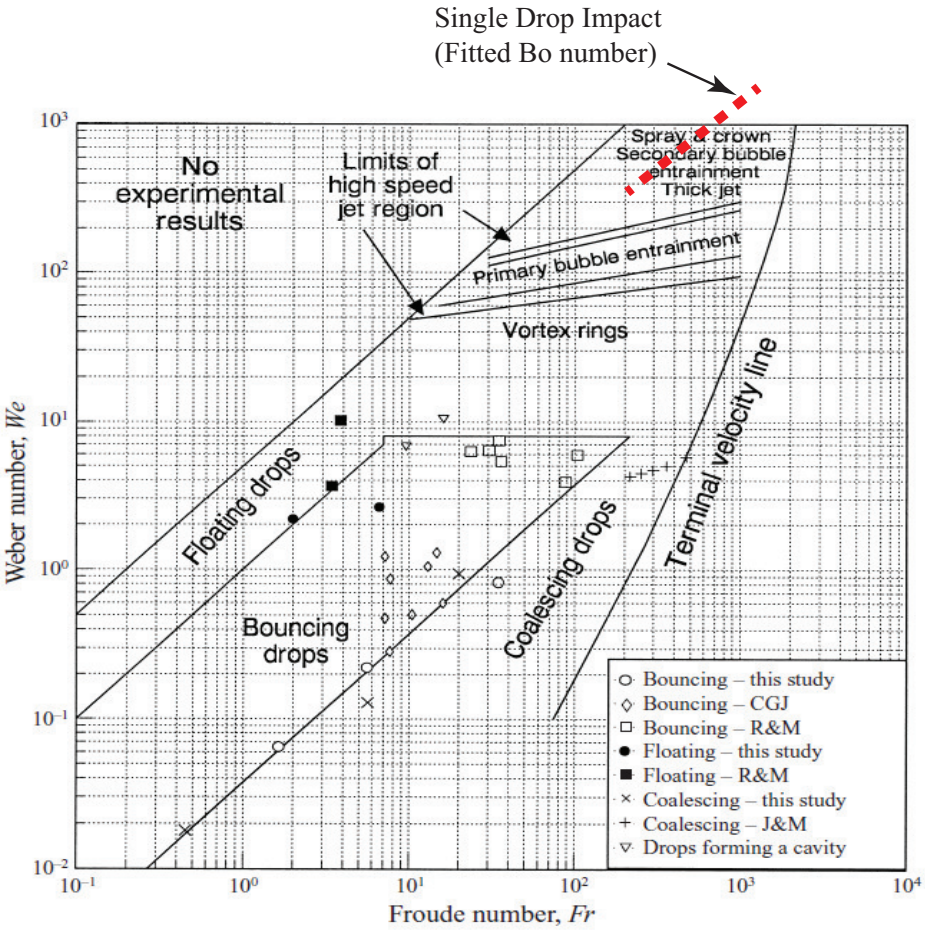

Figure 3.8: Different Regimes for Single Drop Impact (Liow 2001)

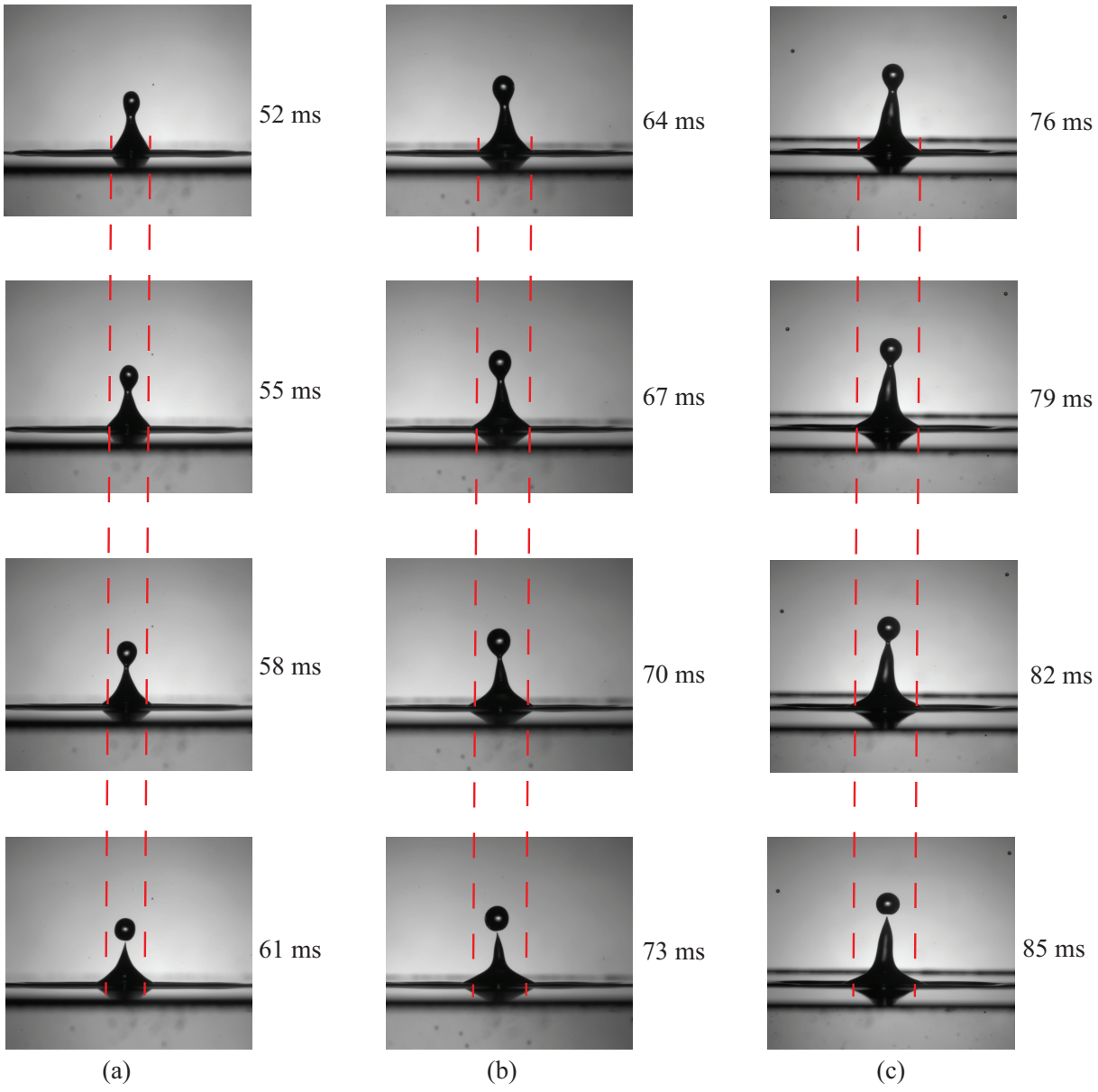

Figure 3.9: Photographic sequences begins at the moment when the droplet impact the water surface. (a) $\mathrm{Fr}_{ave} = 347$ (b) $\mathrm{Fr}_{ave} = 586$, (c)$\mathrm{Fr}_{ave} = 1005$

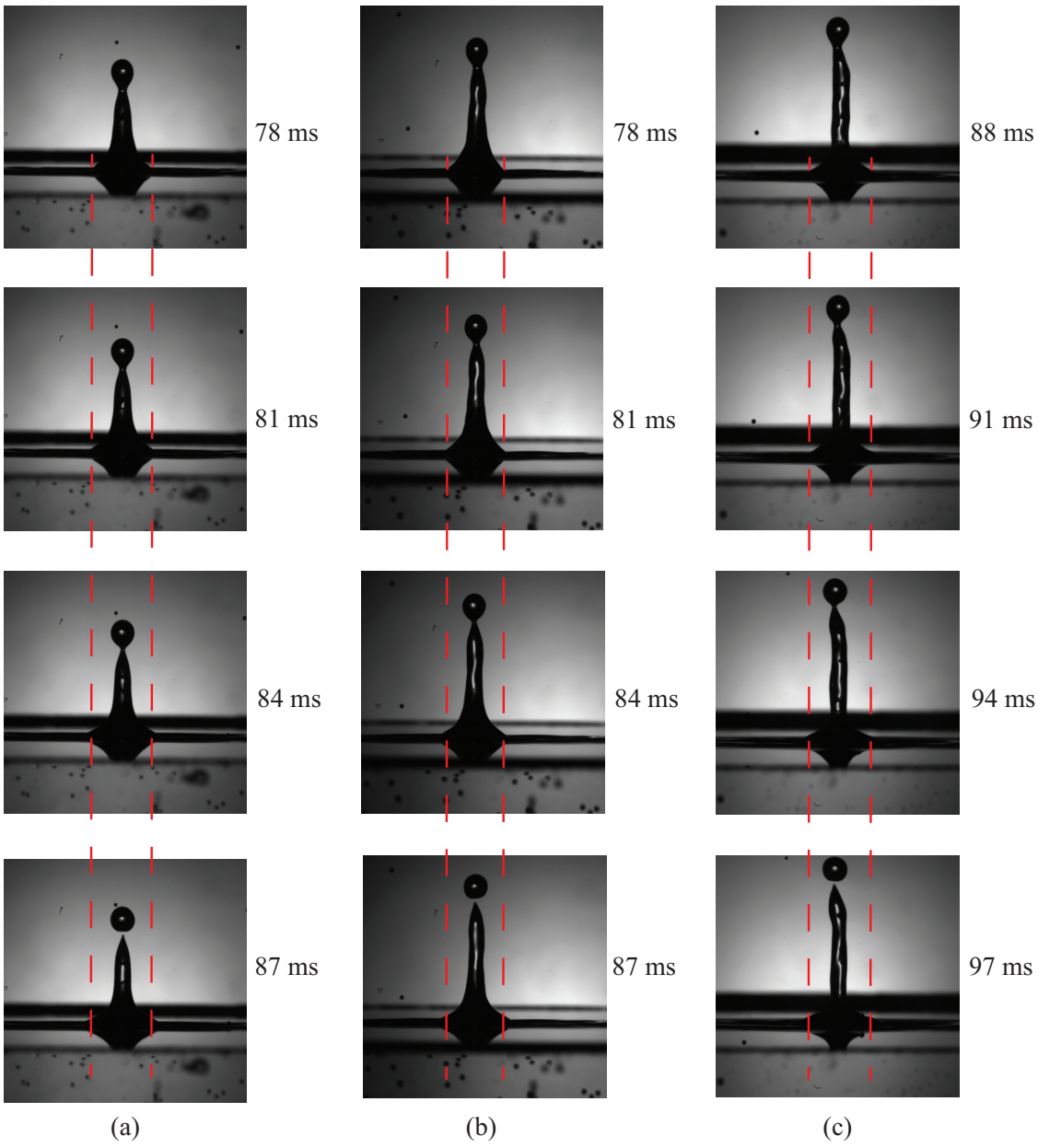

Figure 3.10: Photographic sequences begins at the moment when the droplet impact the water surface. (a) $\mathrm{Fr}_{ave} = 1208$ (b) $\mathrm{Fr}_{ave} = 1406$, (c)$\mathrm{Fr}_{ave} = 1729$

the time for the stalk to reach the maximum height is increased as well. However, the mechanism causes tip drop formation was different. For Froude number between 300 and 1000, the bottom half of the stalk started to retract indicted by its base spread to the side while the tip of the stalk still remained at the same height (the red dash lines there to help better observe the slight change in the base diameter). Then, a tip droplet was form due to the retraction of the water at the bottom. Thus, this formation was dominated by the gravitational force verse surface tension force. For Froude number between 1000 and 1800, the base did not spread as much as the lower Froude number cases, and the tip droplet was continuing moving up after it pinched off from the tip of a stalk. Thus, the tip droplets were form due to the upward motion of the tip of the stalks i.e apply force verse surface tension force.

For Froude number greater than 1800, the standard deviation was suddenly increased. The average stalk height is getting lower as the Froude number increases. That is because the impact condition enter the region where the flow condition after the collapse of a crater is random as Figure 3.11 shown. Even though these three cases has similar size initial droplets and they had the similar shape before impact (T = -1 ms), three different surface responses occurred. For Figure 3.11(a), a regular stalk appeared. For this type of response, the stalk height increased linearly with the Froude number. For Figure 3.11(b), the stalk was intercepted by the tips of the crown and resulted a stalk with reduced maximum height. For Figure 3.11(c), the crown closed and formed a larger air bubble. Thus, the maximum stalk height was limited by the height of the air bubble as shown in Figure 3.12. For these three cases, the droplet impact and target pool conditions were nearly identical and the

surface response is not much different up to 10 ms after impact. However, from case (a) to (c), the crater opening decreased and in case (c) the crater closed 20 ms after impact. The difference between cases (a) and (b) became visible at about 40 ms after impact. Case (a) left enough space for a stalk to rise up while in case (b) the gap was smaller than the stalk diameter. From this point on, the average stalk heights were lower as the Froude number increased. That is because the crown enclosure appeared more often at higher Froude number. However, the experiments condition were too few (only took place at two different Froude number) to predict its general behavior. In addition, there is not enough repeated runs (only 20) to make statistical analysis for such a random outcome either.

3.2 Rain Field Measurements

Surface profile measurements were performed for eight rain conditions generated from three rain intensities, four rain generator heights, two needle lengths and four needle arrangements. The rain conditions and the measurements performed are given in Table 3.2. The resulting raindrop velocities at impact ranged from 3.8 to 7 m/s and the rain intensity ranged from 85 mm/hr to 300 mm/hr. Stalk height distributions were measured for the full field concentered and full field scattered needle arrangements described in Section 2.1.5. The half field arrangements were used to study the surface waves within and outside of the rain fields. Flow field measurements were performed at three conditions created from two rain intensities with the rain generator at two heights. The radar backscattering power was mea-

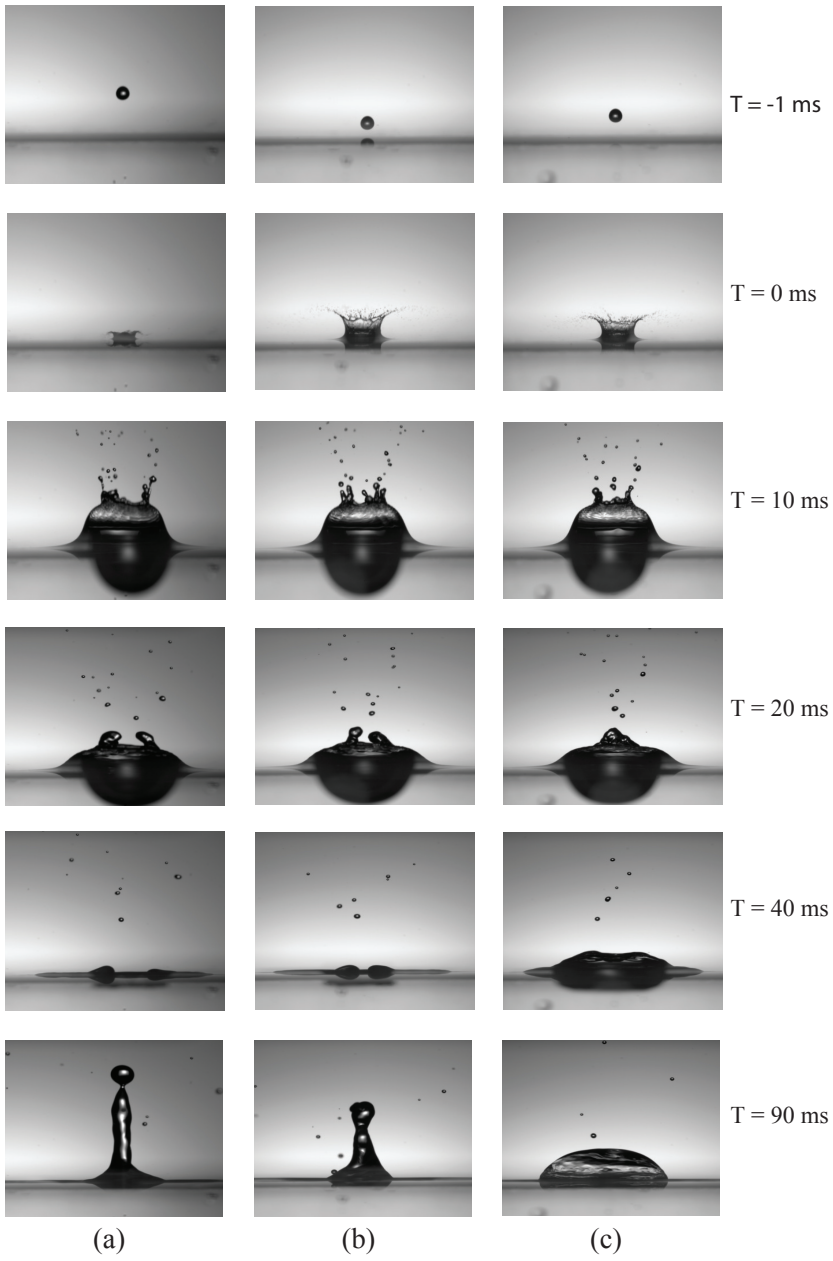

Figure 3.11: Photographic sequences for 4.8 meter single drop impact, $Fr = 2,011$. The time when the droplet impacts the water surface is taken as $T = 0$. The behavior after the collapse of the crater at $T = 40$ ms is random. (a) Formation of a regular stalk. (b) A stalk is intercepted by the crown and its height is reduced. (c) An irregular bubble entrainment occurs and the stalk height is limited.

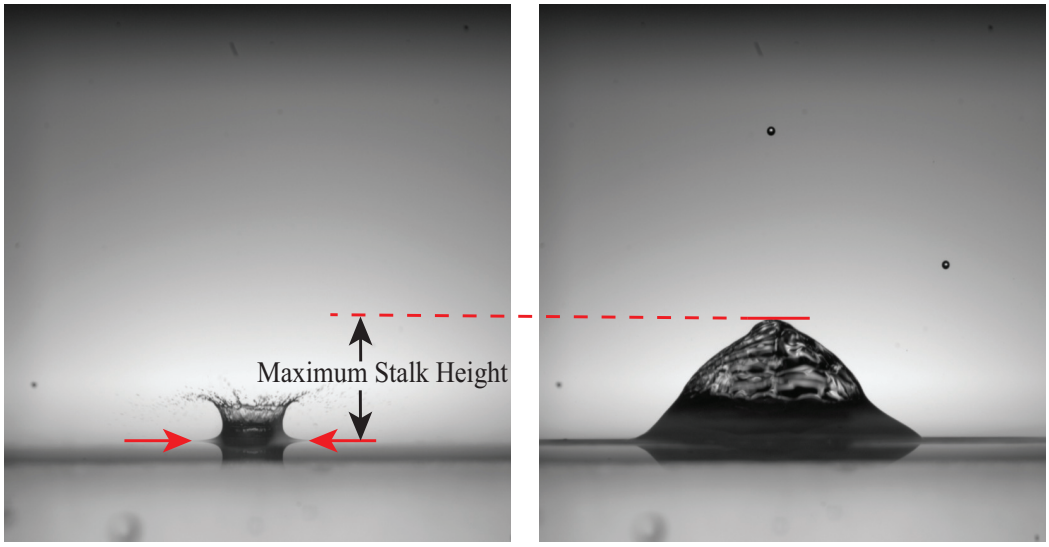

Figure 3.12: How to determine the maximum stalk height when irregular air entrainment bubble occurs

sured for four conditions created from three rain intensities and two rain generator heights. The results from the various measurements are discussed below.

3.2.1 Raindrop Impact Conditions

Raindrop diameter and impact velocity were measured by the cinematic shadowgraph technique described in Chapter 2. At each height about 20 to 50 raindrop impact events were recorded and the raindrop diameter and velocity at impact were extracted from the shadowgraph images by the same process used in the single drop measurements. The resulting raindrops had diameters between 2.3 and 3.1 mm as shown in Figure 3.13. The drop diameter variation could be due to several reasons. First, the inner diameter of needles are not perfectly identical even though the were all 22 gauge needles. Second, dust and the dye added to the rain tank might clog

H_d (m)	NA	NL	V_{ave} (m/s)	D_{ave} (mm)	R (mm/hr)	Fr	SPIV	LIF	Radar
0.85	S	St	3.78	2.77	130	526	-	x	-
1.5	S	St	4.66	3.04	130	728	-	x	-
2.2	S	Lg	5.59	2.58	85	1,235	-	x	-
2.2	S	St	5.61	2.66	130	1,206	-	x	-
2.2	C	St	5.66	2.84	300	1,150	x	x	x
4.8	S	Lg	7.04	2.41	85	2,096	-	-	x
4.8	S, HS	St	6.83	2.44	130	1,949	x	x	x
4.8	C, HC	St	7.02	2.44	300	2,059	x	x	x

Table 3.2: Experimental conditions and measurements for the rain experiments. H_d is the vertical distance from the bottom of the hypodermic needles to the water free surface in the target pool. NA is the needle arrangement discussed in Chapter 2, where C represents the full field concentrated arrangement, HC stands for half field concentrated, S is for full field scattered, and HS is for half field scattered. NL is the needle length, where Lg is for long needles and St stands for short needles. V_{ave} and D_{ave} are the average of the raindrop impact velocities diameters, respectively. R is the resulting rain intensity. "x" means a measurement is performed and "-" means otherwise.

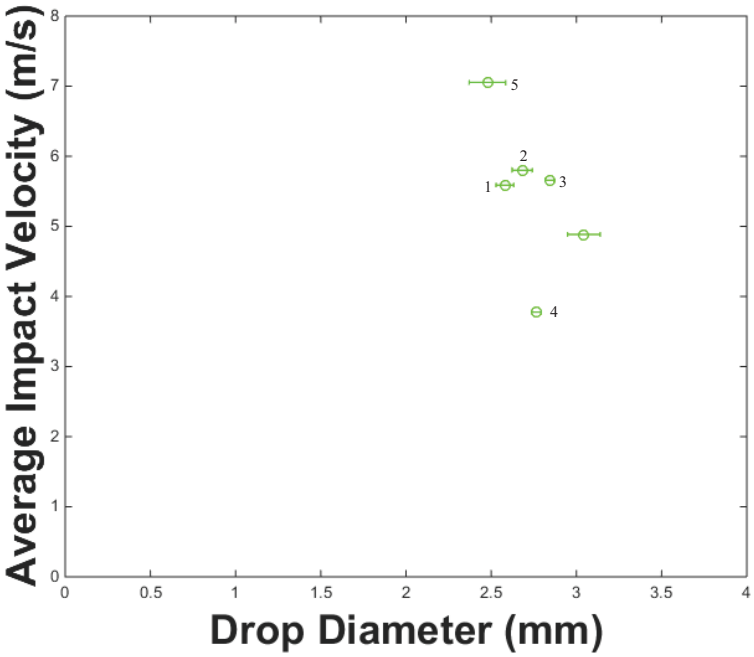

Figure 3.13: Raindrop impact condition

the needles and reduced their working inner diameter over time. Third, the rain generator motion may induce vibrations to the needles and cause raindrops to fall off before they would under static conditions. Fourth, the water level inside the rain tank was varied to accommodate different needle lengths and to achieve different rain intensities. Possible variations due to needle ID variations are the due to manufacturing and cannot be controlled. Diameter variations due to water level changes are desired and controllable. However, diameter variations due to needle clogging and the rain generation motion need to be prevented and measured, respectively.

To investigate the raindrop diameter variation overtime due to possible needle clogging, nine separate raindrop measurements were conducted over a 7 hour period in which the rain generator remained on at constant conditions. A condition with 22

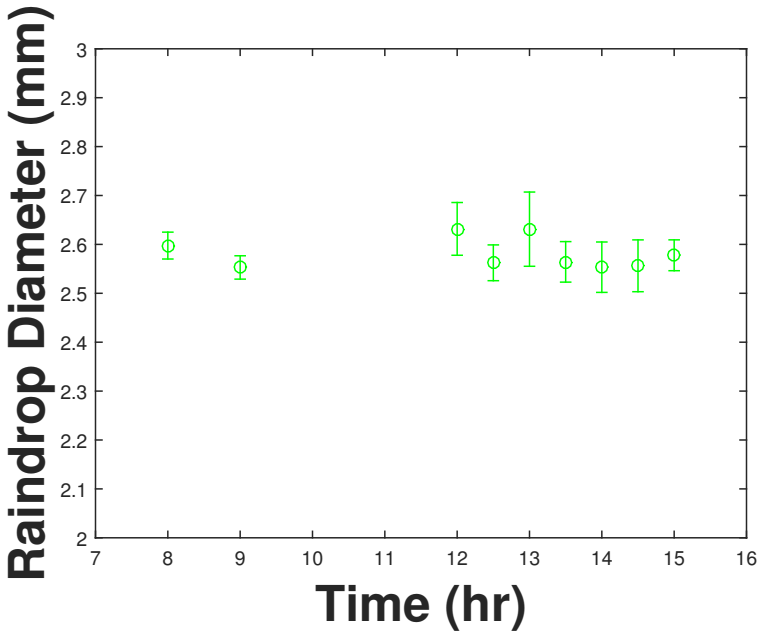

Figure 3.14: Raindrop diameter variation over 7 hours period

gauge long needles and a rain generator water height of 25 cm with the rain generator stationary was chosen for these experiments. The droplet measurement samples at each time contained 10 to 45 raindrop impacts. The average and the standard deviation of the raindrop diameters were calculated and the results are shown in Figure 3.14. The average raindrop diameters fluctuated between 2.55 to 2.65 mm during the seven hour period and the standard deviation in the measurement at any time was about ± 0.05 mm.

To investigate the raindrop diameter and impact velocity variation due to rain generator motion, raindrop impact measurements were conducted using 22 gauge short needles with a 13 cm of water height inside the rain tank when the rain generator was stationary and moving in both circular and oval motions at the 4.8-meter height. The average and the standard deviation of the raindrop diameters are

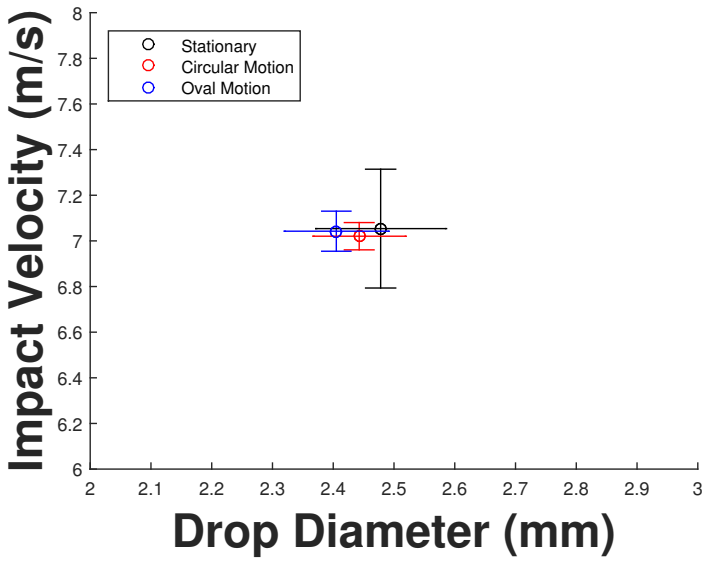

Figure 3.15: Raindrop variation due to rain generator motion

plotted in Figure 3.15 as black (stationary rain generator), red (circular motion), and blue (oval motion) open circles and error bars, respectively. The raindrop diameters varied from 2.3 to 2.6 mm and the average values varied from about 2.40 to 2.48. The average raindrop diameters were smaller when rain generator was moving but the difference was minor (less than 0.1 mm). For the three cases, the horizontal velocities of the raindrops at impact were close to zero and the average velocities at impact were almost the same. The stationary case had the biggest raindrop diameter variation, perhaps because the raindrops were generated from just two needles and the raindrops produced had two sizes with fairly large difference between them. This may also have lead to the stationary case having the largest variation of impact velocities.

As mentioned before, the average impact velocities of the raindrops ranged from 3.8 m/s to 7 m/s as the rain generator was positioned at 4 different heights.

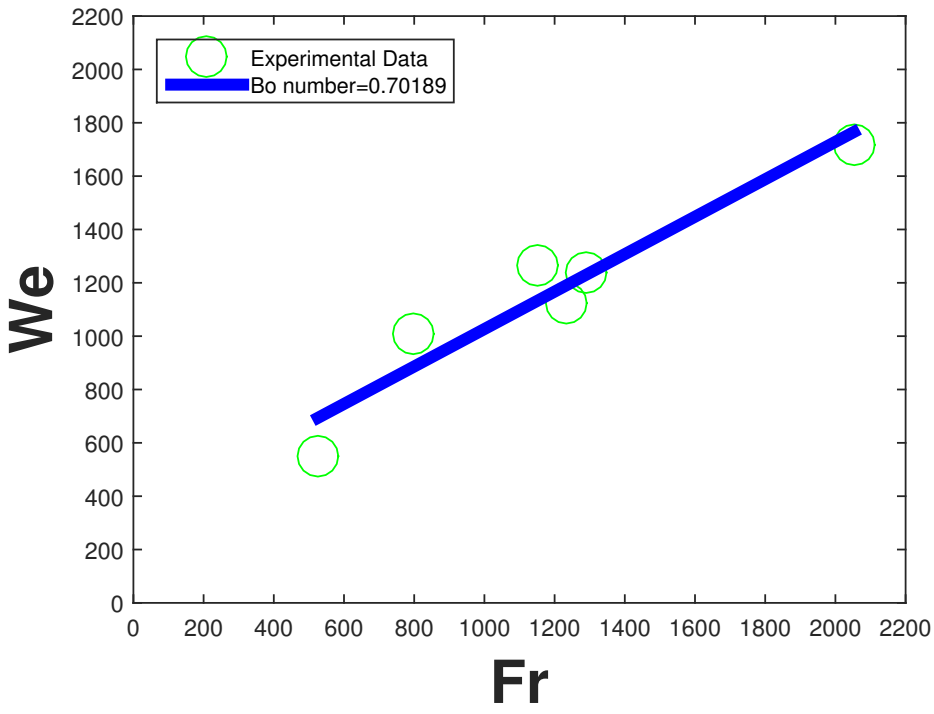

Figure 3.16: Non-dimentional raindrop impact condition

The drop impact Froude and Weber numbers were calculated using the average raindrop diameter and impact velocity. The resulting Froude numbers were between 500 and 1900 and the Weber numbers were between 500 and 2000. As shown in Figure 3.16, the Bond number was still consistent and small (0.71) but slightly less than the single drop cases due to the smaller diameter of the raindrops.

The maximum stalk heights in the rain fields were measured by nearly the same method, see Figure 3.17, as in the drop impact experiment. The mean water level measured without rain was used as the base level for all stalks. As mentioned in Section 2.3.3, this mean water level should be the same as the mean water level during the rain because the round tank was supplying water directly into the target pool through a garden hose to make the water overflow nearly the same as during

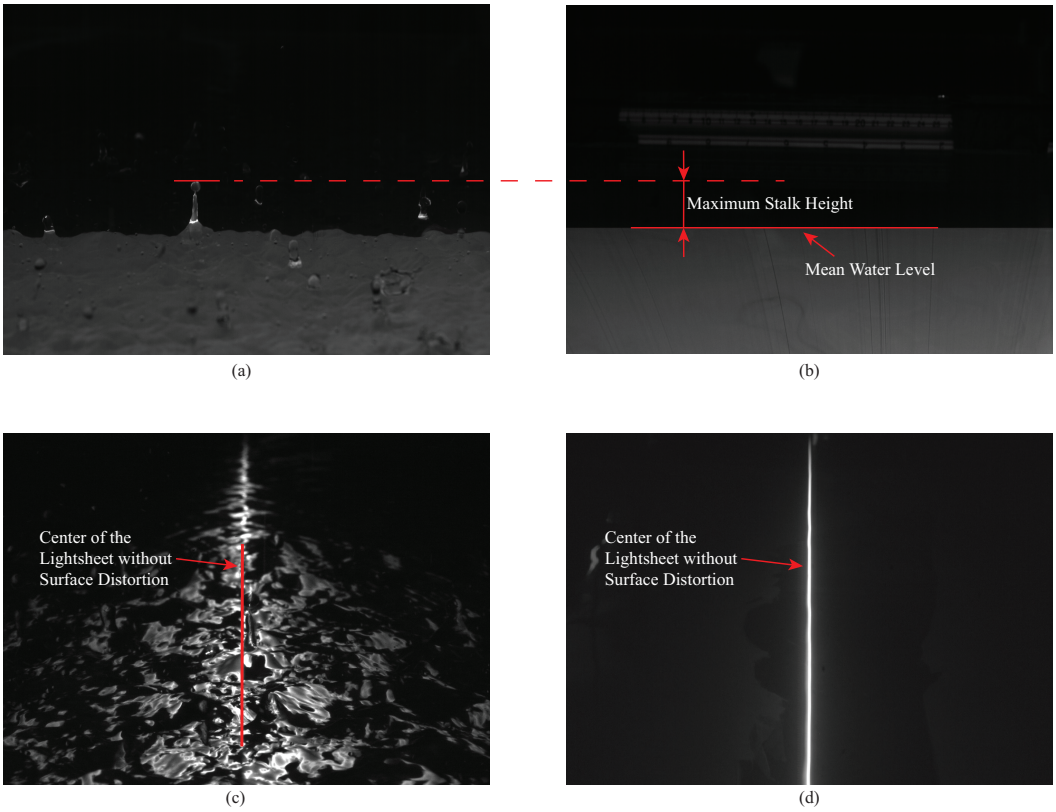

Figure 3.17: Measure the maximum stalk height in a rain field. (a) The maximum height a stalk can reach measured during experiment. (b) Mean water level measured during calibration. (c) Location of the measured stalk. (d) Location of the light sheet during calibration.

the rain experiment. Also, the stalk location relative to the center plane of the light sheet was measured with the end-view images; see Figures 3.17(c) and (d). Only stalks that were at least partially within the light sheet were collected for the data set.

The heights of about 1000 stalks were collected for each rain condition and statistical analyses were performed with each data set. Figures 3.18 (a) through (c) show the stalk height distributions of four rain cases. For the conditions correspond-

ing to subplots (a), (b), and (c) the impact velocities were nearly the same (5.59, 5.61 and 5.66 m/s, respectively), but the rain intensities were different (85, 130, and 300 mm/hr, respectively). The conditions corresponding to subplots (b) and (d) have the same rain intensity (130 mm/hr) but different impact velocities (5.61 and 6.83 m/s, respectively). The range of stalk heights is about 2 mm to 400 mm in all four cases. This wide range of the stalk height distributions, which consistently appears for all rain conditions, indicates that this is a complex problem. If we consider a drop impact for which the vertical velocity of the water surface in the vicinity of the drop impact has the same magnitude and opposite direction as the drop velocity, then the relative impact velocity between the droplet and water surface will be twice as big as the drop velocity. Thus, the single drop impact-induced stalk height under this assumption could be as high as the tallest measured stalk in a rain field. The dotted vertical blue lines indicate the average stalk height for each rain experiment. The dotted vertical red lines indicate the corresponding average stalk heights from the single drop experiments. These values are obtained using the straight line fit to the single drop impact data (Figure 3.6) in the range $1,000 \leq Fr \leq 1300$ and the Froude numbers from the rain experiments, $Fr = 1,235$, 1,206, and 1,150 corresponding the subplots (a), (b) and (c), respectively, in Figure 3.18. For case (d), the single drop impact-induced stalk height is not predictable as mentioned before. In is found that as the rain intensity increases, the raindrop impact-induced average stalk height decreases while the corresponding stalk height from the single drop impact experiments remains nearly the same. For the cases with the same rain intensity comparison but different drop impact velocities (subplots (b) and (d))

the average stalk height changes only slightly from 15.05 mm at the lower velocity (subplot (b) to 14.5 mm at the higher velocity (subplot (d)). This latter trend with impact velocity is opposite to the single drop results.

To take a close look at what happened in the rain field, a sequence of images for the lowest raindrop impact velocity 3.8 m/s were shown in Figure 3.19. The images show two raindrops impacting the water surface with similar impact conditions. However, the first impact (marked by the red arrows) results in the formation of a stalk while the second impact (marked by the white arrow) results in the formation of a bubble. This difference might be due to the local turbulence-induced surface velocity of slope fluctuations. The crown enclosure phenomenon which only happens for Froude number greater than 1800 in single drop experiments, can happen at much lower Froude numbers (average $Fr = 526$ in the present case) in a rain field.

To further investigate the effect of rain intensity on the stalk height distributions, the three cases with different rain intensity and similar impact velocity (approximately 5.7 m/s) plotted in figure 3.18(a), (b) and (c) were further analyzed. To this end, the stalk heights for each case were nondimensionalized by their average height and the three distributions were were placed on a single log-log plot, see Figure 3.20. Straight lines were fit to each distribution in the low ($H^* < 0.5$) and high ($H^* > 15$) ranges of the graph and plotted as solid lines. The distributions in these regions vary significantly with the rain condition; as the rain intensity decreases, the slope of the solid lights increase. In the band of H^* between the straight line fits, the distributions are nearly independent of rain intensity. If the rain intensity (number of raindrop) is further reduced to the same as a single drop,

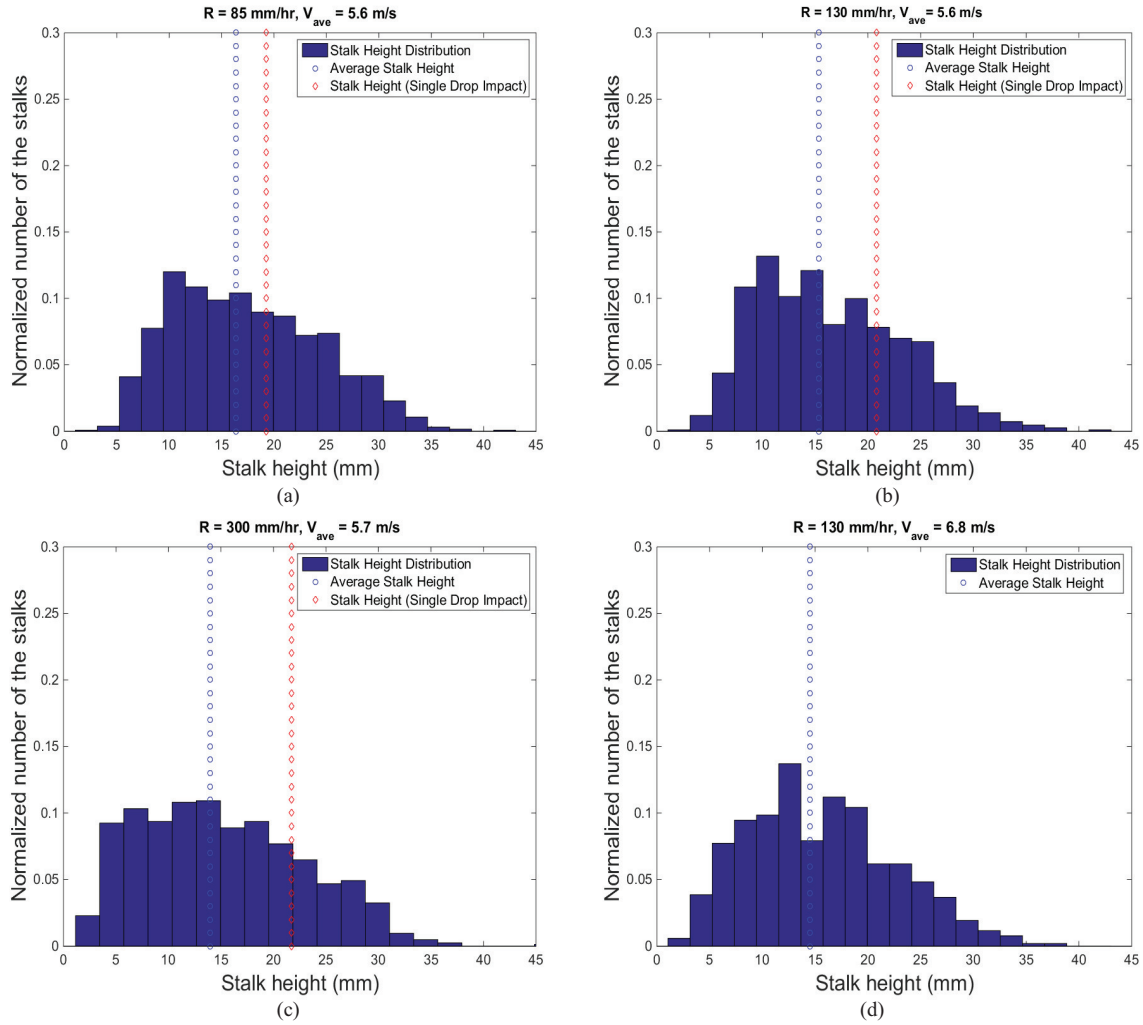

Figure 3.18: Stalk height distributions. (a) Rain intensity is 85 mm/hr with 5.59 m/s raindrop velocity at impact. (b) Rain intensity is 130 mm/hr with 5.61 m/s raindrop velocity at impact. (c) Rain intensity is 300 mm/hr with 5.66 m/s raindrop velocity at impact. (d) Rain intensity is 130 mm/hr with 6.83 m/s raindrop velocity at impact. See Table 3.2 for additional characteristics of these rain conditions.

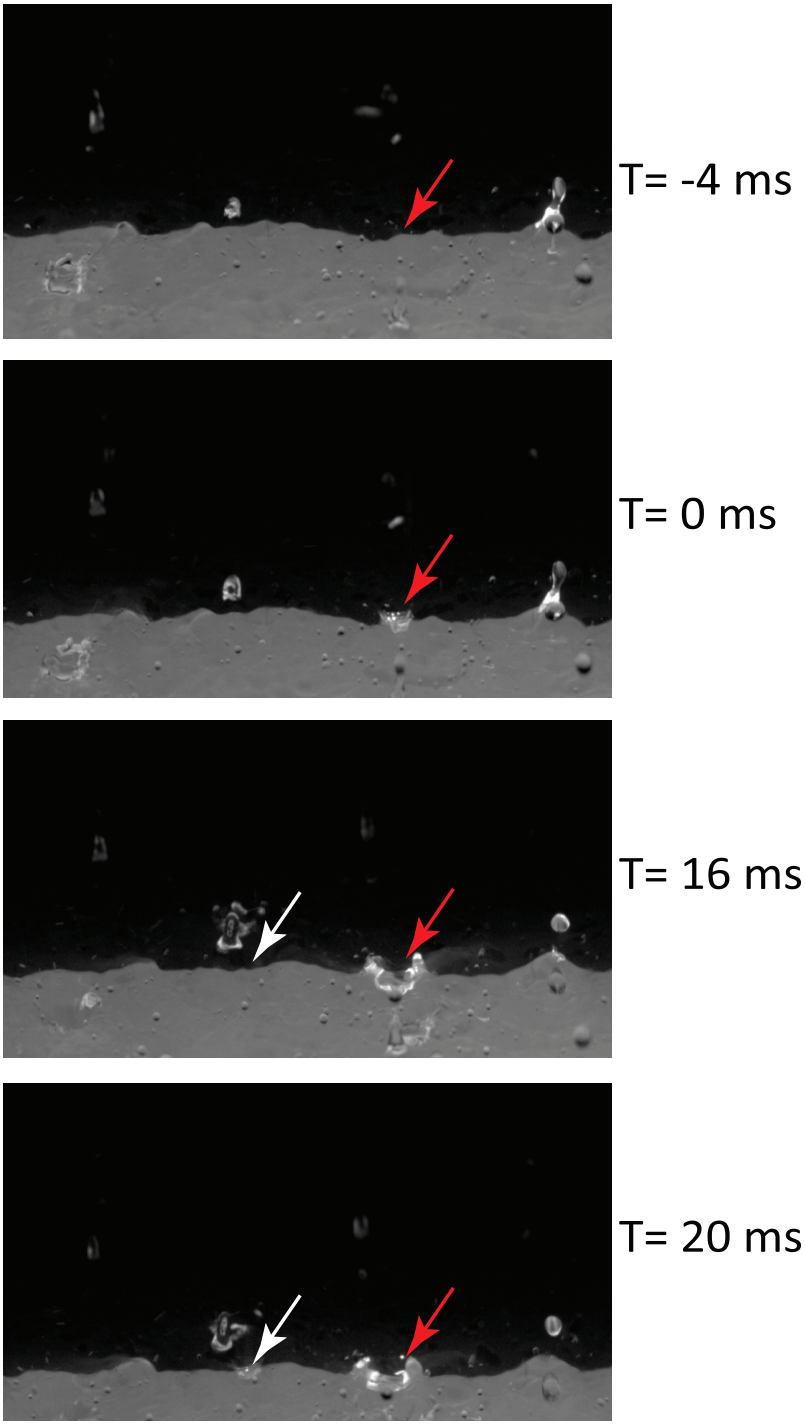

Figure 3.19: An LIF image sequence from the rain condition with a rain intensity of 130 mm/hr and a raindrop impact velocity of 3.78 m/s. The sequence begins at the moment when a droplet impacts the water surface at the location marked by the red arrows. In subsequent images, a stalk forms at this location. The white arrows marks the location of a second drop impact. At this location, an irregular bubble forms instead of a stalk.

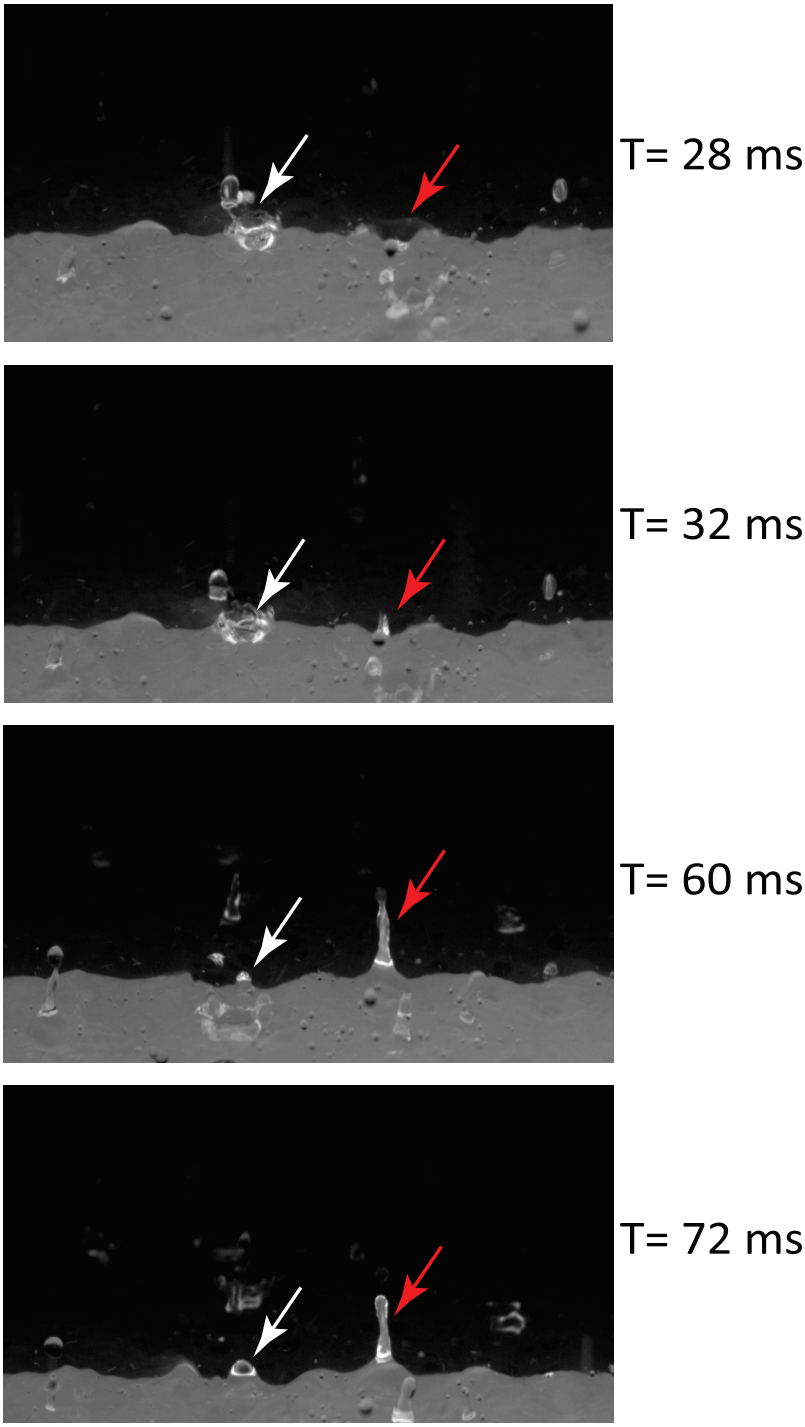

Figure 3.19: Photographic sequences (cont.)

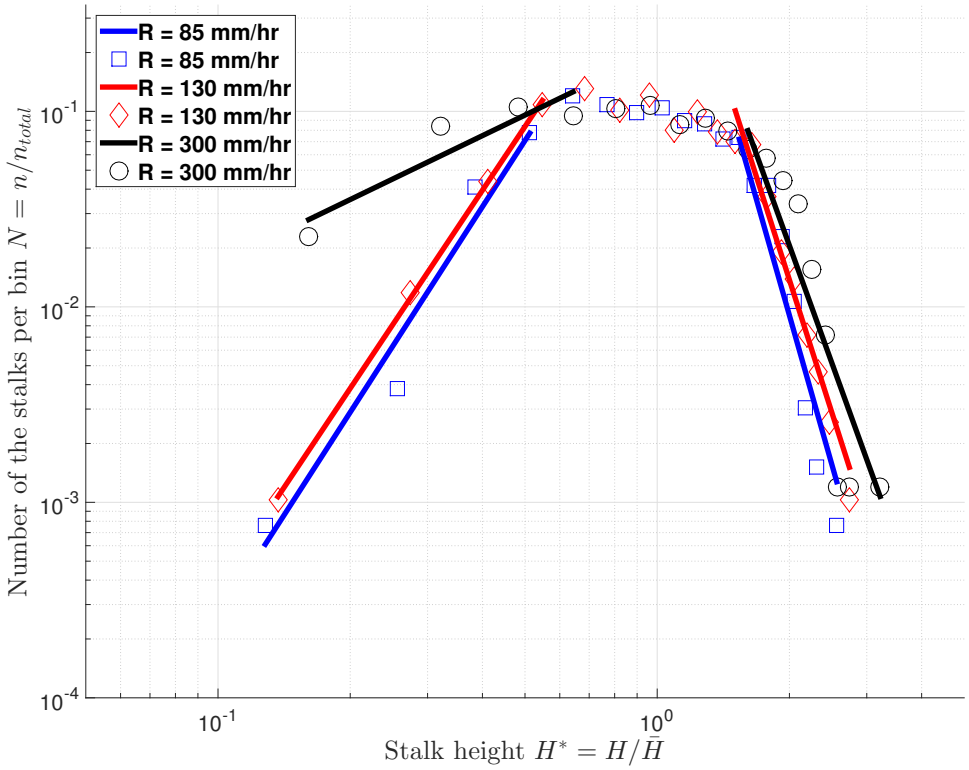

Figure 3.20: Non-dimensional stalk height distributions. All three conditions have nearly the same drop diameters (about 2.7 mm) and impact velocities (about 5.7 m/s). Further details can be found in Table 3.2.

the two solid line will collapsed together to form a vertical line. The thickness of the vertical line will indicated the standard deviation of a single drop impact-induced stalk heights.

To investigate the effect of impact velocity on the stalk height distribution, three cases with a rain intensity of 130 mm/hr and different impact velocities (3.8, 5.6 and 6.8 m/s) are plotted in Figure 3.21. The data points below $H^* = 0.7$ and above $H^* = 15$, especially on the upper range, appeared to collapse to a single

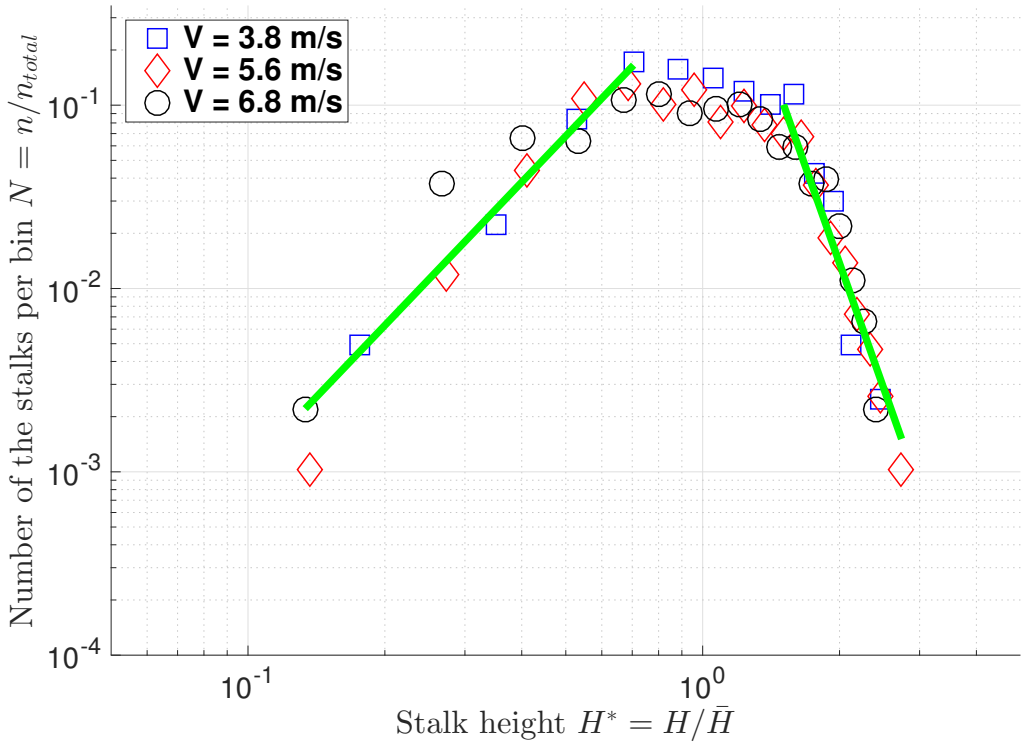

Figure 3.21: Non-dimensional stalk height distribution. Rain intensity is about 130 mm/hr rain intensities with three different raindrop velocities at impact. Further details can be found in Table 3.2.

straight line. Thus, linear regression fits were performed and plotted as the green solid lines. In the band between the two linear regions, there is a slight increase in the number of stalks with decreasing impact velocity; however, generally speaking the distributions only vary slightly in the range of impact velocities in these experiments.

To compare the raindrop stalk height data with the data from the single drop impact experiment, the average and standard deviations of H^* were calculated for each condition and plotted versus Froude number, along with the single drop data, in Figure 3.22. The green circles are the maximum stalk heights from single drop

impact experiment and the black diamonds are the rain experiments. In any small band of Fr, the average maximum stalk heights in the rain cases were always substantially less than in the single drop cases. For Froude numbers less than 1000, the upper end of the standard deviation range is above the single drop H^* average and standard deviation range. For Froude numbers between 1000 and 1800, the upper end of the H^* standard deviation range is close to but usually below the H^* data for the single drop case. -induced stalks are about the same as the stalk induced by a single drop impact. For Froude numbers greater than 1800, the upper end of the standard deviation range of H^* values for the rain-induced stalks are less than the average stalk height in the single impact experiments.

3.2.2 Surface Waves

As mentioned in Chapter 2, a water surface profile in the plane of the light sheet can be extracted from each image of the LIF movie. For several rain conditions, a continuous sequence of 250 profiles were plotted together and each profile was shifted vertically from the previous one by 1 mm to generate plots such as the one in Figure 3.23. The horizontal axis in the plot is horizontal distance along the center-plane of the rain field. The vertical axis is the water surface height above the mean water level. Based the camera frame rate, the time interval between the consecutive profiles is 1/250 s. The big empty white spots indicate the rapid change of the water surface that are usually associated with the raindrop impact-induced crowns. There are more than 50 stalks in Figure 3.23, but many of them were from

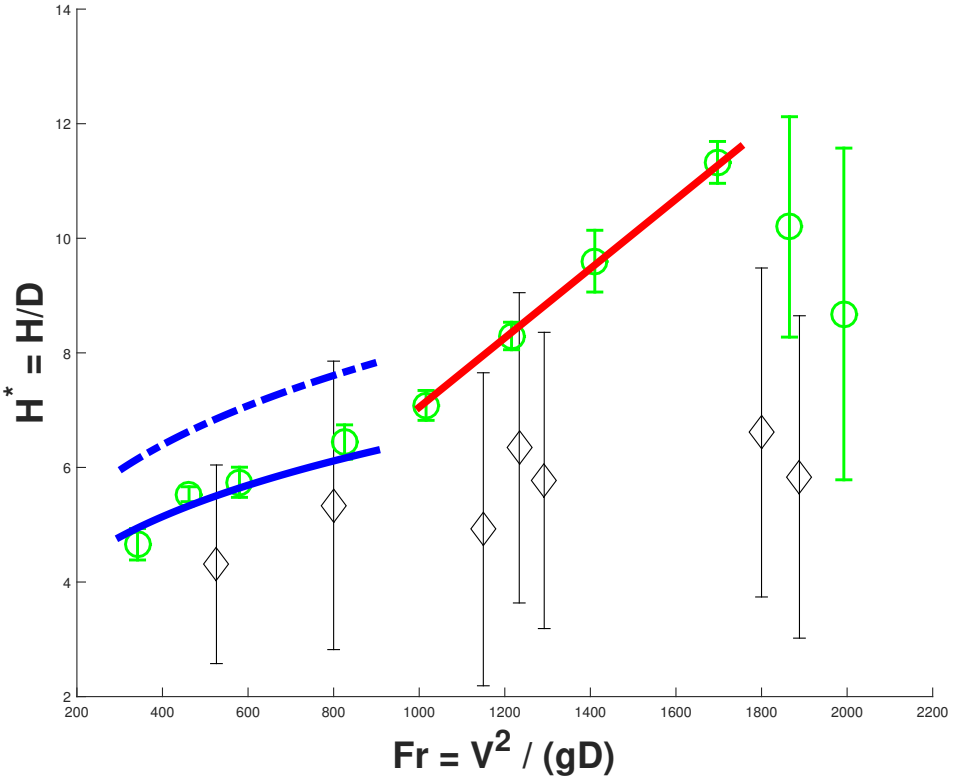

Figure 3.22: Average stalk heights and the corresponding standard deviations. Green dots are the data from single drop experiment and black diamonds represent rain experiments

raindrops that hit the target pool in front of the light sheet and induced stalks that rose up to block the camera's view of the light sheet and appeared as if they were part of the profile in the light sheet plane. Only a few of stalks (less than 10) were induced by the raindrops impacts near the light sheet indicated by the formation of crowns (white spot).

Although the surface in a rain field is chaotic, the surface waves propagating in both the (left and right) directions away from the impact location can be clearly observed. Due to the chaotic nature of the water surface inside a rain field, many other features like crowns and stalks are present and blocking the surface waves. Because of these complex profiles, the surface waves could not be analyzed using numerical methods such as cross correlation. The velocities of those surface waves were approximated by tracking their crests from profile to profile as indicated by the red arrows.

On the other hand, the surface profiles outside the rain field contain mostly the surface waves as show in Figure 3.24. Occasionally, small drifting droplets carried away by the surface waves were observed. There appear to be two distinct wavelengths in the record and both move at nearly the same speed. To be consistent, with the above-described wave speed measurements inside the rain field, the the wave phase speeds outside the rain field were also approximated by the same method of tracing crests. The velocity distributions of surface waves inside and outside of a rain field are plot in Figure 3.25. The wave velocities inside the rain field have greater variation. Surface waves outside of the rain field (further away from the impact location) propagate faster.

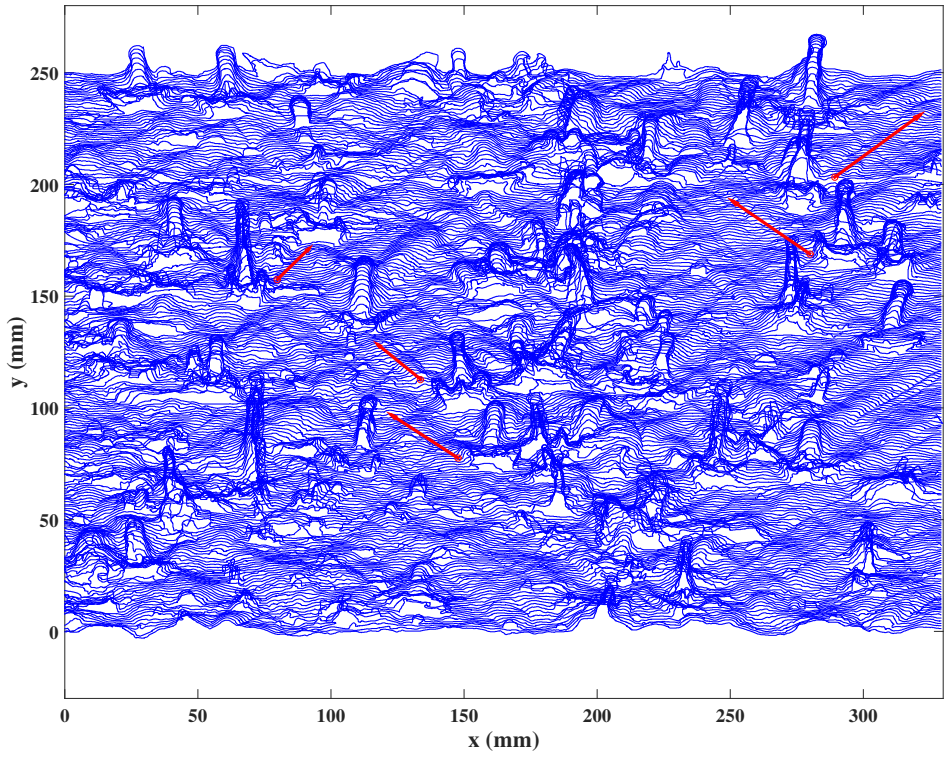

Figure 3.23: A water surface profile history at the intersection of the light sheet and the water surface within a rain field.

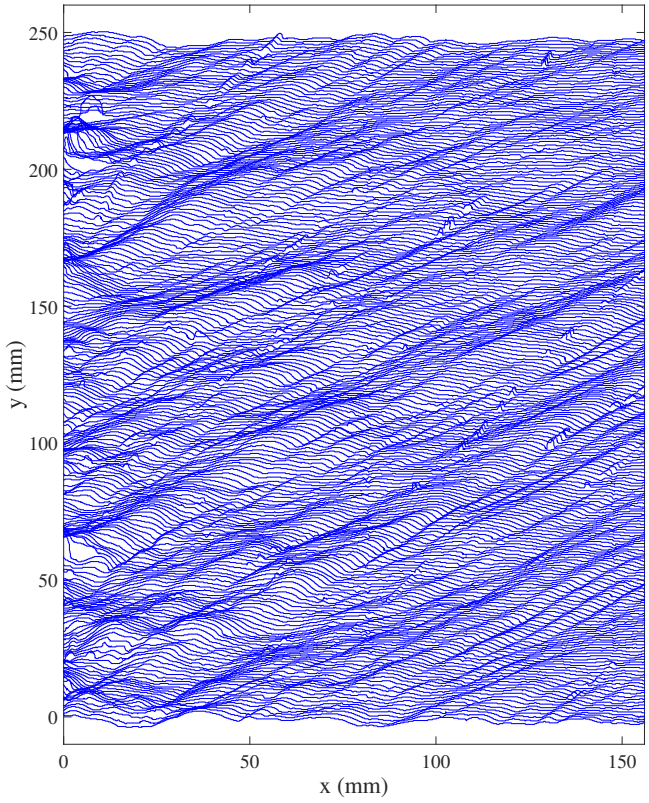

Figure 3.24: A water surface profile history of the surface wave outside the rain field at the intersection of the light sheet and the water surface.

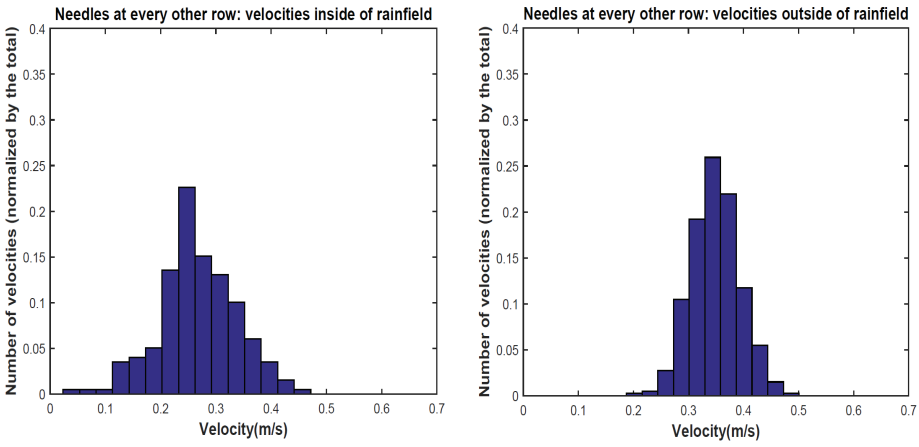

Figure 3.25: Surface wave velocity distribution

In order to quantitatively study the propagation of surface waves outside of a rain field, a cross correlation function R was applied to profiles, where

$$R(\Delta x, \Delta t) = \frac{\sum(Z_1(x,t) - \bar{Z}_1)(Z_2(x+\Delta x, t+\Delta t) - \bar{Z}_2)}{\sqrt{\sum(Z_1(x,t) - \bar{Z}_1)^2}\sqrt{\sum(Z_2(x+\Delta x, t+\Delta t) - \bar{Z}_2)^2)}}. \tag{3.5}$$

In this equation, Z_1 and Z_2 are the two correlated profiles, x is the horizontal coordinate along the center-plane of a rain field at free surface and t is time determined by the frame rate. Δx and Δt are the spatial and temporal shift between correlated profiles. The cross correlation was applied for profiles outside the rain with different rain intensities and nearly the same impact velocities. The resulting correlation maps average over a region next to the rain field are shown in Figure 3.26. Figure 3.26 (a) is the result from the lower rain intensity (130 mm/hr). The resulting period is T=0.14s and the average surface wave velocity is 0.354 m/s. When the rain intensity is increased more than twice (300 mm/hr), the period and average surface wave velocity were not change much (T=0.136 s and V_{ave} = 0.357 m/s).

3.3 Subsurface Flow Field

Subsurface flow field were measured at two different rain generator heights and with two different rain intensities. The original goal was to find the correlation between the subsurface turbulence and the raindrops impact-induced surface features. Thus, a geometric mask, like the one shown in Figure 3.27 (a), was applied around drop impact locations for images 8 ms and 4 ms before raindrop impact to

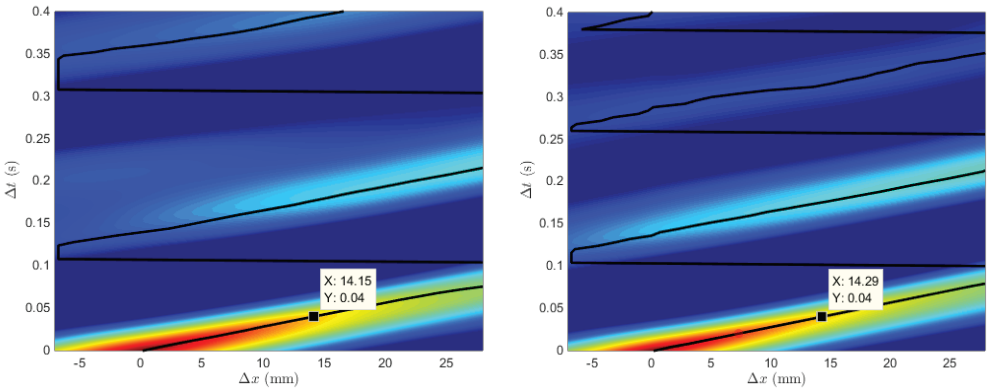

Figure 3.26: Cross correlation result of surface profiles outside the rain field. (a) Rain intensity R = 130 mm/hr. (b) Rain intensity R = 300 mm/hr.

measure the subsurface flow field (Figure 3.27 (b)). Then, the resulting maximum stalk height was also collected from the simultaneous LIF measurement. About 100 of those velocities fields and the resulting maximum stalk height were collected. The averaged vertical velocity showed a correlation with the averaged maximum stalk height as shown in Figure 3.28. If the vertical velocity of the flow field was downward when a raindrop impacted the water surface, the crater would be deeper and the resulting stalk would be higher. However, the standard deviation was big and may have been due to the surface slope variation. The surface slope was not measured because the LIF is a 2D measurement.

It is also important to look the average RMS turbulent velocities ($\overline{U}_{RMS}$,$\overline{V}_{RMS}$,$\overline{W}_{RMS}$). The RMS velocities of each velocity field (V) were calculated using the following equation:

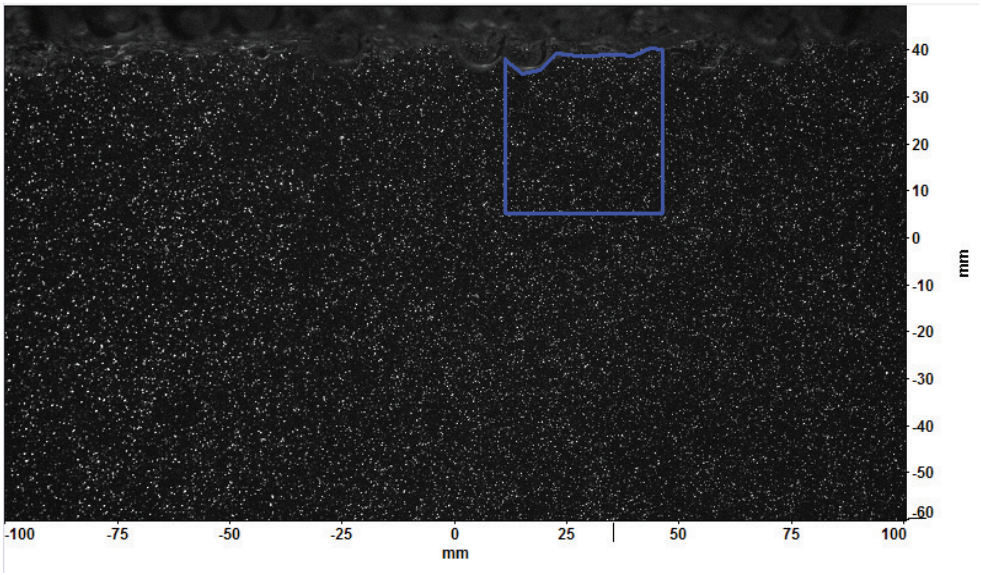

(a)

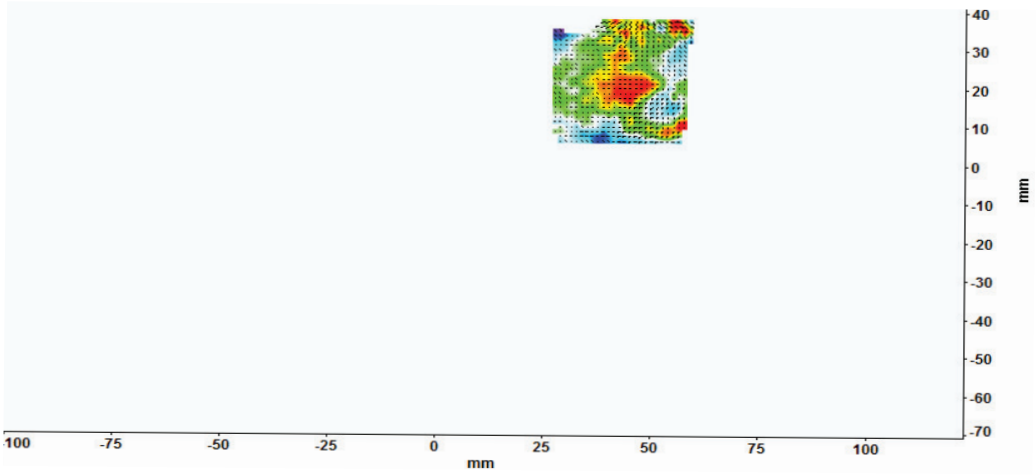

(b)

Figure 3.27: Subsurface flow field at impact location. (a) A geometric mask was apply before raindrop impact at impact location (b) Calculated subsurface flow field 4 ms before a raindrop impact

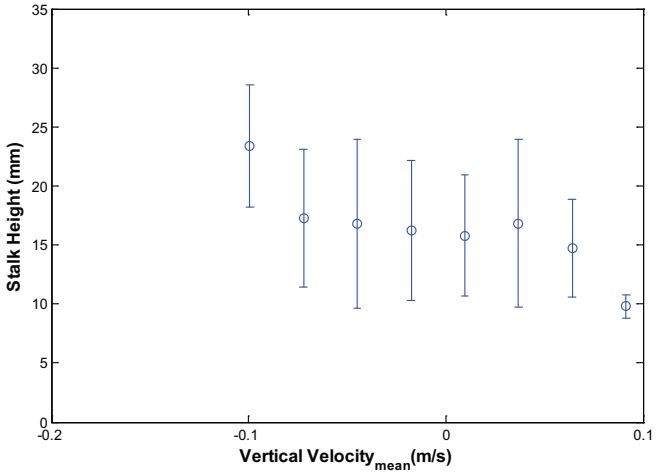

Figure 3.28: Stalk height variation and the corresponding averaged vertical velocity.

$$V_{RMS} = (\frac{1}{n}\sum(V_i - V_{mean})^2)^{1/2}. \tag{3.6}$$

where,

$$V_{mean} = \frac{1}{n}\sum(V_i). \tag{3.7}$$

Then, V_{RMS} from 4500 velocity fields (18 s measurement time) were averaged to get the average RMS turbulent velocities ($\overline{U}_{RMS}$,$\overline{V}_{RMS}$,$\overline{W}_{RMS}$). Due to the depth of rain-induced craters, the subsurface flow field were measured about 10 mm (5.7 m/s impact) and 18 mm (7 m/s impact) below the mean water level. Figure 3.29 shows the RMS velocity for the same rain intensity with different raindrop impact velocities. At the same depth (-18 mm), the RMS velocities were greater with higher raindrop velocity at impact . RMS velocities of both cases experienced a sudden drop. For 5.7 m/s raindrop impact velocity, the velocity is suddenly decrease around 12 mm below the mean water level while the higher impact velocity case the

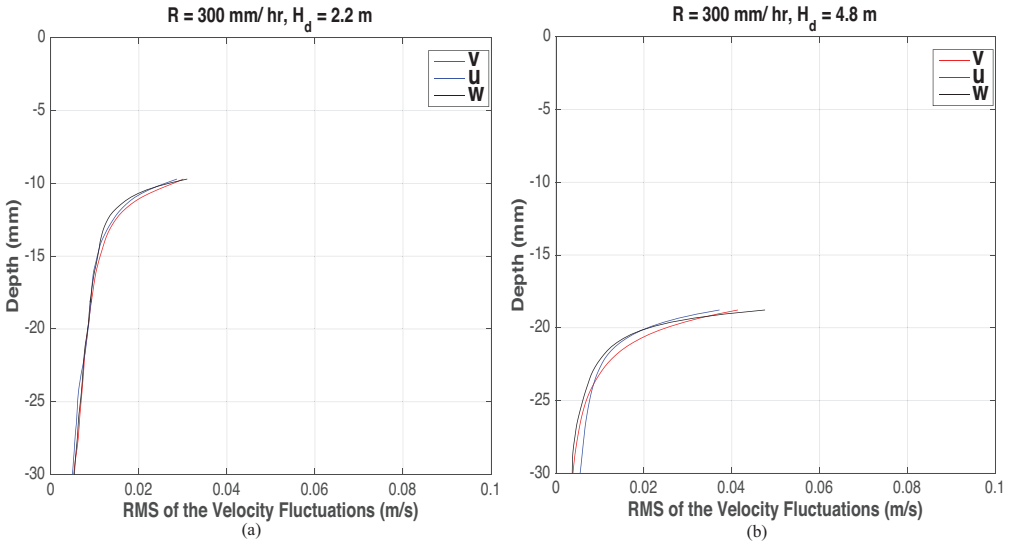

Figure 3.29: Velocity RMS vs. Depth (mean water level is considered depth = 0 mm) of rain intensity 300 mm/hr. (a) 5.7 m/s raindrop impact velocity. (b) 7 m/s raindrop impact velocity.

suddenly decrease happens at much lower depth (around 22 mm below the mean water level). The rain intensity did not have significant impact on the RMS velocity, see Figure 3.30. When rain intensity increased more than twice, all three velocities (U, V, and W) had small differences (on the order of 0.001 m/s) at the at a given depth. RMS velocities measured in the present study have greater RMS velocities than those previously reported by Lange et al. [29], and Beya et al. [3], because the measurement was conducted closer to the water surface.

3.4 Radar Measurement Results

The radar backscattering power (intensity) from the raindrops, surface waves, and stalk were measured separately to study the effect of each feature on radar

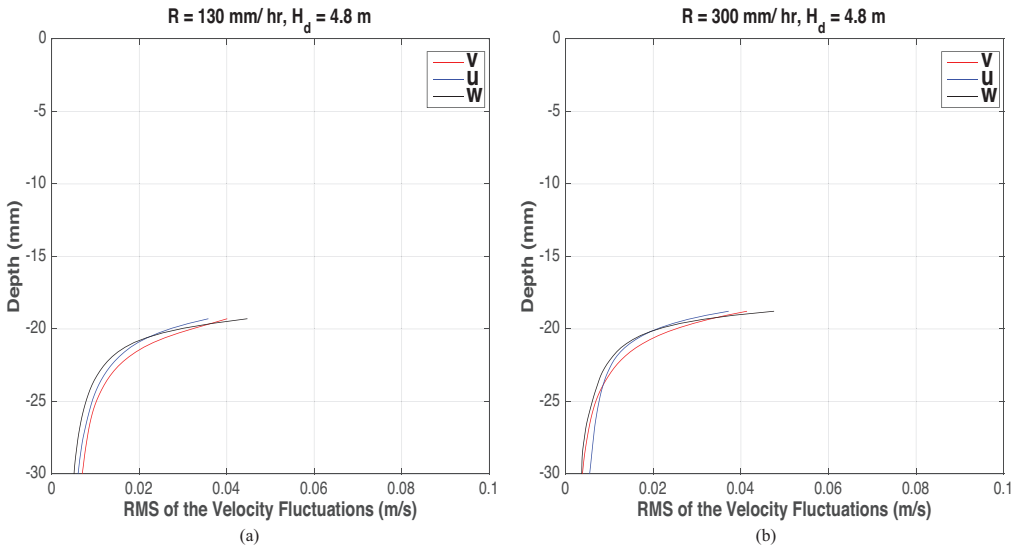

Figure 3.30: Velocity RMS vs. Depth (mean water level is considered depth = 0 mm) with raindrop velocity 7 m/s at impact. (a) Rain intensity R = 130 mm/hr. (b) Rain intensity R = 300 mm/hr.

backscattering. For raindrop cases, the antennas was placed horizontally ($\theta = 90°$) and the water in the target pool was lowered such that the secondary droplet did not interfere with the radar signals. For surface wave cases, the half field concentrated needle arrangement was used such that there are only surface waves in the first half of the target pool. Thus, the backscattering power from the front half of target pool is correlated with the surface waves.

Figure 3.31 is a image for raindrop falling from 4.8 m above (7 m/s velocity at impact) and it shows that the secondary droplets formed a thick layer (up to 14 cm) above the water surface. The raindrops were constantly falling down and appeared to be short vertical bars because the velocity of the raindrop was high and the exposure time was not sufficiently short to capture them.

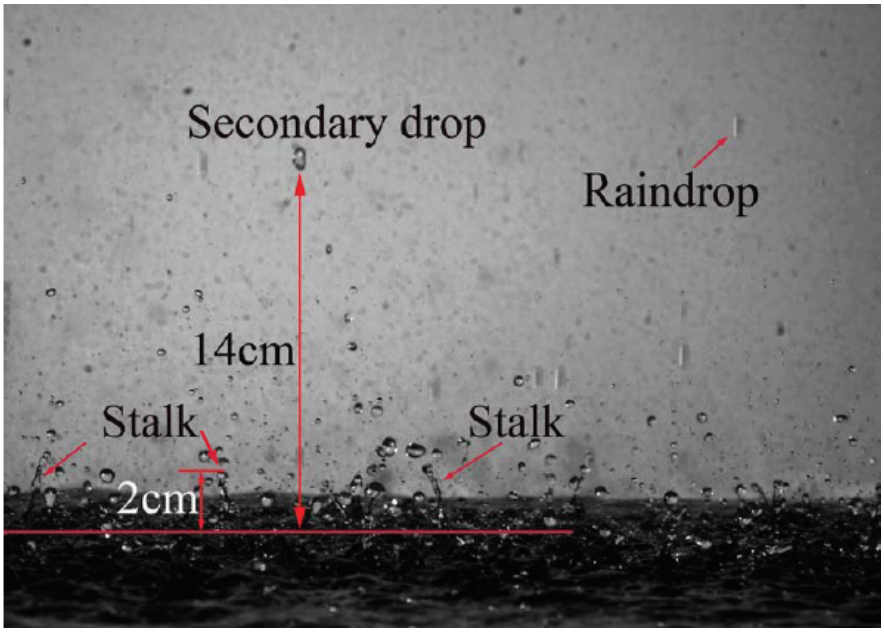

Figure 3.31: Rain field of a 300 mm/hr rain with 7 m/s raindrop velocity at impact

Figure 3.32 shows the variances of all four backscattering signals measured at five different incident angles. Five measurements were taken at each angle with a constant rain intensity, which was around 130 mm/hr and 5.7 m/s raindrop velocity at impact. As can be seen from the figure, the variance of the radar signal decreases with increasing incident angle with an exception at 55°. The magnitude of the VV radar signal is significantly stronger than that of other signals.

As mentioned in Chapter 1, Sobieski el al. [61] found significant differences of geometrical and backscattering characteristics of surface features for raindrops impact at terminal and non-terminal (50 % - 60 %) velocities. However, no significant difference is found in the present study for raindrops impact at 90 % and 72% terminal velocities with an exception of HV signals, see Figure 3.33. This is consistent with the stalk height distribution only vary a little for increasing impact

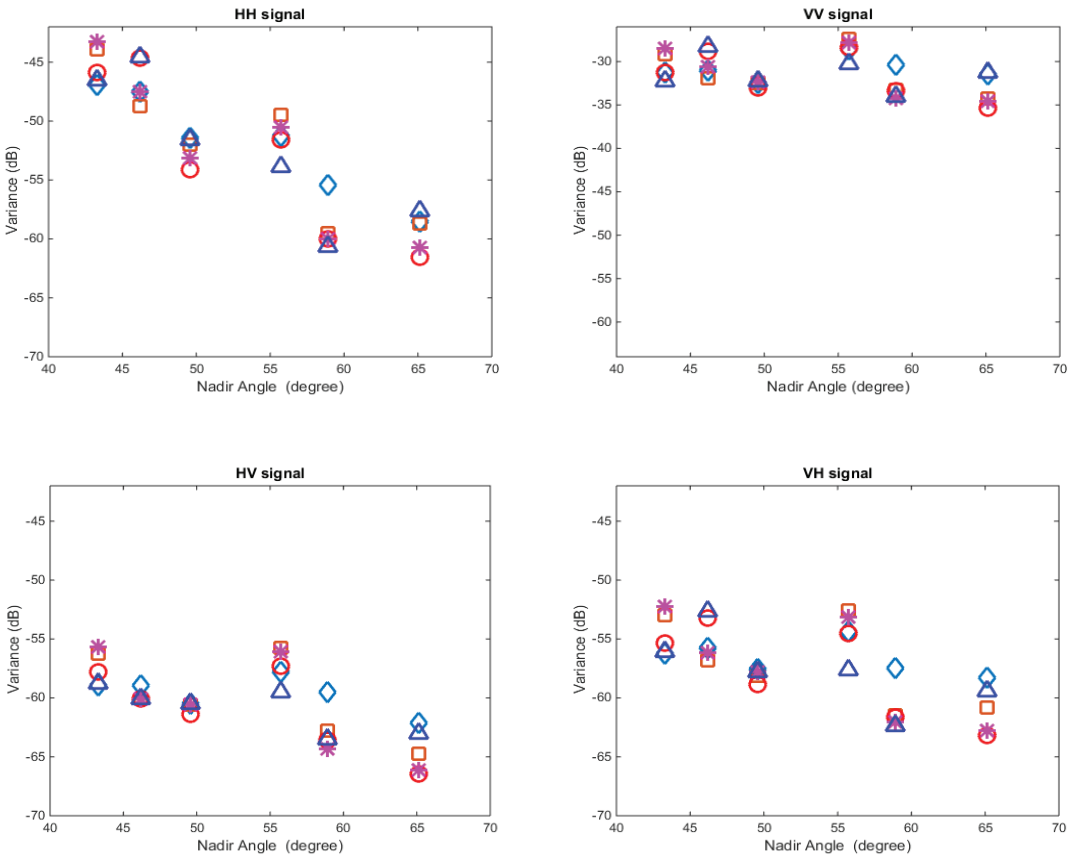

Figure 3.32: All four signals of the radar backscattering of water surface inside the rain field. Each plotting symbol represents one experimental run. There were 5 repeated run performed at each angle.

velocity.

Figure 3.34 shows the radar backscattering due to the raindrops, the surface waves in front of the rain field and the water surface within the rain field. The radar backscattering due to surface waves in front of the rain field was measured at two different incident angles with 300 mm/hr rain intensity and 7 m/s raindrop velocity at impact. As can be seen from the figure, the radar backscattering power of a water surface within a rain field was the strongest one except the HV signals. The power of HV signals of a rain field had the similar strength as the surface waves at 45°.

Since a large amount of the secondary droplets and raindrops were consistent present in a rain field as well as other surface feature such as surface waves, and crater and crowns, it is difficult to study the effects of impact-induced stalks to radar backscattering alone. Thus, a PVC board with an array of nails were used to mimic the stalks to investigate the backscattering power due to stalks only, see Figure 3.35. These nails were arranged to have the same full field concentered setting as the needles attached to the bottom of rain tank. Then, the PVC board was completed submerged into the water, only allowing top 2 cm portion of the nails to be above the water surface.

Figure 3.36 (a) shows the radar signal obtained from the raindrop impact area ranging from 0.3 to 0.8 m. As can be seen from the figure, the radar signal in the rain field decays with increasing distance from the radar antennas, while the radar signal in from the array of the nail tips, which is shown in Figure 3.36 (b), has little variation with the distance less than 0.8 m away from the radar. The trend difference between these two signals in Figure 3.36 (a) and (b) might be due to

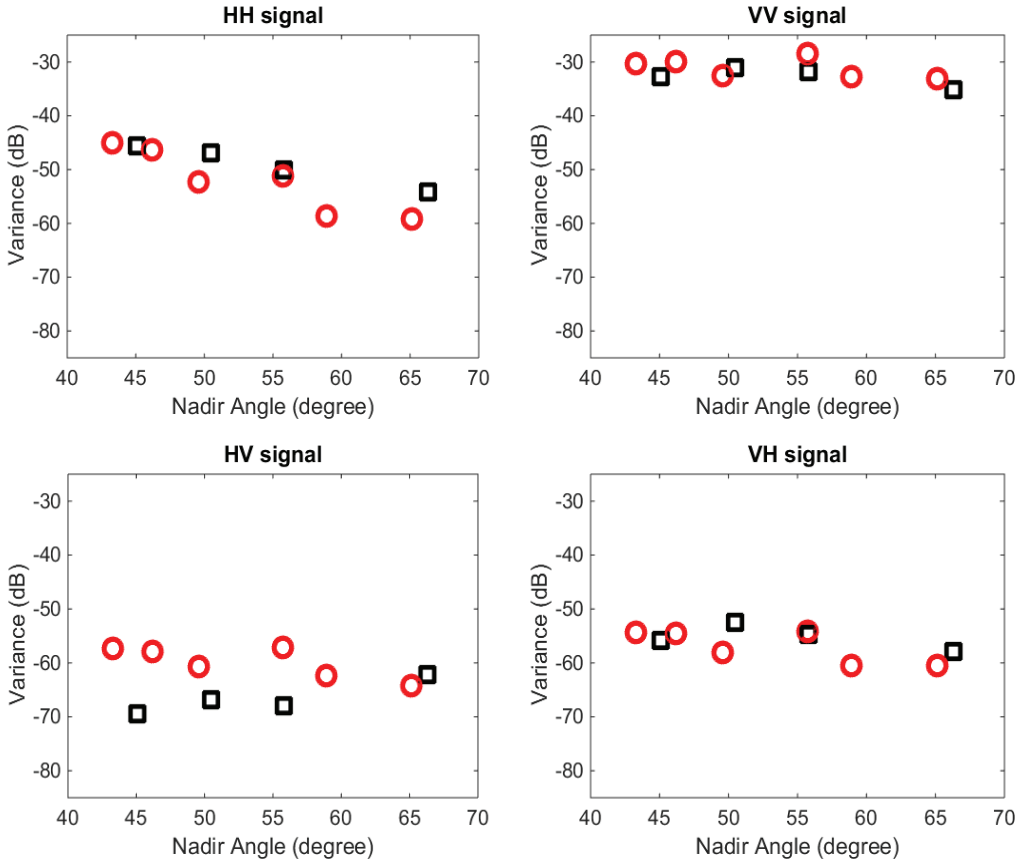

Figure 3.33: All four signals of the radar backscattering of water surface inside the rain field. Red circles are the average of five repeated runs of rain experiment with 72% terminal velocity (R = 300 mm/hr, H_d= 2.2 m, V_{ave}= 5.7 m/s). Black squares are the average of five repeated runs of rain experiment with 90% terminal velocity (R = 300 mm/hr, H_d= 4.8 m,V_{ave} = 7 m/s))

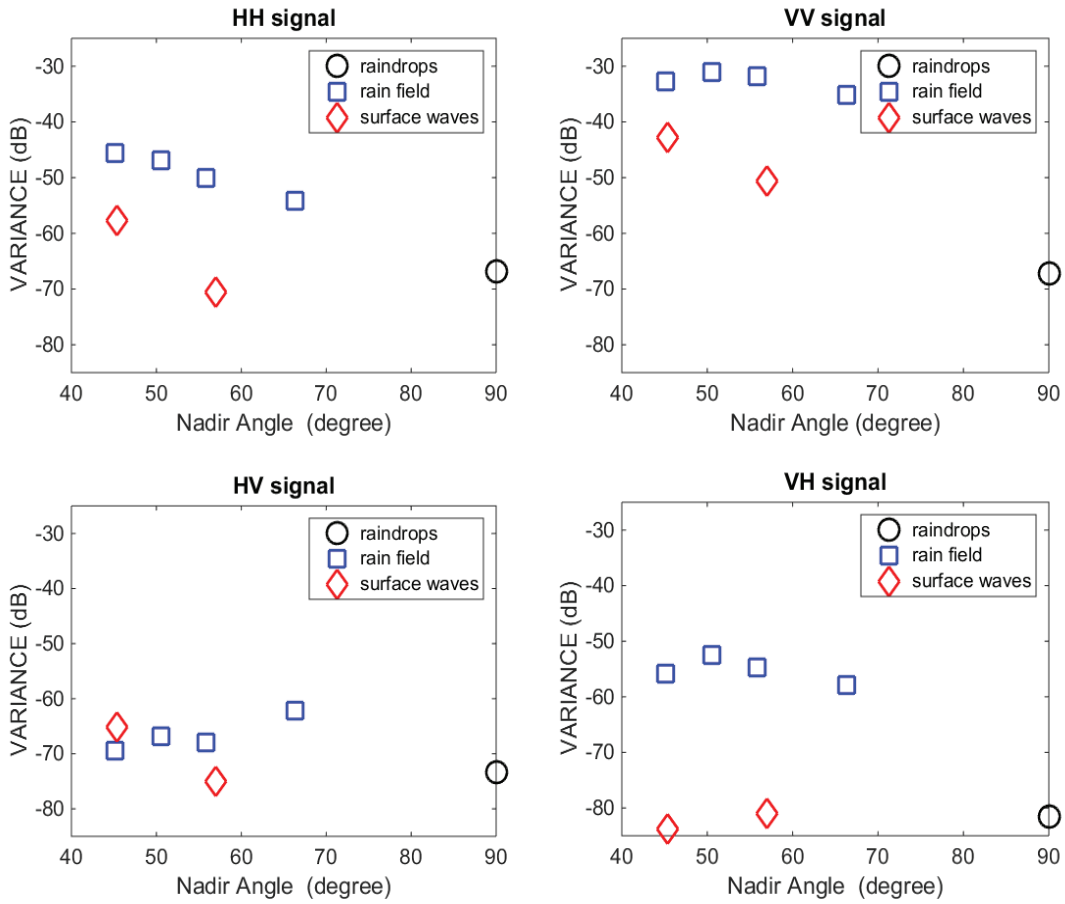

Figure 3.34: Radar backscattering of raindrops, surface waves and water surface inside the rain field. Each plotting symbol represents one experimental run. There were 10 repeated runs for measuring radar signals of surface waves (at two different angles), 5 repeated runs for measuring radar signals of the rain field (at four different angles), and 2 repeated runs for measuring radar signals of raindrops (antennas were horizontal and water inside the target pool was lowered) at each angle.

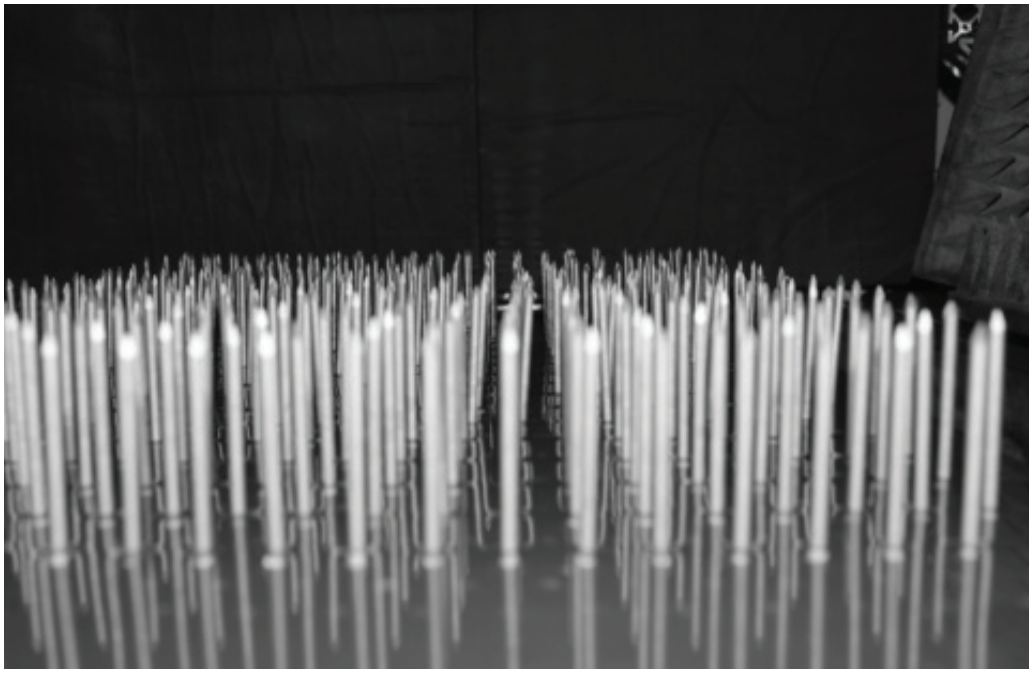

Figure 3.35: Array of nails used to represent stalks.

the presence of the raindrops and the layer of raindrop impact-induced secondary droplets. In addition, the radar signal obtained from the simulated rain falling on the nail tips (Figure 3.36 (c)) is similar to that shown in Figure 3.36 (a), indicating that the radar signal from the nail tips is significantly attenuated by the rain.

Figure 3.37 shows the variances of the radar backscattering signals measured at 57° incident angle with three different rain intensities. Each measurement was repeat for five times and the difference between run to run was small. As can be seen from the figure, the variances of all four signals increase with increasing rain intensity and the VV signal remains to be the strongest one. The HH signals are stronger than VH and HV signals but they have similar trend.

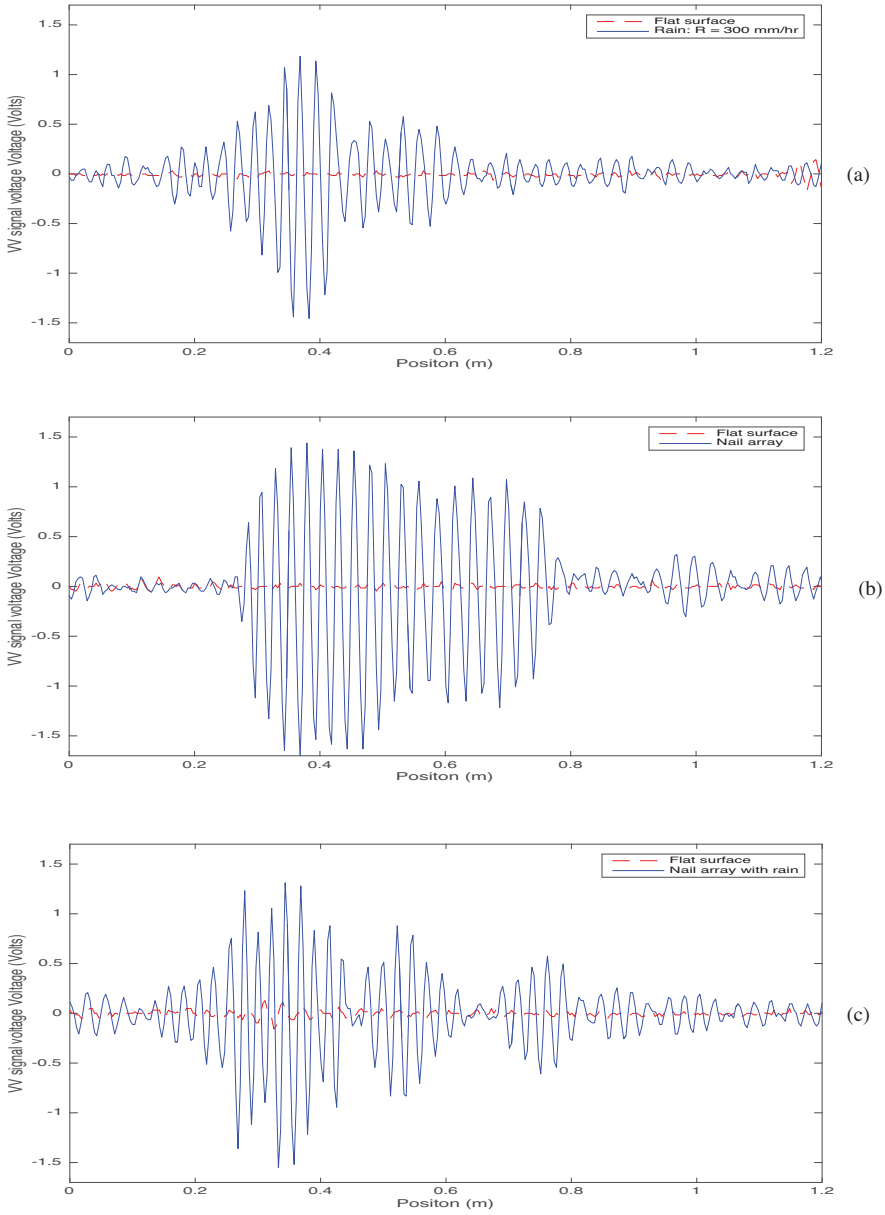

Figure 3.36: Radar VV signals versus the distance from the antennas. (a) Signal received during raining. (b) Signal received by using an array of nails. (c) Signal received when raindrops impacting onto a water surface with the presence of an array of nails.

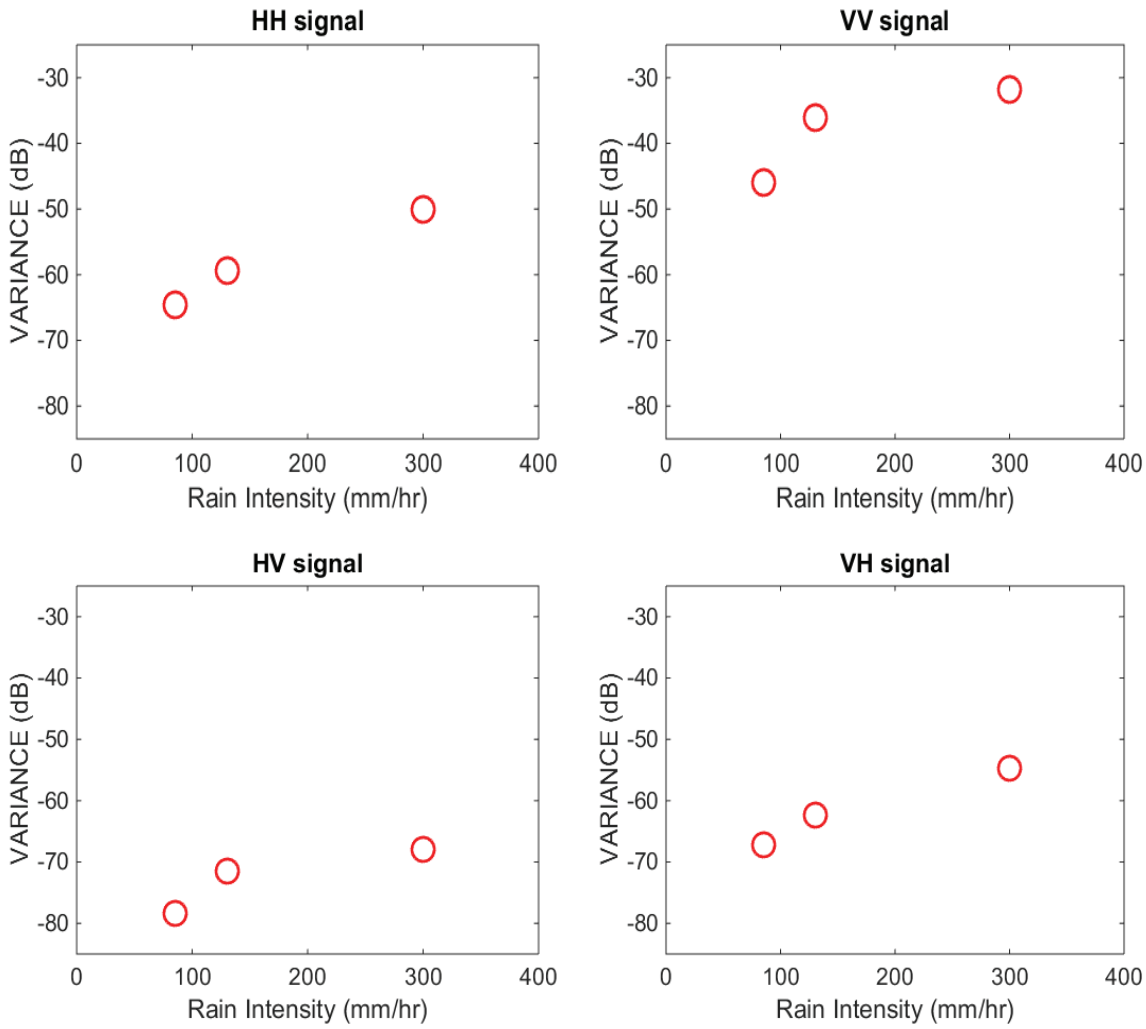

Figure 3.37: Radar backscattering signals of 3 different rain intensities at 57 degree incident angle. Each plotting symbol represents one experimental run. There were 5 repeated runs for each rain intensity.

Chapter 4: Summary, Conclusions and Future Work

4.1 Summary and Conclusions

It is found that for single drop impacts on a quiescent water surface, the plot of average impact-induced stalk height versus Froude showed three different behaviors in the range $300<Fr<2,000$. For $300<Fr<1,000$, the stalk height is proportional to the one fourth power of the Froude number. For $1000<Fr<1800$, the stalk height increases linearly with Froude number. For $1,800<Fr<2,000$, the crown sometimes blocks the formation of the stalk and the average stalk height decreases with increasing Froude number. The standard deviation of the stalk heights in repeated drop impacts on a quiescent surface is quite small, except in the range $1,800<Fr<2,000$.

For raindrop impact-induced stalks, the average stalk heights were less than in the single drop cases at the same drop impact Froude numbers. However, the stalk height variation at any stalk height was much larger than in the single drop case. In addition, occasional bubble entrainment was observed even in the lowest raindrop velocity impact ($Fr = 500$) while this phenomena only occurred for Froude numbers greater than 1,800 in the single drop experiments. Furthermore, the width of the stalk height distribution was correlated with the rain intensities rather than

the drop impact velocity.

The measurement of the subsurface flow field showed that the stalk height was inversely proportional to the local vertical velocity in the target pool near the free surface just before drop impact. The RMS velocities near the free surface increased with increasing raindrop impact velocity. However, the rain intensity did not have a significant effect on the RMS velocity.

The air-seas interface in rain fields and its effects on the attenuation of radar backscattering were experimentally studied in the laboratory. The measurement results show that strong radar return signals are observed from the water surface inside the rain field while the radar return signals from both raindrops and the surface waves in front of the rain field are weak. The experimental results also show that the radar return intensity increases as the rain intensity increases from 85 to 300 mm/hr. In addition, it is found that the attenuation of the radar backscattering from the rain field is likely correlated with a high-water-content layer of secondary droplets generated in the rain field.

4.2 Directions for Future Work

In the present experiments, the variations in the impact Froude and Weber numbers were due primarily to changes in the impact velocity, while the droplet diameter and water properties were held nearly constant. In future work, it is important to test the effect of initial droplet diameter and fluid properties on the results. Surfactants could be added to water to study the effect of different surface

tension as well. It is also helpful to predict the raindrops impact by studying the effect of moving water surface since the water surface in a rain field is fluctuating and moving. Finally, a further investigation of flow conditions after the collapse of a crater for high Froude number (greater than 1800) is needed.

A 3D surface imaging is needed to measure surface slope in order to take out the effect of impingement angle. Thus, the effect of subsurface flow field to stalk height will be better understood. A rain experiment with 85 mm/hr rain intensity is need to investigate the corresponding subsurface flow field.

For Radar measurement, only X-band waves were measured while the other radar waves such as C-band waves are also commonly used for weather radar detection. Thus, it is important to explore the effect of electromagnetic frequency effect as well. Also, the needle spacing can be further reduced to investigate the effect of stalk distance on radar backscattering power.

Bibliography

[1] S. K. Alghoul, C. N. Eastwick, and D. B. Hann, *Normal droplet impact on horizontal moving films: an investigation of impact behaviour and regimes* (Exp. Fluids, 2011), Vol. 50, pp. 1305 - 1316.

[2] R. G. Barry, and R. J. Chorley, *Atmosphere, weather and climate* (Routledge, New York, 2003).

[3] J. Beya, W. Peirson, and M. Banner, *Rainfall-generated, near-surface turbulence* (Gas Transfer at Water Surfaces, Kyoto University Press, 2010), pp. 90.

[4] L.F. Bliven, H. Branger, P. Sobieski, and J-P. Giovanangeli, *An analysis of scatterometer returns from a water surface agitated by artificial rain: evidence that ring-waves are the main feature* (Int. J. Remote Sensing, 1993), Vol. 14, No. 12, pp. 2315 - 2329.

[5] L.F. Bliven, P. W. Sobieski, and C. Craeye, *Rain generated ring-waves: Measurements and modelling for remote sensing* (Int. J. Remote Sensing, 1997), Vol. 18, No. 1, pp. 221 - 228.

[6] N. Braun, M. Gade and P. A. Lange, *The effect of artificial rain on wave spectra and multi-polarization X band radar backscatter* (Int. J. Remote Sens., 2002), Vol. 23, Iss. 20, pp. 4305 - 4323.

[7] Y. K. Cai, *Phenomena of a liquid drop falling to a liquid surface* (Exp. Fluids, 1989), Vol. 7, pp. 388 - 394.

[8] D. R. Caldwell and W. P. Elliott, *Surface stresses produced by rainfall* (Journal of Physical Oceanography, 1971), Vol. 1, pp. 145 - 148.

[9] N. S. Cheng, *Comparison of formulas for drag coefficient and settling velocity of spherical particles* (Powder Technology, 2008).

[10] C. Craeye, P. W. Sobieski, L. F. Bliven, and A. Guissard, *Ring-waves generated by water drops impacting on water surfaces at rest* (IEEE Journal of Oceanic Engineering,1999), Vol. 24, No. 3, pp. 323 - 332.

[11] G. D. Crapper and E. Horwood, *Introduction to water waves* (Wiley, 1984).

[12] R. W. Cresswell and B. R. Morton, *Dropformed vortex rings -The generation of vorticity* (Physics of Fluids, 1995), Vol. 7, pp. 1363.

[13] E.K. Edgerton and J.R. Killiam, *Flash: Seeing the unseen by ultra-high speed photograph* (Hall Publishing Company, 1939).

[14] O.G. Engel, *Crater depth in fluid impacts* (J. Appl. Phys., 1967), Vol. 37, No. 4, pp. 1798 - 1808.

[15] A. I. Fedorchenko and A. Wang, *On some common features of drop impact on liquid surfaces* (Physics of Fluid, 2004), Vol. 16, pp. 1349.

[16] G.J. Franz, *Splashes as sources of sound in liquids* (J. Acoust. Soc. AM., 1959), Vol. 31, No. 8, pp. 1080 - 1096.

[17] T. Green and D. F. Houk, *The mixing of rain with near-surface water* (J. Fluid Mech., 1979), Vol. 90, pp. 569 - 588.

[18] J. P. Hansen, *Rain backscatter tests dispel old theories* (Microwaves & RF, 1986), Vol. 25, pp. 97 - 102.

[19] F. H. Harlow and J. P. Shannon, *The splash of a liquid drop* (Journal of Applied Physics, 1967), Vol. 38, pp. 3855.

[20] E. L. Harrison, F. Veron, D. T. Ho, M. C. Reid, P. Orton, and W. R. McGillis, *Nonlinear interaction between rain- and wind-induced air-water gas exchange* (Journal of Geophysical Research, 2012), Vol. 117, C03034.

[21] D. T. Ho, W. E. Asher, L. F Bliven, P. Schlosser and E. L. Gordan*On mechanisms of rain-induced air-water gas exchange* (Journal of Geophysical Research, 2000), Vol. 105, No. C10, pp. 24,045- 24,057.

[22] P. V. Hobbs and A. J. Kezweeny, *Splashing of a water drop* (Science, 1967), Vol. 155, pp. 1112 - 1114.

[23] D. Houk and T. Green, *A note on surface waves due to rain* (Journal of Geophysical Research, 1976), Vol. 81, No. 24, pp. 4482 - 4484.

[24] M. Hsiao, S. Lichter, and L. G. Quintero, *The critical Weber number for vortex and jet formation for drops impinging on a liquid pool* (Physics of Fluids, 1988), Vol. 31, pp. 3560.

[25] O. W. Jayaratne and B. J. Masion, *The coalescence and bouncing of water drops at an air/water interface* (Proc. R. Soc., (1964), Vol. 280, No. 1383, pp. 545 - 565.

[26] K. B. Katsaros, *Effects of precipitation on the eddy exchange in a wind-driven sea* (Dynamics of Atmospheres and Oceans, 1976), Vol. 1, pp. 99 - 126.

[27] C. Kidd and V. Levizzani, *Status of satellite precipitation retrievals* (Hydrol. Earth Syst. Sci, 2011), Vol. 15, pp. 1109 - 1116.

[28] C. Kummerow, W. Barnes, T. Kozu, J. Shiue, and J. Simpson, *The Tropical Rainfall Measuring Mission (TRMM) Sensor Package* (Journal of Atmospheric and Oceanic Technology, 1997), Vol. 15, pp. 809 - 817.

[29] P. A. Lange, G.V.D. Graaf and M. Gade *Rain-induced subsurface turbulence measured using image processing methods* (Geoscience and Remote Sensing Symposium, 2000 IEEE, 2000), Vol. 7, pp. 3175 - 3177.

[30] J. O. Laws, and D. A Parsons, *The relation of raindrop size to intensity* (Trans. Amer. Geophysical Union, 1943), pp. 452 - 460.

[31] D. Lemaire, L.F. Bliven, C. Craeye, and P. Sobieski, *Drop size effects on rain-generated ring-waves with a view to remote sensing applications* (Int. J. Remote Sensing, 2002), Vol. 23, No. 12, pp. 2345 - 2357.

[32] P. Lenard, *Uber regen* (Meteor. Z., 1904), Vol. 21, pp. 248 - 262.

[33] J. L. Liow, *Splash formation by spherical drops* (J. Fluid Mech., 2001), Vol. 427, pp. 73 - 105.

[34] A.Lipson, S.G.Lipson, and H.Lipson, *Optical Physics* (University Press, Cambridge, UK, 2010), IV edition.

[35] X. Liu and J. H. Duncan, *An experimental study of surfactant effects on spilling breakers* (J. Fluid Mech., 2006), Vol. 567, pp. 433 - 455.

[36] X. Liu, Q. Zheng, R. Liu, D. Wang, J. H. Duncan and S. Huang, *A study of radar backscattering from water surface in response to rainfall* (Journal of Geophysical Research, 2016), Vol. 121, pp. 1546 - 1562.

[37] X. Liu, Q. Zheng, R. Liu, M. A. Sletten, and J. H. Duncan, *A Model of Radar Backscattering of Rain-Generated Stalks on the Ocean Surface* (IEEE Trans. on Geoscience and Remote Sensing, 2017), Vol. 55, No. 2, pp. 767 - 776.

[38] S. L. Manzello and J.C. Yang, *An experimental study of a water droplet impinging on a liquid surface* (Exp. Fluids, 2002), Vol. 32, pp. 580 - 589.

[39] R. Marks, *Preliminary investigations on the influence of rain on the production,concentration, and vertical distribution of sea salt aerosol* (J. Geophys. Res., 1990), Vol. 95, No. C12, pp. 22,299 - 22, 304.

[40] B. L. Mehaute, *Gravity-capillary rings generated by water drops* (J. Fluid Mech., 1988), Vol. 197, pp. 415 - 427.

[41] A. K. Mishra, *A new technique to estimate precipitation at fine scale using multifrequency satellite observations over Indian land oceanic regions* (IEEE Trans. on Geoscience and Remote Sensing, 2013), Vol. 51, No. 7, pp. 4349 - 4358.

[42] R. Moore, Y. Yu, A. Fung, D. Kaneko, G. Dome, and R. Werp, *Preliminary study of rain effects on radar scattering from water surfaces* (IEEE J. Oceanic Eng., 1979), Vol. 4, No. 1, pp. 31 - 32.

[43] J. A. Nystuen,*Rainfall measurements using underwater ambient noise* (J. Acoust. Soc. AM., 1986), Vol. 79, No. 4, pp. 972 - 982.

[44] T. Oguchi, *Electromagnetic wave propagation and scattering in rain and other hydrometeors* (Proceeding of IEEE,1983), Vol. 71, No. 9, pp. 1029 - 1078.

[45] B. Peck and L. Sigurdson, *The threedimensional vortex structure of an impacting water drop* (Physics of Fluid, 1994), Vol. 6, No. 2, pp. 564 - 576.

[46] B. Peck and L. Sigurdson, *The vortex ring velocity resulting from an impacting water drop* (Exp. in Fluids, 1995), Vol. 18, pp. 351 - 357.

[47] W. L. Peirson, J. F. Beya, M. L. Banner, J. S. Peral and S. A. Azarmsa, *Rain-induced attenuation of deep-water waves* (J. Fluid Mech., 2013), Vol. 724, pp. 5 - 35.

[48] H. C. Pumphrey and P. A. Elmore, *The entrainment of bubbles by drop impacts* (J. Fluid Mech., 1990), Vol. 220, pp. 539 - 567.

[49] Y. Poon, S. Tang, and J. Wu, *Interactions between Rain and Wind Waves* (Journal of Physical Oceanography, 1992), Vol. 22, pp. 976 - 987.

[50] A. Prosperetti and H. N. Oguz, *The impact of drops on liquid surfaces and the underwater noise of rain* (Annu. Rev. Fluid Mech., 1993), Vol. 25, pp. 577 - 602.

[51] C.J.C. Reason, *On the effect of ENSO precipitation anomalies in a global ocean GCM* (Climate Dynamics, 1992), Vol. 8, pp. 39 - 47.

[52] M. Rein, *Phenomena of liquid drop impact on solid and liquid surfaces* (Fluids Dyn. Res., 1993), Vol. 12, pp. 61 - 93.

[53] M. Rein, *The transitional regime between coalescing and splashing drops* (J. Fluid Mech., 1996), Vol. 306, pp. 145-165.

[54] O. Reynolds, *On the floating of drops on the surface of water depending only on the purity of the surface* (Proc. Manchester Lit. Phil. Soc., 1881), Vol. 21, pp. 1 - 2.

[55] F. Rodriguez and R. Mesler, *A Model of Evaporating Spray Droplet Dispersion* (J. Colloid Interface Sci., 1988), Vol. 96, No. C4, pp. 7181 - 7200.

[56] M. Santini, S. Fest-Santini, G. E. Cossali, *LDV characterization and visualization of the liquid velocity field underneath an impacting drop in isothermal conditions* (Exp. Fluids, 2013), Vol. 54, pp. 1593.

[57] P.Schlussel, A. V. Soloviev and W. J. Emery, *Cool and freshwater skin of the ocean during rainfall* (Boundary-Layer Meteology, 1997), Vol. 82, pp. 437 - 472.

[58] R. M. Schotland, *Experimental results relating to the coalescence of water drops with water surfaces* (Disc. Faraday Soc., 1960), Vol. 30, pp. 72 - 77.

[59] G. L. Siscoe and Z. Levin, *Water-Drop-Surface-Wave Interactions* (Journal of Geophysical Research, 1971). Vol. 76, No. 21, pp. 5112 - 5116.

[60] M. A. Sletten and D. B. Trizna,*An unltrawideband, polarimetric radar for the study of sea scatter* (IEEE Trans. on Antennas and Propagation, 1994), Vol. 42. No. 11, pp. 1461 - 1466.

[61] P. W. Sobieski, C. Craeye and L. F. Bliven, *Scatterometric signatures of multivariate drop impacts on fresh and salt water surfaces* (Int. J. Remote Sensing, 1999), Vol. 20, pp. 2149 - 2166.

[62] A.F. Spilhaus, *Raindrop size, shape, and falling speed* (J. Meteor, 1948), Vol. 5, pp. 161 - 164.

[63] C. D. Stow and R. D. Stainer, *The physical products of a splashing water drop* (Journal of the Meteorological Society of Japan, 1977), Vol. 55, pp. 518 - 532.

[64] Ulaby, F. T., R. K. Moore, and A. K. Fung, *Microwave Remote Sensing: Active and Passive, Volume II: Radar remote sensing and surface scattering and emission theory* (Addison-Wesley Publishing Co., Reading, MA, 1982), pp. 624.

[65] N. J. Washuta, *Air Entrainment in the Turbulent Ship Hull Boundary Layer* (Doctoral Dissertation, 2016), Retrieved from Digital Repository at the University of Maryland.

[66] L. B. Wetzel, *On the theory of electromagnetic scattering from a raindrop splash* (Radio Science, 1990), Vol. 25, pp. 1183 - 1197.

[67] A.M. Worthington, *A Study of Splashes* (Longmans, Green, and Co, 1908).

[68] C. J. Zappa, D. T. Ho, W. R. McGillis, M.L. Banner, J. W. H. Dacey, L. F. Bliven, B. Ma, J. Nystuen, *Rain-induced turbulence and air-sea gas transfer* (Journal of Geophysical Research, 2009), Vol. 114.

[69] H. Zhao, A. Brunsvold, S. T. *Munkejord Investigation of droplets impinging on a deep pool: transition from coalescence to jetting* (Exp. Fluids, 2011), Vol. 50, pp. 621 - 635.

[70] G. Z. Zhu, Z. H. Li and D. Y. Fu, *Experiments on ring wave packet generated by water drop* (Chinese Science Bulletin, Beijing, 2008), Vol. 53, pp. 1634 - 1638.